# ELLIPSOMETRY OF $Ni_{1-x}Pt_x$ ALLOYS AND RELATED SILICIDES

BY

LINA ABDALLAH

A thesis submitted to the Graduate School
in partial fulfillment of the requirements
for the degree of
Doctor of Philosophy

Major Subject: PHYSICS

New Mexico State University
Las Cruces, New Mexico
August 2014

"Ellipsometry of $Ni_{1-x}Pt_x$ Alloys and Related Silicides," a thesis prepared by Lina Abdallah in partial fulfillment of the requirements for the degree, Doctor of Philosophy of Science, has been approved and accepted by the following:

---

Loui Reyes
Dean *ad interim* of the Graduate School

---

Stefan Zollner
Chair of the Examining Committee

---

Date

Committee in charge:

Dr. Stefan Zollner, Chair

Dr. Igor Vasiliev

Dr. Michael Engelhardt

Dr. David Voelz

# DEDICATION

I dedicate this work to my beloved parents for their endless support throughout this process.

ACKNOWLEDGMENTS

My deepest gratitude goes to Dr Stefan Zollner for his guidance and encouragement throughout this work. Special thanks go to the examining comittee: Dr Igor Vasiliev, Dr Michael Engelhardt and Dr David Voelz for their valuable input on this work. I also would like to thank my research group: Travis Willett-Gies, Nalin Fernando, Eric DeLong, Cayla Nelson, Nathan Nunley, Khadijih Mitchell, Cesar Rodriguez and Laura Piñeda for their support. Many thanks to Loretta Gonzales, our department secretary, and Rosa Christensen, our fiscal assistant, for their dedicated work. I am grateful to our collaborators at IBM and Globalfoundries Ahmet Ozcan, Christian Lavoie and Mark Raymond. Many thanks also to Dr Igor Vasiliev and Tarek Tawalbeh for contributing the theoretical part of our work. My sincere thanks go to Harland Tompkins, Tom Tiwald, James Hilfiker, Gerry Cooney and Craig Herzinger from the Woollam company for all the advice and the support they provided on the data analysis and modeling.

We are grateful to V.W. Kamineni and A.C. Diebold for offline discussions and helpful suggestions. We also thank Peter de Chatel for a careful reading of our manuscript and useful comments.

This work was performed, in part, at Arizona State University and also at the Center for Integrated Nanotechnologies, an Office of Science User Facility operated for the U.S. Department of Energy (DOE) Office of Science by Los Alamos National Laboratory (Contract DE-AC52-06NA25396) and Sandia National Laboratories (Contract DE-AC04-94AL85000). We are grateful to Dr. R.J. Davis and his colleagues at The Ohio State University, Columbus, OH, for providing sputtered Ni films on $SiO_2$ with varying thicknesses.

This work was supported by the National Science Foundation (DMR-1104934).

This work has been partially supported by the independent Bulk CMOS and SOI technology development projects at the IBM Microelectronics Division Semiconductor Research & Development Center, Hopewell Junction, NY 12533.

# VITA

| | |
|---|---|
| 2002-2006 | B.S. in Physics,<br>University of Jordan, Amman, Jordan |
| 2006-2009 | MS in Physics,<br>University of Jordan, Amman, Jordan |
| 2012 | MS in Physics,<br>New Mexico State University |
| 2014 | PhD in Physics<br>New Mexico State University |

# ABSTRACT

ELLIPSOMETRY OF $Ni_{1-x}Pt_x$ ALLOYS AND RELATED SILICIDES

BY

LINA ABDALLAH

Doctor of Philosophy

New Mexico State University

Las Cruces, New Mexico, 2014

Dr. Stefan Zollner, Chair

In this work we present the composition dependence of the optical constants of $Ni_{1-x}Pt_x$ ($0<x<0.25$) alloys and $Ni_{1-x}Pt_xSi$ ($0<x<0.30$) monosilicides. $Ni_{1-x}Pt_x$ alloys were deposited on top of $SiO_2$ on top of a two-side polished silicon substrate. The same set of metal alloys was also deposited on silicon and heated at 500°C for 30 s to create monosilicides.

Near-infrared to visible to near-ultraviolet measurements were performed using spectroscopic ellipsometry over a photon energy from 0.6 eV to 6.6 eV. For unreacted $Ni_{1-x}Pt_x$ alloys angles of incidence were varied from 20° to 80° to improve the accuracy of the measurement. For $Ni_{1-x}Pt_xSi$, the angles of incidence were varied from 65° to 75° since using a broader range does not change the results.

Results on metal alloys obtained in the near-ultraviolet range show an absorption peak at 4.5 eV that broadens with increasing platinum content. Ab initio density functional calculations by our collaborators are used to explain this

result. Previous density of states calculations performed on nickel silicides are analyzed to understand our experimental results for $Ni_{1-x}Pt_xSi$ monosilicides. For $Ni_{1-x}Pt_xSi$ monosilicides, our ellipsometry results show two absorption peaks at around 1.5 eV and 4.5 eV.

Infrared ellipsometry is performed on the same samples and results show a pure metallic behavior for unreacted $Ni_{1-x}Pt_x$ alloys.

Ellipsometric data are fitted using a set of oscillators to describe optical transitions. A Drude oscillator is used to describe free carrier absorption as well as intraband transitions whereas a Lorentz oscillator is used to describe interband transitions.

# CONTENTS

# LIST OF TABLES

# LIST OF FIGURES

# 1 Introduction

## 1.1 Light Interaction With Materials

The optical constants of materials depend on how light interacts with matter. Light-matter interaction occurs in different ways. When a light beam travels through air and hits the sample, part of it will get reflected and the rest will pass through the sample. The portion of the light that is not reflected can be refracted, absorbed or scattered. Refraction causes the velocity of the light to change as it enters a new medium; this velocity change results in bending of the light beam. Absorption occurs when the energy of the photon matches a transition energy of atoms in the crystal. Absorption is related to transmission since the portion of the light that does not get absorbed will be transmitted through the medium. The effect of scattering is negligible for smooth samples compared to the other phenomena that might occur when light interacts with the medium. Scattering results in the change of the light's direction and possibly frequency (depending on whether the scattering is elastic or inelastic).

The optical response of a material is given by the **complex index of refraction**

$$\tilde{N} = n + ik, \tag{1}$$

where $n$ is called the **index of refraction**; $k$ is called the **extinction coefficient** and is related to absorption. $n$ is related to the velocity of the light $v$ in the material relative to the speed of light in free space $c$:

$$n = \frac{c}{v}. \tag{2}$$

$k$ is related to the change of the intensity of the light wave as it propagates through the material. The intensity of light inside the material $I(z)$ at depth $z$ is related to the incident intensity $I_0$:

$$\frac{dI(z)}{dz} = -\alpha I(z). \tag{3}$$

This equation has a solution of the form

$$I(z) = I_0 e^{-\alpha z}, \tag{4}$$

where $I_0$ is the intensity of the light just inside the sample and $\alpha$ is called **the absorption coefficient** and it describes the loss of the light intensity due to absorption only. The extinction coefficient is related to absorption coefficient through the equation

$$k = \frac{\lambda}{4\pi}\alpha. \tag{5}$$

The penetration depth is defined as

$$D = \frac{1}{\alpha}. \tag{6}$$

### 1.2 Polarization of Light

Polarization is an important concept when it comes to understanding how ellipsometry works. Maxwell's equations show that light is a transverse wave where the electric and the magnetic field components are perpendicular to each other. When studying optical phenomena only the electric field is considered [1].

The electric field vector has two components that are perpendicular to each other and both are perpendicular to the direction of light wave propagation. When there is a random relationship between the electric field components, such as the light coming from the sun or from a light bulb, light is said to be unpolarized. If the electric field vector is confined to an axis in the plane perpendicular to the

direction of propagation, light is said to be linearly polarized. The direction of polarization is given by the direction of the electric field. When two orthogonal light waves propagate through space in phase, the resulting light wave will be linearly polarized. If the electric field vector precesses around the axis of propagation, light is said to be circularly or elliptically polarized. The type of polarization depends on the phase shift between the light waves and the amplitude of each wave.

For a light wave travelling along the z direction, polarization is described by taking the superposition of the two electric field components along x and y directions using the equation

$$\begin{aligned} \mathbf{E}(z,t) &= \mathbf{E}_x(z,t) + \mathbf{E}_y(z,t) = \\ & E_{x0}\exp[i(\omega t - Kz + \delta_x)]\hat{\mathbf{x}} + E_{y0}\exp[i(\omega t - Kz + \delta_y)]\hat{\mathbf{y}}, \end{aligned} \tag{7}$$

where $\delta$ is the initial phase of the light. For spectroscopic ellipsometry applications, we are interested in the phase difference $\delta_x$ - $\delta_y$ rather than the initial phases of the electric field components. Figure 1 shows the various phase shift differences of light and how they result in various polarization states.

Linear polarization states can be labeled as p and s depending on the direction of the electric field components with respect to the plane of incidence. The plane of incidence refers to the virtual plane that contains the incident beam, the reflected beam, and the normal to the surface of the sample. In p-polarization, the electric field of the beam is parallel to the plane of incidence. Whereas in s-polarization, the electric field of the beam is perpendicular to the plane of incidence.

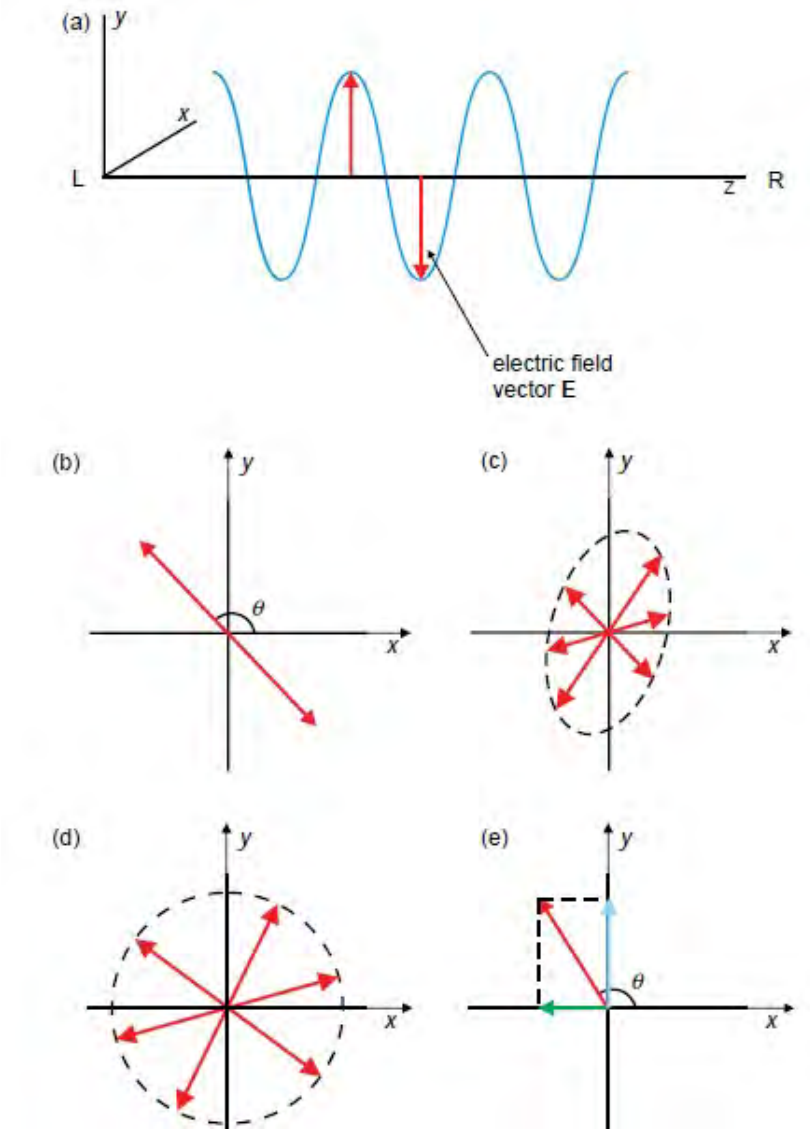


Figure 1: a) A light wave propagating from left to right along the $z$-axis. b) The electric field vector oscillates along an axis at a constant angle $\theta$ forming linearly polarized light. c) The electric field vector traces out an ellipse around the direction of propagation forming elliptically polarized light. d) The electric field vector traces out a circle forming circularly polarized light. e) The electric field vector can be resolved at any time into two perpendicular components, as shown by Eq. (7). From Ref. [1]

## 1.3 Ellipsometry

Ellipsometry is a precise optical technique that has been used to study the optical properties of bulk materials and thin films for over 100 years. The uniqueness of this tool comes from the fact that it compares the polarization state of the light beam before and after it hits the sample surface rather than measuring the absolute value of the reflected beam intensity [2].

Upon reflection, the light beam suffers from a phase shift in the s and p components of the electric field as well as an amplitude reduction of each light wave. Both changes are described by the two ellipsometric angles $\Psi$ and $\Delta$, where $\Psi$ describes the relative amplitude reduction and $\Delta = \delta_1 - \delta_2$ describes the phase shift. $\delta_1$ is the phase difference between the p-wave and s-wave before reflection and $\delta_2$ is the phase difference between the p-wave and s-wave after reflection. $\Psi$ and $\Delta$ are related to the Fresnel reflection coefficients $r_p$ and $r_s$ through

$$\frac{r_p}{r_s} = \rho = \tan\Psi \times e^{i\Delta}. \tag{8}$$

A vast amount of information can be obtained by ellipsometry. Some of the properties that can be determined by ellipsometry are optical constants (n and k or $\epsilon_1$ and $\epsilon_2$ ), film thickness, surface conditions, doping concentration, optical anisotropy, etc. The optical constants of a material cannot be determined from ellipsometry measurements directly. Rather it measures $\Psi$ and $\Delta$ which can then be converted to optical constants in an inverse problem where a model for the sample needs to be built and compared with the experimental data.

Once the ellipsometric angles are determined the pseudodielectric function can be calculated via the equation [3]

$$\epsilon \approx \langle\epsilon\rangle = \left(\frac{1-\rho^2}{1+\rho}\right)\tan\phi^2\sin\phi^2 + \sin\phi^2, \tag{9}$$

where $\phi$ is the angle of incidence and $\rho$ is the complex Fresnel reflectance ratio. This approximation only works for bulk isotropic substrates.

Even though ellipsometry is a powerful tool when it comes to characterizing bulk materials and thin films, there are some conditions on the sample that have to be met so ellipsometry can be effective. The first requirement is that the wavelength of the light beam needs to be similar (within a few orders of magnitude) to the film thickness. Second, the roughness of the film has to be no more than 10% of the penetration depth. The third requirement is that the variation of the film thickness across the sample should be less than 10%. Finally, the sample must be larger than our beam (typically 5 to 10 mm diameter) and uniform across the area probed by the beam. Some ellipsometers, such as the one used to perform this work, can account for these flaws if they exist in the sample.

### 1.4 Procedure

The general procedure of ellipsometry starts with measuring the ellipsometric angles as a function of wavelength at different angles of incidence. Both varying the angles of incidence and measuring over a broad range of wavelengths enhance the information about the sample and increase the accuracy of the measurement. After the measurement is performed, a model that has some unknown parameters is built. The model should have the same number of layers as the sample measured. The values of the other parameters in the model are guessed depending on the properties of the sample shown in the experimental graph. A fit is performed that causes parameters to change until the experimental data match the calculated data from the model. After the best fit is obtained, the final model parameters will represent the true optical properties of the sample.

The experimental procedure starts with unpolarized light radiating from a

Xenon lamp (190 nm to 2 $\mu$m). Even though the light source covers the whole spectrum that extends from quartz-UV to the near-infrared, the choice of the optical fiber used to pass the light between the optical elements may limit the wavelength range on which the measurement is performed. Two types of optical fibers can be used and each one of them affects the wavelength range differently. The UV fiber transmits light in the quartz-UV and absorbs light at 1340-1450 nm. The IR fiber absorbs above 300 nm. These absorption bands need to be taken into account when performing ellipsometric measurements. A monochromator is placed after the light source to ensure that monochromatic light is incident on the sample. After the light beam leaves the monochromator and travels through the optical fiber, it reaches an input unit that contains a focusing lens and a polarizer. This allows the polarization state of the light wave to change to linear. As the light hits the sample, the polarization state changes from linear to elliptical. In order to compare the change in s and p states of the light beam upon reflection, light polarization state has to be converted to linear again. An analyzer is used to convert the polarization state back to linear. The detector used in our system is either a silicon or InGaAs photodiode detector. The detector measures the intensity of the light and the s and p components of the electric field that are related to the ellipsometric angles via the equation [4, 5]

$$\rho = (E_{rp}/E_{ip}) \,/\, (E_{rs}/E_{is}) = (\tan\psi)\, e^{i\Delta}. \tag{10}$$

Figure 2 shows a schematic description of the optical components of ellipsometry.

### 1.5 Ellipsometry Applications

This section lists some of the applications of ellipsometry that show how much information ellipsometry can provide about the sample under study:

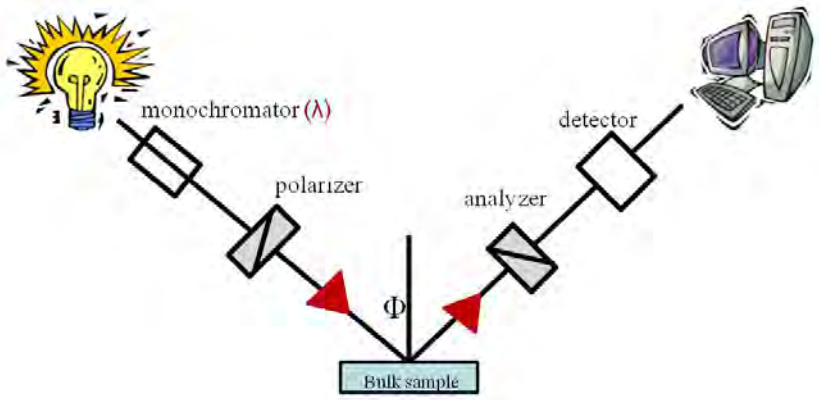


Figure 2: Optical components of ellipsometry: The measurement technique starts with unpolarized light that is radiated by the light source and ends with the signal (ellipsometric angles) shown on the screen.

- Film Thickness:

  Figure 3 shows the responses for different nickel film thicknesses on $SiO_2$. The figure shows interference fringes for both 100 Å and 200 Å thickness, but not for thicker films. The spacing between the interference fringes is related to the optical thickness of the film, while the amplitude of the fringes is related to the optical contrast at each interface (related to the refractive index above and below the interface).

- Surface Conditions:

  Ellipsometry is very sensitive to film surface conditions such as surface roughness, oxides, water layers, etc. Some of the surface conditions that appear in ellipsometric data are listed below. Figure 4 shows the pseudodielectric function for a bulk $LaAlO_3$ sample. Ellipsometric measurements show that there is a surface roughness layer on top of the substrate. The sample was then annealed and the measurement was repeated. The ellipsometric data shows that the pseudo-absorption went down and the apparent surface roughness decreased. Figure 5 shows another surface condition which

appears in our ellipsometric results and that is the contamination of water on top of $Ni_{1-x}Pt_x$ alloy films. Fitting the ellipsometric data for these films results in a 53 Å thick layer of water on the surface. To reduce the water layer, annealing was performed and measurement was taken again and ellipsometric data showed that the water layer thickness was reduced to 7 Å.

- Alloying Effects:

  Optical properties of $Ni_{1-x}Pt_x$ alloys depend on the Pt content in the alloy. Figure 6 shows an absorption peak at 4.5 eV that broadens with increasing Pt content in the alloy.

- Temperature Dependence:

  Figure 7 shows the effect temperature has on the critical points ($E_1$, $E_1+\Delta_1$, $E_2$) of germanium. The graph shows a redshift of the energy and increased broadening of the critical points as the temperature is increased.

### 1.6 Optical Transitions

The model used to compare the experimental data to the generated data in spectroscopic ellipsometry depends on the type of the material and how light propagates through it. There have been many studies on optical properties of materials and therefore some of the optical constants are already tabulated in the software used to analyze ellipsometric data. However, for new types of materials or materials that have never been studied before, such as the samples used in this work, analysis becomes much harder. Knowing what type of optical transitions occur in the material helps to understand the ellipsometric data.

The response of the material to the incident light depends on the energy of the light beam. In the visible or UV range, the photon energy is high enough

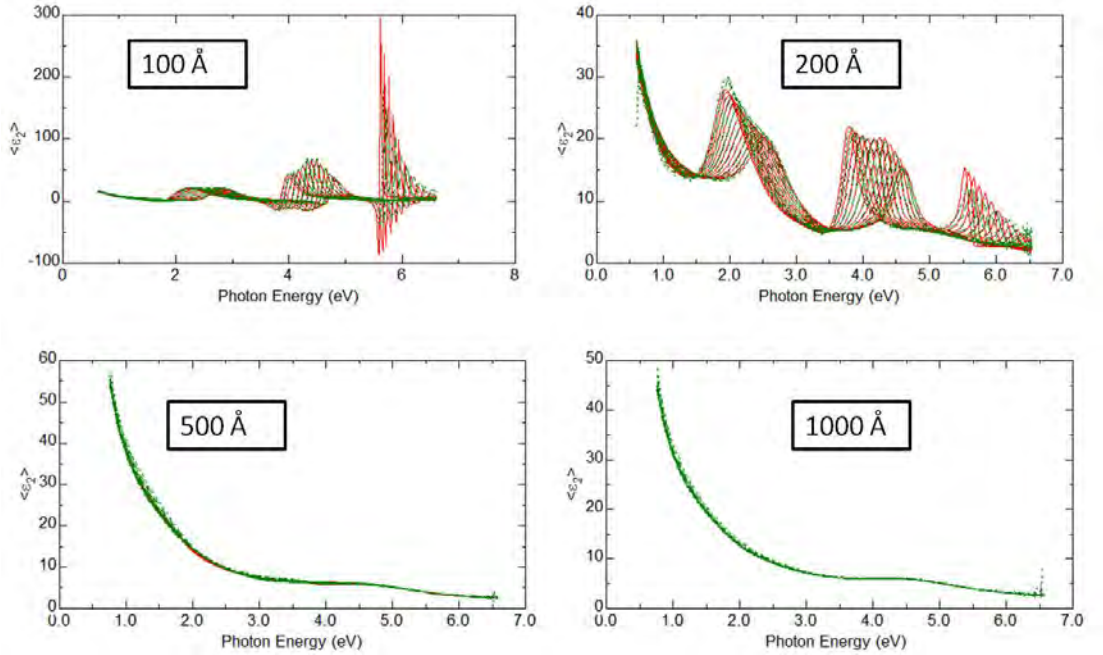


Figure 3: The imaginary part of the pseudodielectric function of different nickel films that were deposited on top of a thick layer of silicon dioxide using silicon as a substrate. The graph shows interference fringes for both 100 Å and 200 Å film thickness that disappear in thicker samples. This response indicates that 100 Å and 200 Å Ni films are still transparent whereas the film is no longer transparent at 500 Å film thickness.

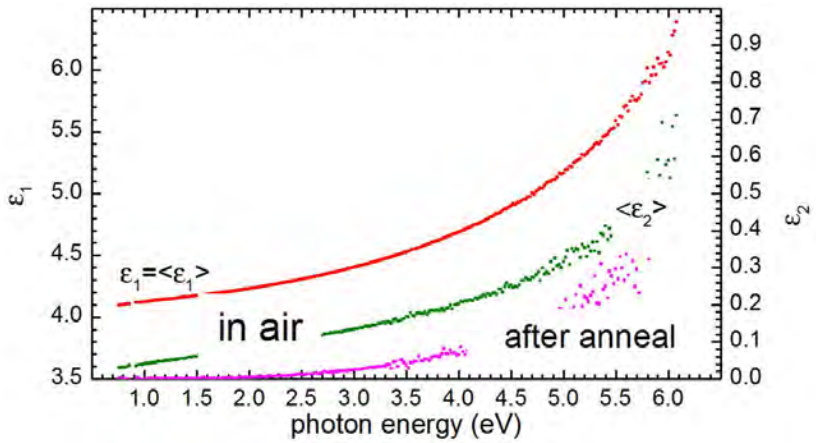


Figure 4: Pseudodielectric function for a bulk $LaAlO_3$ sample. The graph shows $\epsilon_2$ before and after annealing. After annealing, the apparent surface roughness dropped from 15 Å to less than 1 Å [6].

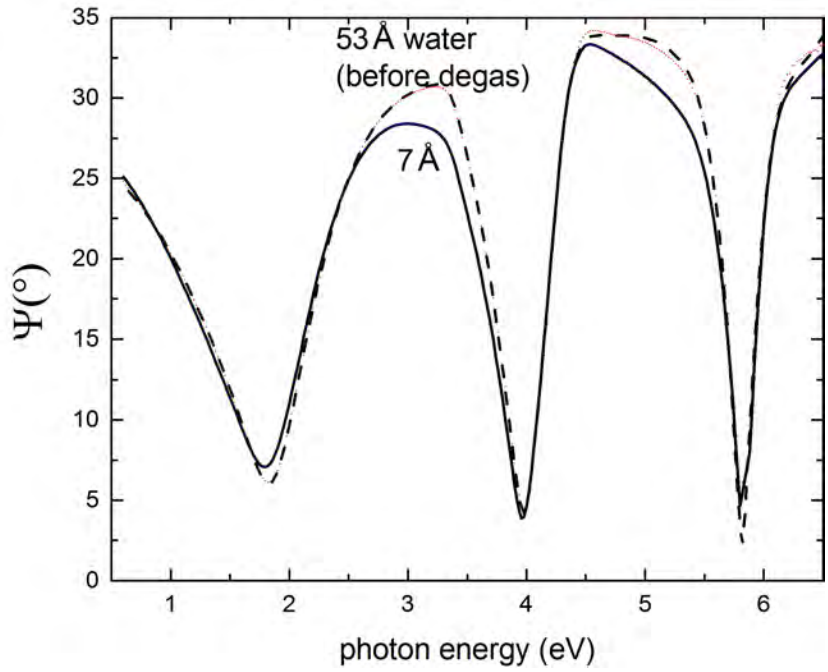


Figure 5: Ellipsometric angle $\Psi$ for 100 Å $Ni_{0.90}Pt_{0.10}$ film. Fitting ellipsometric data resulted in a 53 Å layer of water on the $Ni_{0.90}Pt_{0.10}$ surface. The sample was then annealed at 700 K and the measurement was repeated at room temperature. Annealing reduced the thickness of the water layer to 7 Å [7].

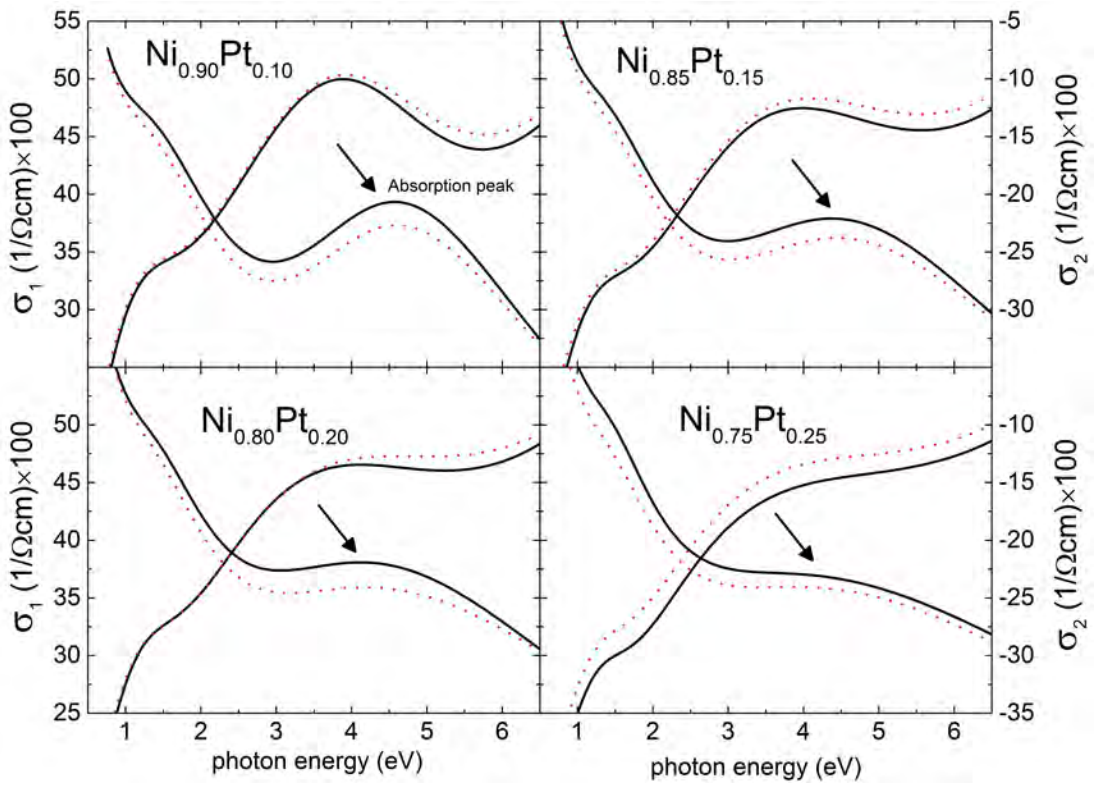


Figure 6: Alloying effect for $Ni_{1-x}Pt_x$ alloys with different Pt concentrations from 10% to 25%. Ellipsometric results show a peak at 4.5 eV due to interband transitions. The absorption peak broadens with increasing Pt content [7].

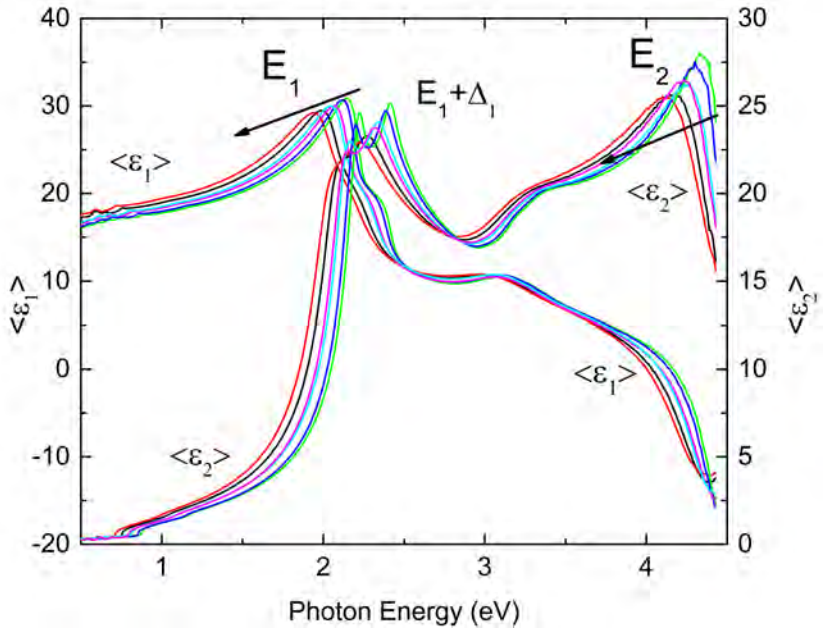


Figure 7: Pseudodielectric function of bulk germanium for increasing temperatures from 77 K to 700 K. The critical points ($E_1$, $E_1 + \Delta_1$, $E_2$) redshift and broaden with increasing temperature.

to excite an electron from one energy state to another. This process results in light absorption. However, in the infrared region, the photon energy is too small to excite electrons and make them hop to other states. Instead, infrared light interacts with lattice vibrations in ionic crystals which are called phonons [8].

In an optical medium, we can assume that there are different types of electron oscillations that occur at different frequencies as a response to the applied electric field.

- **Lorentz Oscillator**

  The Lorentz oscillator is a classical model that describes the response of bound electrons to an oscillating electric field. It assumes that the electron cloud is oscillating back and forth around the nucleus depending on the direction of the electric field. This motion is similar to a harmonic oscillator

where objects oscillate around a fixed position. Applying Newtons Second Law by studying the forces acting on the bound electrons we get [9, 10]

$$-eE_0 \exp(-i\omega t) = m\ddot{x} + b\dot{x} + kx, \tag{11}$$

where $m$ is the **mass** of the electrons (in vacuum), $b$ is the **damping constant**, and $k$ is the strength of the restoring force which is related to the resonance frequency $\omega_0$ by the equation

$$\omega_0 = \sqrt{\frac{k}{m}} \quad \text{or} \quad k = m\omega_0^2. \tag{12}$$

$-eE_0 \exp(-i\omega t)$ is the driving force caused by the applied electric field. By dividing by the mass and using the substitution $b = m\gamma$, the oscillation equation becomes

$$-\frac{eE_0}{m} \exp(-i\omega t) = \ddot{x} + \gamma\dot{x} + \omega_0^2 x. \tag{13}$$

This equation is a second order differential equation whose solution is of the form $x(t) = x_0 \exp(-i\omega t)$. By taking the first and second derivatives and solving for $x_0$ we get

$$\mathrm{x}_0 = \frac{eE_0}{m(\omega^2 - \omega_0^2 + i\omega\gamma)}, \tag{14}$$

where $\gamma = 1/\tau$ is called the **relaxation rate** and $\tau$ is the **scattering time**. The dielectric polarization is given by

$$P(t) = -nex(t) = -\frac{ne^2 E_0}{m(\omega^2 - \omega_0^2 + i\gamma\omega)} \exp(-i\omega t) = \epsilon_0 \chi(\omega) E(t), \tag{15}$$

where $-ex$ is the dipole moment of one electron and $n$ is the **charge density**

per unit volume. The dielectric susceptibility $\chi(\omega)$ therefore becomes

$$\chi(\omega) = \frac{-e^2 n}{\epsilon_0 (m\omega^2 + ib\omega - k)}. \quad (16)$$

The dielectric function $\epsilon(\omega)$ equals

$$\epsilon(\omega) = 1 + \chi(\omega) = 1 - \frac{e^2 n}{\epsilon_0 m (\omega^2 + ib\omega/m - k/m)}. \quad (17)$$

We define the **plasma frequency** as

$$\omega_P^2 = \frac{ne^2}{m\epsilon_0}. \quad (18)$$

The dielectric function then becomes simplified:

$$\epsilon(\omega) = 1 - \frac{m\omega_P^2}{m\omega^2 + ib\omega - k} = 1 + \frac{\omega_P^2}{\omega_0^2 - \omega^2 - i\gamma\omega}. \quad (19)$$

Separating the real part from the imaginary part in Eq. (19) we get

$$\epsilon(\omega) = 1 - \frac{\omega_P^2 (\omega^2 - \omega_0^2)}{(\omega^2 - \omega_0^2)^2 + \gamma^2\omega^2} + i\frac{\omega_P^2 \gamma\omega}{(\omega^2 - \omega_0^2)^2 + \gamma^2\omega^2} = \epsilon_1 + i\epsilon_2. \quad (20)$$

A **pole** is a Lorentz oscillator with zero broadening (damping). The dielectric function of a pole is real and has the form

$$\epsilon(\omega) = 1 + \frac{\omega_P^2}{\omega_0^2 - \omega^2}. \quad (21)$$

- **Drude Oscillator**

  The Drude model is used for free electrons in metals as well as in semiconductors. When a light beam hits a metal, it interacts with free electrons present near the surface of the metal. The interaction between light and free electrons causes these free electrons to oscillate and scatter when colliding with defects and other electrons.

The Drude model is a modification of the Lorentz model. The restoring force vanishes for free electrons, we have $k$=0 and $\omega_0$=0. Therefore,

$$\epsilon(\omega) = 1 - \frac{\omega_P^2}{\omega^2 + i\gamma\omega} \tag{22}$$

The **DC conductivity** is defined as

$$\sigma_0 = \frac{ne^2}{\gamma m} = \frac{ne^2\tau}{m}. \tag{23}$$

The expression of the Drude dielectric function needs to be separated into real and imaginary parts, see [10]:

$$\epsilon_1(\omega) = 1 - \frac{ne^2}{m\epsilon_0(\omega^2+\gamma^2)} = 1 - \frac{\omega_P^2}{\omega^2+\gamma^2} \quad \text{and} \tag{24}$$

$$\epsilon_2(\omega) = \frac{ne^2\gamma}{m\epsilon_0\omega(\omega^2+\gamma^2)} = \frac{\omega_P^2}{\omega^2+\gamma^2} \times \frac{\gamma}{\omega}. \tag{25}$$

The speed of electrons is called $\langle v \rangle$. The time between collisions is called the mean scattering time $\langle \tau \rangle$ and is related to the relaxation energy $\Gamma$ by the relation $\Gamma = \hbar \langle \tau \rangle^{-1}$. Drifting of electrons is caused by the electrostatic force $\mathrm{F}_e$.

For frequencies much smaller than the **relaxation rate** $\gamma$, i.e., , $\omega \ll \gamma$, the real part part of $\epsilon$ becomes a large negative number determined by the square of the ratio of the plasma frequency to the relaxation rate, whereas the imaginary part diverges:

$$\epsilon_1(\omega) \approx 1 - \frac{\omega_P^2}{\gamma^2} \approx -\frac{\omega_P^2}{\gamma^2}, \tag{26}$$

$$\epsilon_2(\omega) \approx \frac{\omega_P^2}{\gamma\omega} \approx -\epsilon_1\frac{\gamma}{\omega} \gg |\epsilon_1|. \tag{27}$$

The complex refractive index at low frequencies is

$$n_1 \approx \sqrt{\epsilon_2/2} = \sqrt{\frac{\omega_P^2}{2\gamma\omega}} \tag{28}$$

$$n_2 \approx \sqrt{\epsilon_2/2} = n_1. \tag{29}$$

The absorption coefficient is

$$\alpha = \frac{2\omega n_2}{c} = \sqrt{\frac{2\omega\omega_P^2}{c^2\gamma}} = \sqrt{\frac{2\mu_0\omega n e^2}{\gamma m}} = \sqrt{2\mu_0\omega\sigma_0}, \tag{30}$$

where he have used $\epsilon_0\mu_0 = 1/c^2$ and the definitions of the plasma frequency $\omega_P$ and the DC conductivity $\sigma_0$. The penetration depth in the DC limit is $\lambda_P = 1/\alpha = 1/\sqrt{2\mu_0\omega\sigma_0}$ and the skin depth is $\delta_0 = 2\lambda_P = \sqrt{2/\mu_0\omega\sigma_0}$, see Ref [11].

The conductivity (see below) in the DC limit is

$$\begin{aligned} \sigma_1 &= \epsilon_0\epsilon_2\omega \approx \epsilon_0\frac{\omega_P^2}{\gamma} = \frac{ne^2}{\gamma m} = \sigma_0, \\ \sigma_2 &= -\epsilon_0\left(\epsilon_1 - 1\right)\omega \approx \frac{\epsilon_0\omega_P^2\omega}{\gamma^2} \approx 0. \end{aligned} \tag{31}$$

### 1.7 Pseudodielectric Function

The pseudodielectric function is the dielectric function obtained directly from the ellipsometric measurement using Eq. (9). The pseudodielectric function is taken as if the sample was one infinitely thick material. If a sample has more than one layer, the pseudodielectric function will not represent the real response of any of the individual films but the response of the whole film stack [5].

## 1.8 Depolarization

Depolarization is the phenomenon where the reflected light is partially polarized which affects the accuracy of the measurement. Depolarization can be caused by weak collimation of the incident light, finite bandwidth of the light, thickness in-homogeneity and backside reflection [5]. Some of these effects can be minimized while performing the measurement.

## 1.9 Data Analysis

To achieve the maximum significance of our measurements, we performed several fitting techniques and compared the results of these techniques in order to get the most accurate set of optical constants. Figure 8 shows the optical conductivity for different $Ni_{1-x}Pt_x$ alloys using different fitting techniques. The graph shows that the overall shape of all the curves is the same.

- **Oscillator Fit**

  In this fit, the choice of the oscillators used depends on the material and the type of carriers present. Our analysis software (WVASE32, J.A.Woollam Co., Lincoln, NE) has a large number of oscillators where the user can choose from. More than one type of oscillator can be combined to describe the interband and intraband transitions.

- **Point By Point Fit**

  In a point by point fit, calculations are performed at each point separately. This process causes noise in the generated data curve. Also, the results of this fit may not be Kramers-Kronig consistent.

- **B Spline Fit**

  Optical constants are fit using a set of control points that keep adjusting

up and down to match the experimental data. Just like the previous fitting method, this method might cause some noise in the generated curve since it takes a running average of the experimental data. The spacing of the nodes is a critical factor when applying this fit. A wide node spacing might cause some of the real peaks of the dielectric function to disappear. Therefore, the node spacing needs to be chosen carefully.

## 1.10 Experimental Procedure and Data Analysis

- **Measurement**

  Performing the experiment results in finding the intensities of the reflected and incident beams as well as ellipsometric angles $\psi$ and $\Delta$. This step starts by choosing the photon energy range at which the measurement is performed and the range of angles of incidence. The choice of the photon energy range and the angles of incidence depend on the sample studied. To ensure maximum accuracy of the ellipsometric measurement, the angles of incidence must be close to an angle called Brewster angle. This Brewster angle is the angle where the reflected light is completely s-polarized. Since the difference between $r_s$ and $r_p$ increases at this angle, sensitivity of the measurement also increases [5].

- **Model Developement**

  Since the optical constants of the material cannot be found directly from the optical measurement, a model has to be built to fit the experimental data. The choice of the model parameters depends mainly on the optical response of the material to the applied electric field. Some materials have well known optical constants that are already tabulated in the WVASE

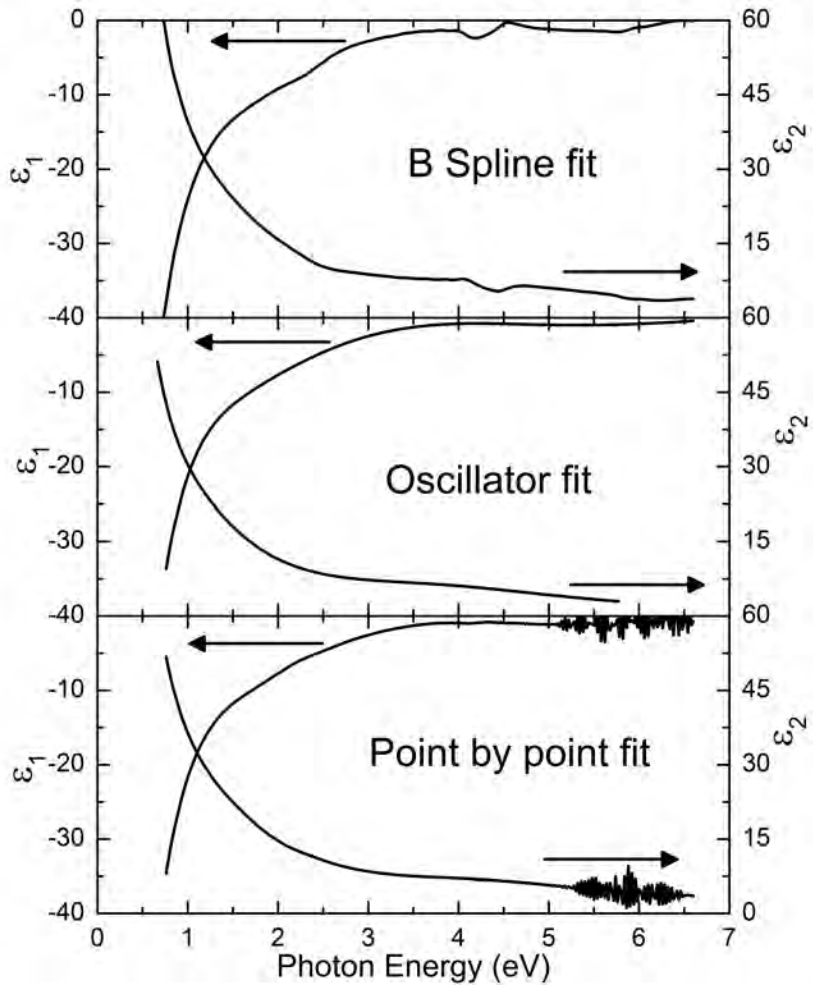


Figure 8: Several types of fits applied to a 10 nm thick $Ni_{1-x}Pt_x$ alloy layer on a thick thermal oxide on Si: Top: Basis spline (or B-spline) fit. Center: Oscillator fit with Drude and Lorentz oscillators. Bottom: Point by point fit. The point-by-point fit shows uncorrelated noise at each wavelength, especially in the UV. The B-spline fit shows wiggles related to the choice of spacing between nodes. The oscillator fit results in a smooth dispersion, but is biased by the number and type of oscillators selected for the fit. The B-spline and oscillator fits are Kramers-Kronig consistent by design, but the point-by-point fit is not.

software. For new materials whose optical constants are not investigated yet, an assumption is required. This assumption includes some parameters such as the thickness of the different layers in the sample, positions and values of oscillators, and surface conditions such as oxide layers or roughness.

- **Fitting Experimental Data**

  After building the model, the models parameters are varied until the experimental data match the generated data from the model. If the initially guessed optical constants and oscillator parameters are close to the real values of the material, the final result of the fit will represent the optical constants of the material.

- **Best Fit Evaluation**

  After obtaining what we believe to be the optical constants of the sample, we have to ensure that the fit is unique and that the models parameters are not strongly correlated. The fitting procedure can be repeated more than once until the minimum mean square error is achieved.

## 1.11 Variable Angle Spectroscopic Ellipsometry

Figure 9 shows the ellipsometer (J.A. Woollam VASE) setup used in obtaining the optical constants of materials. As the name indicates, the measurement is taken at different angles of incidence and over a wide range of photon energies.

- **Light Source and Monochromator**

  An Arc lamp is used in performing ellipsometric measurements because of the wide range of photon energies it emits. However, some of the challenges that are associated with the use of arc lamps are the difficulty of getting a collimated light beam as well as the low intensity arc lamps have compared

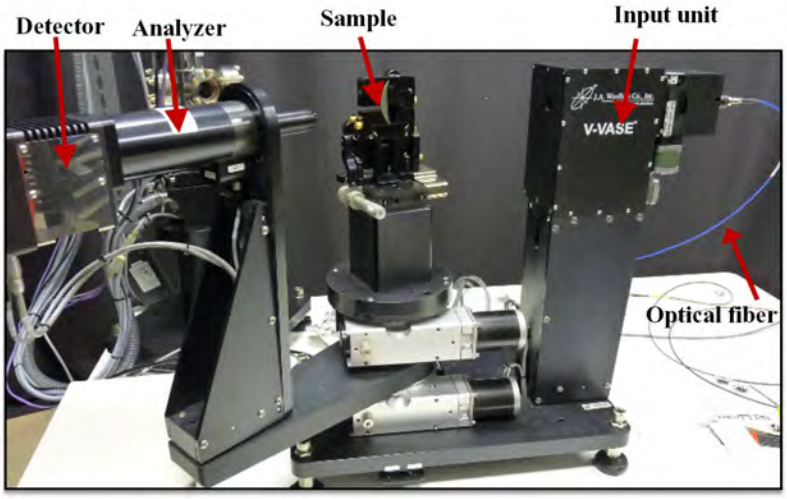


Figure 9: Optical components of our variable angle spectroscopic ellipsometer.

to other sources such as laser.

The monochromator uses a diffraction grating where a line of parallel grooves are separated by a regular spacing that is comparable to the wavelength of the light.

- **Optical fiber**

  An optical fiber is a flexible glass rod where light is forced to travel within. An optical fiber consists of a core surrounded by a cladding. The cladding has a lower refractive index than the core to ensure that light suffers total internal reflection whenever it hits the interface between the core and the cladding. Both the core and the cladding are covered with a plastic jacket for protection.

- **Input unit: Polarizer**

  A polarizer is placed in front of the light wave and is used to change the polarization state of an unpolarized light beam to be linearly polarized. It allows light with one certain linear electric field orientation to pass and

blocks all other orientations from passing.

- **Sample stage**

  The sample stage uses vaccum suction to hold the sample in place. Ellipsometry can also be used to measure optical properties of liquids. In this case, a special sample holder is required. We can also replace our sample holder with a variable-temperature cryostat, but this was not used for this work.

- **Analyzer**

  Analyzers and polarizers are basically the same since they both do the same job of converting the polarization state into linearly polarized light. The only difference is where each of them is placed. The rotating analyzer is placed in front of the detector.

- **Detector**

  The ellipsometer used in our measurements uses silicon and InGaAs photodiode detectors due to their sensitivity to different wavelengths. The InGaAs photodiode is used in the mid-infrared below the Si band gap, where the detection efficiency of the Si photodiode vanishes.

## 1.12 Infrared Spectroscopic Ellipsometry

- **Infrared Spectrum**

  Planck's law states that the energy of a photon is inversely proportional to the wavelength which means that longer wavelengths have lower energies and vice versa. Therefore, the energy of infrared light is not high enough to break the bonds between the bound electrons and the nucleus. Instead, it affects the molecular motions. Infrared light photon energies match

the molecular translational, vibrational, and rotational energies [8]. Unlike translational motion where the whole molecule changes position, vibrational motion causes atoms within the molecule to move without changing the average position of the molecule. In rotational motion, the molecule rotates around its center of mass without causing a shift in the molecule position. Vibrational motion is the most important motion seen in the infrared absorption spectrum of a crystal where translational and rotational motions are weak and hard to detect in the infrared absorption spectrum. For any molecule, the degrees of freedom determine the possible ways in which the molecule can move in. The number of degrees of freedom is determined by the molecular structure. Assuming that a molecule with N atoms is located in three dimensions, the number of degrees of freedom is 3N. This number corresponds to the potential motions of the molecule. Table 1 lists the different molecular motions and the corresponding degrees of freedom.

- **Infrared Regions**

  The infrared spectral region extends from 14,000 to 20 $cm^{-1}$ and is divided into three subregions, near (14,000 to 4000 $cm^{-1}$), middle (4000 to 400 $cm^{-1}$) and far-infrared (500 to 20 $cm^{-1}$). Most of the characterization applications use the middle infrared region [8].

- **Infrared Ellipsometry**

  A J.A. Woollam FTIR-VASE variable angle ellipsometer was used to perform measurements in the infrared between 250 and 8000 $cm^{-1}$ at the Center for Integrated Nanotechnologies user facility. Measurements were taken at three angles of incidence: 60°, 65°, and 70°.

Table 1: Molecular motions and their corresponding degrees of freedom.

| Motion | Degrees of freedom |
|---|---|
| Translation | 3 |
| Rotation | 3 (non-linear) |
| | 2 (linear) |
| Vibration | 3N-6 (non- linear) |
| | 3N-5 (linear) |

# 2 CMOS Processing and Silicide Contacts

## 2.1 Introduction to CMOS technology

Complementary metal oxide semiconductor (CMOS) transistor technology has been used in everyday applications such as computer processors or cell phone microchips. A CMOS transistor acts like a switch with two states: ON and OFF. CMOS transistors are used to process and store information. The revolution in the semiconductor industry over the last 40 years has led to CMOS transistors that are faster, cheaper, and smaller and consume less power. In order to improve the device operating speed through continuous scaling (Moore's Law), improvements in materials technology are required. Specifically, resistive and capacitive losses and time delays should be minimized [12].

In a CMOS transistor, see Fig. 10, current flows from one electrical contact (source) to another electrical contact (drain). A third electrical contact (gate) is made of a conducting material and is separated from the semiconductor channel by a thin layer of oxide. The gate acts as an input terminal that controls the current flow by modifying the voltage applied to the gate. This gate voltage should be high enough to lower the barrier between the source and the drain so current can flow (ON state). Otherwise, the CMOS transistor will be on the OFF state. Figure 10 shows a schematic diagram of a CMOS transistor.

In an integrated circuit, the silicon substrate is doped with foreign atoms to make it more conductive by adding free carriers. There are two types of Si doping, n-type and p-type. For n-type doping, silicon is implanted with a five valence electron element (e.g, phosphorus). For p-type doping, an element with only three valence electrons is added (e.g, boron).

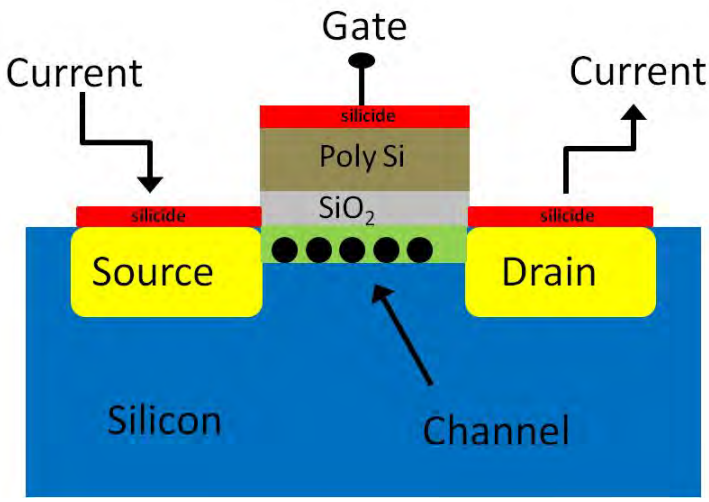


Figure 10: CMOS transistor with source, drain, and gate. Contact to these three terminals is made with a thin silicide layer (red). The gate (poly-Si) is separated from the Si channel (green) by a thin gate oxide (here: $SiO_2$).

Circuits built using complementary metal oxide semiconductor (CMOS) technology requires two types of metal oxide semiconductor field effect transistors (MOSFETs), called NMOS and PMOS. They have different doping and work in a complementary way. In NMOS transistors, the source and drain are made of n-type semiconductors, whereas the substrate and channel are made of a p-type semiconductor. PMOS transistors are the other way around.

In an NMOS transistor, electrons flow from the n-type region to the p-type region creating a depletion layer where electrons are depleted. The diffusion of the electrons from the n-type side to the p-type side makes the p-type side negative and repels any electrons trying to diffuse. This depletion layer acts as a barrier that prevents electrons from flowing through the transistor and the device will be in the OFF state. To turn the switch on, a positive voltage has to be applied to the gate causing the electrons to move from the n-type side and overcome the depletion layer by forming a conducting channel near the gate oxide.

## 2.2 CMOS Fabrication

The front-end CMOS fabrication process consists of four main modules. A brief description of each of these CMOS fabrication modules follows below. See also Figs. 10 and 11.

- Wafer cleaning

  The front-end CMOS fabrication process starts with cleaning the silicon substrate using HF and other acids or solvents to remove any impurities and contaminants that may be found on the Si surface and to get rid of the native oxide. Trenches are formed by etching and filled with $SiO_2$ to electrically isolate adjacent transistors and other devices.

- Active region formation

  This step dopes Si by ion implantation with either group three (to create NMOS) or group five (to create PMOS) elements to enhance conductivity. Photoresist and a mask are used to define the regions where the P and the N wells will be formed. The wafer is then transferred to a furnace which diffuses the dopants to a desired junction depth.

- Gate formation

  **Gate oxide formation**

  After the formation of the P and N wells, the Si surface is oxidized to form an $SiO_2$ gate oxide by thermal oxidation. Modern CMOS technologies also use a high-k metal oxide (e.g., $HfO_2$) instead of $SiO_2$ as the gate dielectric.

  **Gate deposition and patterning**

  Polycrystalline Si is deposited on top of the $SiO_2$ as a gate metal. (Highly doped semiconductors have similar properties as metals.) Modern technolo-

gies also use transition metal nitrides as the gate layer. The gate metal is removed by etching over the source, drain, and trench regions.

**Spacer formation and source-drain implantation**

This step is followed by the formation of a gate sidewall spacer (usually silicon nitride) and the implantation of the gate, source, and drain regions.

- SALICIDE process

  A metal silicide is formed over the source, drain, and gate regions by a solid state reaction process called SALICIDE, a term that stands for Self ALIgned siliCIDE. A blanket metal deposition (usually Ni or another transition metal such as Ti or Co) is applied and the wafer is heated up to form a silicide which acts as an Ohmic contact to the source, drain and gate, if the metal is in contact with a clean Si surface. The metal does not react over $SiO_2$ or silicon nitride (tranch or spacer) regions. The unreacted metal is removed by wet etching in a mixture of sulphuric acide and hydrogen peroxide (or aqua regia, if the silicide metal contains noble metals). More details of the formation of metal silicides will be illustrated later.

Figure 11 shows the front-end CMOS process steps from the formation of the N and P wells to silicide contact formation.

## 2.3 Metal Silicides

Metal silicides are used as contact materials between interconnecting copper lines and the silicon CMOS transistors [13, 14, 15]. Their special properties such as low sheet resistance, low junction leakage, no bridging across gate sidewall spacers and the low contact resistance when in contact with n- and p-type silicon, low formation temperature, the uniformity of the silicide layer formed, and their

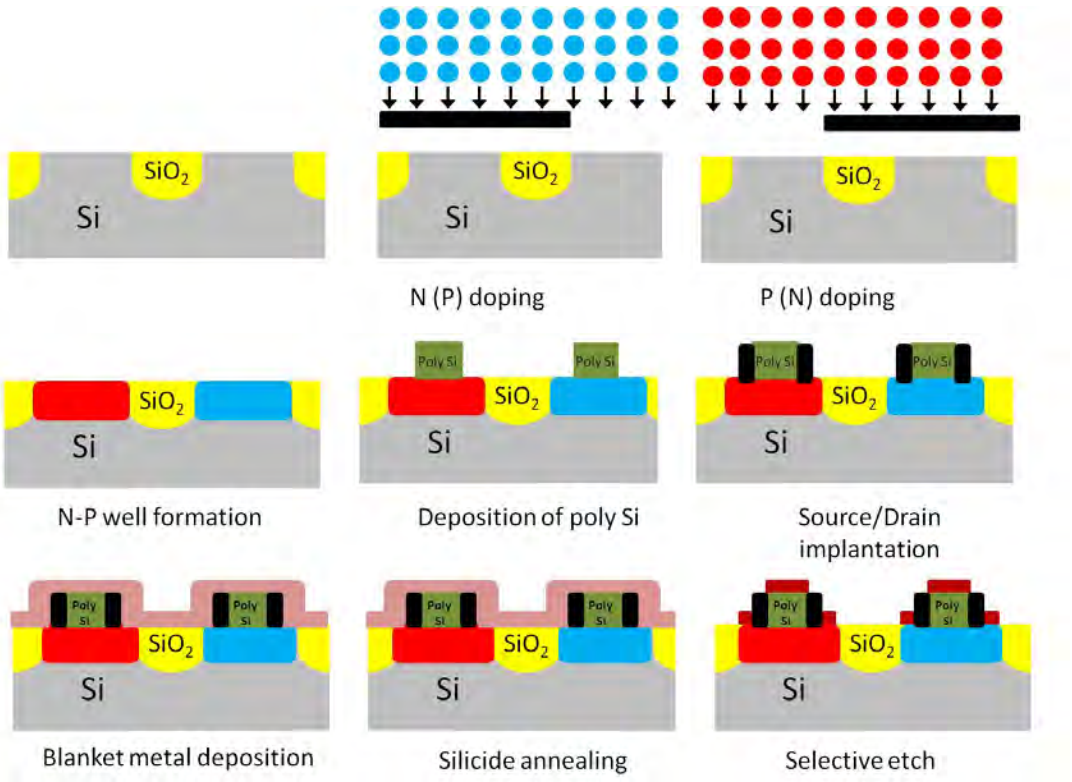


Figure 11: Front-end CMOS process steps from well implantation to silicide contact formation.

compatibility with silicon gate technology [16, 17] make them perfect for transistor applications.

Moore's law states that every two years, the number of transistors on a chip should double [18] which means that transistors need to shrink in size. The reduction in the MOSFET size causes the contact resistance to the Si drain and Si source to increase. This problem needs to be avoided in order to get a high performance transistor.

The metallic behavior of metal silicides helps to improve conductivity and to compensate for the resistance increase associated with the scaling of integrated circuits.

- **Metal Silicide Formation**

  SALICIDE is the most common silicide formation technique in a CMOS process flow. It starts with a clean silicon surface. A metal blanket layer is then deposited on top of a patterned silicon substrate. The metal/silicon system is thermally treated to stimulate the interaction (interdiffusion) between the metal and the silicon. A sufficient annealing temperature is needed so the metal is all consumed creating a metal silicide without melting the metal [19].

  Thermal annealing can be performed more than once depending on the silicide phase required for CMOS applications. As the annealing temperature increases, the silicide phase changes from being metal rich to silicon rich. New phases can also be obtained by increasing the annealing temperature or increasing the annealing time [20]. A metal-silicon binary phase diagram, see Fig. 12 as an example, shows the possible silicide phases during the silicide annealing. With increasing annealing thermal budget, silicide phases

form from left (pure metal) to the right.

Remaining unreacted metal can be removed by a wet etch.

- **Transition Metal Silicides**

  $TiSi_2$, $CoSi_2$ and NiSi are the most common silicides used in semiconductor manufacturing. $TiSi_2$ and $CoSi_2$ have long been the dominant silicides used in CMOS transistors. However, NiSi has been replacing $TiSi_2$ and $CoSi_2$ due to its low sheet resistance, low Si consumption, and low formation temperatures compared with $TiSi_2$ and $CoSi_2$ [21, 22]. The formation of nickel silicide is diffusion controlled whereas the formation of $TiSi_2$ and $CoSi_2$ is nucleation controlled. Diffusion controlled silicide formation results in smoother surfaces and narrower silicided gate lines [23, 24].

  There are two $TiSi_2$ phases in the Ti-Si system: The C49 phase has a base-centered orthorhombic structure with a resistivity of (60-90 $\mu\Omega$cm) and 12 atoms per unit cell. The C54 phase has a face-centered orthorhombic structure and a resistivity of (12-20 $\mu\Omega$cm) which makes it preferable for CMOS applications [25]. Since the C49 phase forms first [26], two annealing steps are needed to form a low resistivity $TiSi_2$ silicide, a problem that limits the use of $TiSi_2$ due to the difficulty of moving from the C54 to the C49 phase. Another problem associated with $TiSi_2$ is the high Si consumption which is not suitable for forming shallow junctions. Also, $TiSi_2$ does not form on narrow lines, since it is formed through a nucleation controlled process.

  To form the desired $CoSi_2$ silicide for CMOS applications, two steps must be followed. The first step is to convert the metal rich silicide to CoSi monosilicide at 400-500°C. The second annealing process converts the monosilide to $CoSi_2$. The use of $CoSi_2$ in CMOS transistors is limited due to the fact that

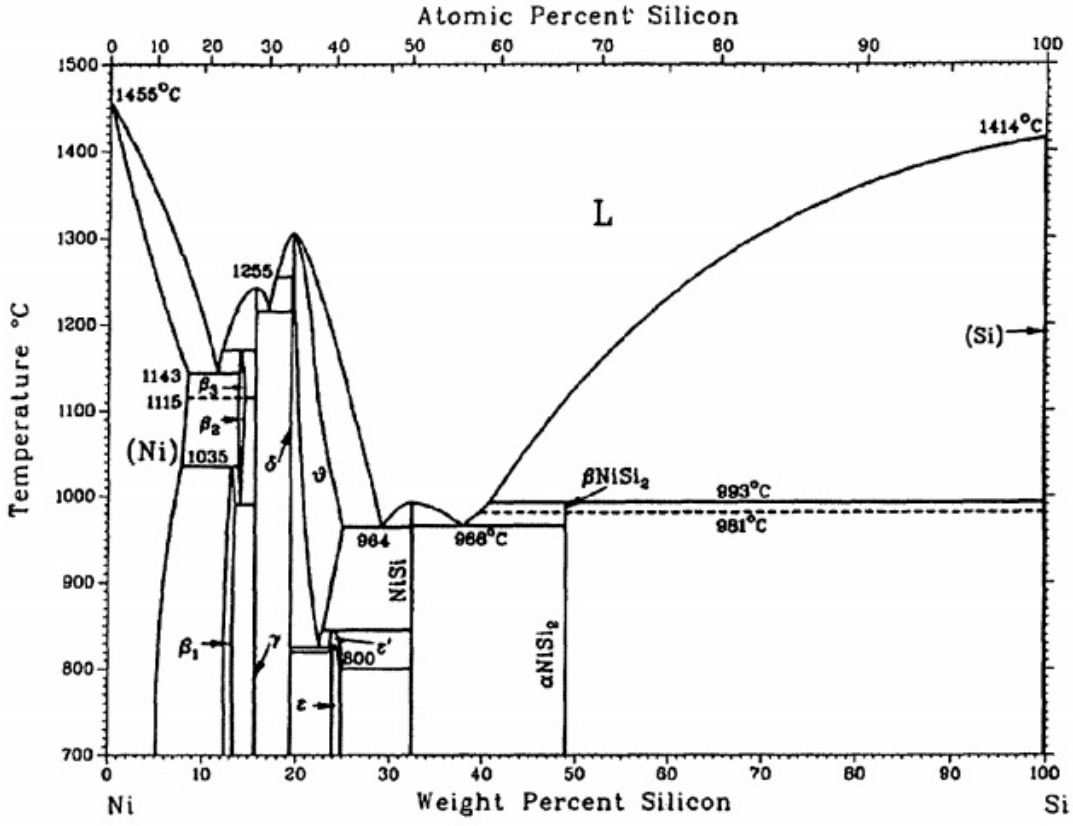


Figure 12: Ni-Si phase diagram.

$CoSi_2$ is sensitive to surface contaminations which might result in a rough silicide/Si interface. Another limitation is the easy oxidation of the $CoSi_2$ when annealed in ambient environment. These issues related to contaminations result in a high resistivity.

Table 2 lists the properties of the different transition metal silicides. Even though NiSi monosilicides have special properties that make them suitable for CMOS applications, a thin NiSi is unstable at high temperatures. Two types of instabilities are observed, agglomeration and the formation of $NiSi_2$ [23, 27]. Both instabilities need to be avoided due to their high resistivity.

Table 2: A comparison between the different silicides used in CMOS transistors

| Property | $CoSi_2$ | $TiSi_2$ | NiSi |
|---|---|---|---|
| Resistivity ($\mu\Omega$cm) | 15-20 | 15-20 | 10.5-15 |
| Si consumed per nm of metal | 3.6 nm | 2.3 nm | 1.8 nm |
| Formation temperature (°C) | 500 | 750 | 250-400 |
| Melting temperature (°C) | 1326 | 1500 | 992 |

## 2.4 NiSi System

Due to their advantages shown in Table 2, NiSi monosilicides have been replacing $CoSi_2$ and $TiSi_2$ in integrated circuit applications [28]. However, their instability at high temperatures makes it challenging to use them as Ohmic contacts in CMOS transistors. The Ni-Si phase diagram (see Fig. 12) shows that the Ni-Si system is rather complex with seven metal rich phases beyond the NiSi monosilicide phase [23]. The Ni-Si phase diagram is shown in Fig. 12 [29]. The phase diagram shows the low melting temperature of NiSi monosilicides compared to the other Ni silicide phases.

Figure 13 shows the steps of nickel silicide formation with the different nickel silicide phases formed at each temperature. A nickel film is sputtered on top of a bare silicon surface. At room temperature, before any thermal treatment is applied, some nickel atoms will already diffuse into the silicon. As the annealing temperature is increased, more nickel will diffuse into the silicon and new phases will be created. $Ni_2Si$ is created at 280°C. After all the nickel has been consumed, monosilicides will be formed at 350°C. Heating the sample up to 750°C will result in forming $NiSi_2$. The graph shows that as the temperature increases, the nickel silicide is transformed from being metal rich to silicon rich. Among the different Ni-Si phases, only the NiSi phase has the lowest resistivity [17] and can be formed at a temperature range from 300-700°C [30].

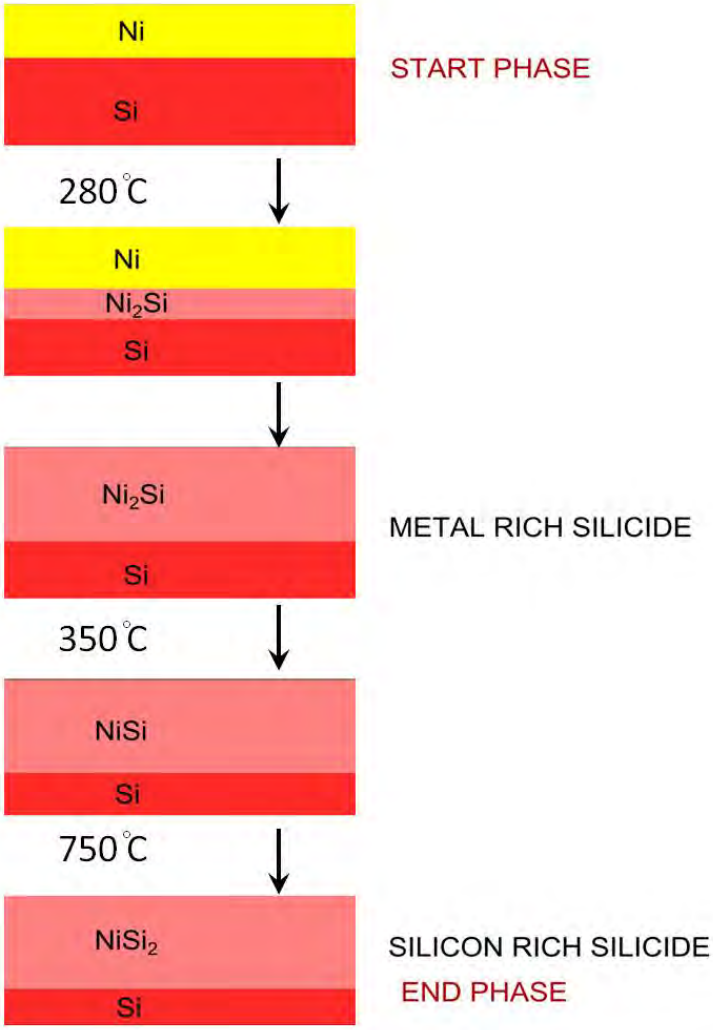


Figure 13: Steps involved in nickel silicide formation by annealing at different temperatures. The NiSi monosilicide is the phase desired for CMOS applications and the formation of the silicon-rich $NiSi_2$ must be avoided.

## 2.5 Effect of Pt Addition on NiSi Stability

In order to solve the problems associated with NiSi applications in integrated circuits at high temperatures, the formation of $NiSi_2$ has to be delayed. Lavoie and co-workers [23] studied the effect of adding several alloying elements to Ni monosilicides on the thermal and morphological stability of these monocilicides.

It was reported that the addition of a small amount of Pt (5%) is able to push the formation of $NiSi_2$ to 900°C. The reason why adding Pt helps to thermally stabilize NiSi is the fact that Pt is miscible in NiSi but not in $NiSi_2$. Pt being insoluble in $NiSi_2$ requires that Pt should be repelled from the $NiSi_2$ nucleation sites whenever $Ni_{1-x}Pt_xSi$ is formed. Solutions with complete solubility always result in higher entropy and this is not the case with the $Ni_{1-x}Pt_xSi_2$ formation. Therefore, as we increase the Pt content in the $Ni_{1-x}Pt_x$ alloys, the total entropy of the system decreases which reduces the driving force of the reaction and the $Ni_{1-x}Pt_xSi_2$ nucleation barrier becomes higher.

In summary, adding Pt to NiSi stabilizes the Ohmic contacts to CMOS devices. Adding Pt delays disilicide formation and improves the uniformity of thin NiSi layers by delaying agglomeration. The purpose of this thesis is therefore to investigate the electronic and optical structure of $Ni_{1-x}Pt_x$ alloys and their silicides. Specifically, knowing the optical constants (complex dielectric function) of $Ni_{1-x}Pt_x$ and $Ni_{1-x}Pt_xSi$ alloys the use of spectroscopic ellipsometry for inline thickness measurements of metal alloys and their silicides.

# 3 Compositional Dependence of the Optical Conductivity of $Ni_{1-x}Pt_x$ Alloys ($0<x<0.25$) Determined by Spectroscopic Ellipsometry

This article appears in Thin Solid Films as it is shown here and will be published later this year in the volume covering the proceedings of the $6^{th}$ International Conference on Spectroscopic Ellipsometry held in Kyoto, Japan from May 26, 2013 through May 31, 2013.

Lina S. Abdallah, Stefan Zollner
Department of Physics, New Mexico State University, MSC 3D, P.O. Box 30001, Las Cruces, NM 88003-8001, USA

Christian Lavoie
IBM Research Division, T.J. Watson Research Center, P.O. Box 218, Yorktown Heights, NY 10598

Ahmet Ozcan
IBM Systems and Technology Group, Hopewell Junction, NY 12533

Mark Raymond
GLOBALFOUNDRIES, 255 Fuller Rd., Albany, NY 12203

## 3.1 Abstract

We measured the ellipsometric angles as a function of photon energy from 0.76 to 6.6 eV of 10 nm thick $Ni_{1-x}Pt_x$ alloy ($0<x<0.25$) films deposited on thick thermal oxides. Using basis spline functions and Drude-Lorentz oscillator fitting, we determined the dielectric functions and optical conductivities of our alloy films. We describe techniques to increase the accuracy of our measurements and data analysis. We find absorption peaks near 1.6 and 4.8 eV due to interband optical transitions. There is a significant broadening of these peaks with increasing Pt content. Annealing the metals at 500°C for 30 s increases the optical conductivity.

## 3.2 Introduction

The optical properties of many semiconductors and insulators have been determined with high accuracy and over a broad spectral range using experimental techniques such as spectroscopic ellipsometry, the minimum-deviation prism method, and transmission and reflection measurements [31]. Many semiconductors and insulators can be prepared as high-purity single crystals. They are often very stable in air and form only thin native oxides. A small amount of surface roughness can be considered in the interpretation of the spectra. The complex refractive index $n$ and the complex dielectric function $\epsilon = n^2$ have been tabulated for many semiconductors and insulators [31].

The complex dielectric functions of metals are less well known than those of insulators and semiconductors [31], because it is hard to achieve comparable purity and crystallinity in metals. Metals can be deposited on various substrates (especially glass or $SiO_2$ on Si) as poly-crystalline films by evaporation, sputtering, electro-plating, or chemical vapor deposition. Single-crystalline metals are rare. Therefore, the optical response of metal films will depend on the deposition technique and parameters such as grain size, texture, film thickness, impurity content, etc. [32]. Many metals (especially alkali metals and rare earths) are highly reactive. Therefore, the optical constants of noble and near-noble metals such as Au, Ag, and Pt are known with the highest accuracy.

Our present work describes measurements to determine the optical constants of Ni and $Ni_{1-x}Pt_x$ alloys as a function of composition ($0<x<0.25$), where $x$ is measured in atomic percent. To be consistent, most of our alloys were deposited as thin films (10 nm thickness) on thermal oxides by physical vapor deposition (sputtering). We find interesting physics related to the interactions of the $d$-bands

in Ni and Pt, which lead to a broadening of the interband optical transitions in $Ni_{1-x}Pt_x$ alloys with increasing Pt content.

Our choice of film thickness and composition is motivated by the application of similar alloys as Ohmic contacts in modern complementary metal-oxide-semiconductor (CMOS) device processing. Our results enable inline optical thickness measurements of metal contact layers using spectroscopic ellipsometry, the most common film thickness measurement technique in the semiconductor industry. In the visible spectral range, metals have penetration depths comparable to our film thickness (10 nm). We will describe specific experimental strategies to determine the optical constants of such thin films with high accuracy. We carefully discuss experimental artifacts and how to identify or reduce them.

### 3.3 Sample Preparation

Most of our $Ni_{1-x}Pt_x$ films were deposited on two-side polished Si wafers with 300 mm diameter. Thick transparent $SiO_2$ layers were first grown as thermal oxides on the Si substrates. For convenience, we chose an oxide thickness of 200 nm, since such thermal oxides can easily be grown on front-end CMOS processing equipment. The transparent oxide below the absorbing metal thin film enhances the information available through variable-angle spectroscopic ellipsometry, since the optical path length in the oxide varies with the angle of incidence [33]. We retained one bare, unprocessed Si substrate and one wafer with thick $SiO_2$ thermal oxide as reference materials. To avoid reflections of light below the Si band gap from the back surface of the wafer [5] (which is incoherent with the light reflected from the front surface and leads to depolarization of the reflected beam), the back surfaces of the wafers were roughened with a sandblaster using alumina abrasive [5, 34, 35].

$Ni_{1-x}Pt_x$ films with varying compositions ($0<x<0.25$, measured as an atomic percentage) were sputtered on the thermal oxide using a commercial DC magnetron sputtering tool for 300 mm Si wafers. The wafer was kept at room temperature during deposition. Typical deposition pressures are on the order of 1 mTorr. We chose a film thickness of 10 nm, which is similar to Ni films used in CMOS device processing. The composition was varied by co-sputtering simultaneously from two targets with compositions of $Ni_{0.9}Pt_{0.1}$ and $Ni_{0.7}Pt_{0.3}$. The deposition rate was on the order of 1 Å/s (about 100 times slower than in the work by Johnson and Christy [36], where samples were prepared by evaporation), resulting in a deposition time of about 2 min for a 100 Å thick film.

The thicknesses and compositions of the $Ni_{1-x}Pt_x$ films were measured using x-ray reflectivity (XRR), x-ray fluorescence [37], and sheet resistance measurements. XRR [37, 22] also showed that the surface layer (oxide and roughness) thickness for similar films was on the order of 15 Å. The $Ni_{1-x}Pt_x/SiO_2$ interface is very stable. Ni diffusion in $SiO_2$ or nickel silicate formation can be neglected at temperatures below 600°C, which was confirmed by XRR measurements [37]. To investigate the influence of thermal processing on the optical constants of $Ni_{1-x}Pt_x$ alloys, some samples were annealed. The most common annealing conditions were heating to 500°C for 30 s.

### 3.4 Experimental Methods

Spectroscopic ellipsometry [4, 5, 38] measures the Jones ratio

$$\rho\left(E,\phi\right) = r_p/r_s = \left(\tan\psi\right)e^{i\Delta} \tag{32}$$

versus photon energy $E$ and angle of incidence $\phi$. $r_p$ and $r_s$ are the complex Fresnel reflectance ratios for p- and s-polarized light. $\psi$ and $\Delta$ are known as the

ellipsometric angles. Under ideal conditions, the reflected beam should be totally polarized, if the incident beam is linearly or elliptically polarized. In practice, some of the reflected intensity is unpolarized even for total polarization of the incident beam. This is known as depolarization. It can be caused by incoherent reflections from the back surface (which we eliminated by roughening the backside of our wafers), by film thickness variations (on the order of 2% across the beam spot for our samples and measurement conditions), by the focusing of the incident beam on the sample, or by the bandwidth of the monochromator (about 2 nm for our measurements) [5].

We acquired $\psi$ and $\Delta$ and the depolarization on a vertical variable-angle-of-incidence rotating-analyzer ellipsometer with a computer-controlled Berek wave-plate compensator [39]. We varied the incidence angles between 20° and 80°. The detector and optics are suitable for measurements from 0.5 to 6.6 eV, but the choice of the optical fiber between the monochromator and the polarizer-sample-analyzer assembly limits spectra to the IR range (0.5 to 4.5 eV) or the UV range (0.76 to 6.6 eV). This instrument uses a triple-grating, double-chamber Czerny-Turner monochromator with 160 mm focal length. The monochromator has variable entrance and middle slits (0 to 2000 $\mu$m). The exit slit width is determined by the diameter of the optical fiber used to connect the monochromator with the goniometer base of the ellipsometer (usually 200 $\mu$m). In the visible and UV spectral range, the linear dispersion of the monochromator is 2.3 nm/mm with 1200 lines per mm ruled gratings. We usually chose a step size of 20 meV. These data sets required about 24 hours for data acquisiton on one sample. Typical spectra are shown in Figs. 14 and 15.

Figure 15 shows the depolarization of the reflected beam (as a percentage of total reflected intensity) versus photon energy for various monochromator en-

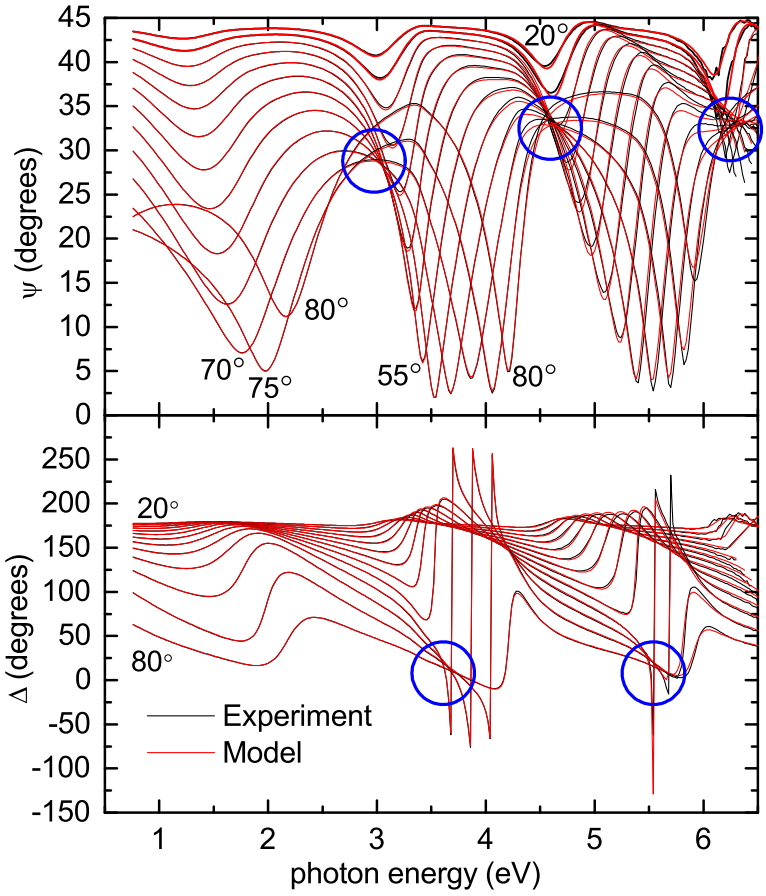


Figure 14: Ellipsometric angles $\psi$ and $\Delta$ as a function of photon energy for a 10 nm thick $Ni_{1-x}Pt_x$ alloy ($x$=0.1) on 220 nm oxide deposited on an undoped Si substrate, acquired with incidence angles ranging from 20° to 80°. Experimental data are shown in comparison with fits to the data using a Drude-Lorentz oscillator for the Ni-Pt optical constants. The circles show focal points, where $\psi$ or $\Delta$ is independent of incidence angle (for large angles). The incidence angle $\phi$ is indicated for some spectra.

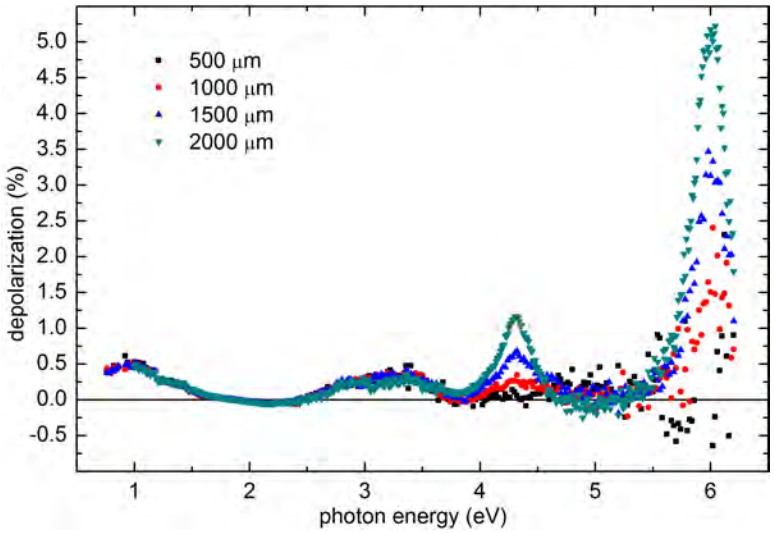


Figure 15: Depolarization of the reflected beam as a function of photon energy for $Ni_{0.75}Pt_{0.25}$ annealed at 500°C (30 s) for 70° angle of incidence and different slit widths ranging from 500 to 2000 $\mu$m.

trance/middle slit widths. It can be seen that the dominant source of the depolarization in the UV is the dispersion of the monochromator. The depolarization can be reduced significantly with a monochromator entrance/middle slit width of 1 mm, which corresponds to a spectral resolution of 2.3 nm. Reducing the entrance/middle slit width further increases the noise in the spectra, as shown in Fig. 15. Given these results, all our spectra were acquired with an entrance/middle slit width of 1 mm. This reduces the depolarization peaks at 4.3 and 6 eV. The origin of the depolarization peaks at 1 and 3.5 eV is not known. These peaks were not affected by the monochromator slit width or other experimental parameters. Similar depolarization peaks are found for a thick oxide on Si (without Ni), but they disappear in thick Ni films or on a bare Si substrate and therefore are related to interference effects.

Figure 14 shows the ellipsometric angles for an as-deposited 10 nm thick $Ni_{1-x}Pt_x$ alloy ($x$=0.1) on $SiO_2$. $\psi$ is always below 45°, which indicates that

$|r_p| < |r_s|$ for all energies and incidence angles. (For a bare oxide film without Ni, $\psi$ reaches peaks close to 90°.) The $\psi$ spectrum shows minima (interference fringes) near 2 eV, 4 eV, and 5.5 eV. They originate from the thick $SiO_2$ layer below the metal. The fringes shift with the incidence angle due to variations in the path length. Small incidence angles (near-normal conditions) only yield shallow $\psi$ minima, while large incidence angles (above 40°) result in steep $\psi$ minima. Since we observe strong interference effects (with $\psi$ almost reaching zero) over the entire spectral range, we conclude that the 10 nm thick metal film is essentially transparent over the entire spectral range. (Thicker Ni films absorb more light and therefore show shallower $\psi$ minima or none at all.) An interesting feature in the $\psi$ and $\Delta$ spectra is marked by the circles: At three specific photon energies (3 eV, 4.5 eV, and 6.2 eV), $\psi$ is independent of the incidence angle (for sufficiently shallow incidence). This leads to a "focal point" in the $\psi$ data. At the same photon energies, the depolarization is largest, see Fig. 15. We expect large systematic errors at these energies in our optical properties for $Ni_{1-x}Pt_x$. Our broad range of incidence angles and the thick $SiO_2$ layer below the metal film enhance the interference effects and thus reduce systematic errors or confine them to a narrow range of photon energies [33]. Similar focal points are also observed in the $\Delta$ spectra at 3.5 and 5.5 eV.

### 3.5 Data Analysis Methods

The ellipsometric angles shown in Fig. 14 can be calculated from Maxwell's equations governing the propagation of electromagnetic waves and their reflection by stratified planar structures (Fresnel equations), with the optical constants of all layers (at each wavelength) and the layer thicknesses as parameters [4, 5, 38]. In our case, the thin-film structure consists of a Si substrate, a $SiO_2$ layer

Table 3: Summary of Drude-Lorentz parameters, see Eq. (33), for 10 nm thick $Ni_{1-x}Pt_x$ alloys. For all films, $E_3$=11 eV and $\Gamma_3$=0. Films with annealing conditions marked "yes" were annealed at 500°C for 30 s. Thicknesses $t_{Ni-Pt}$ and $t_{SiO_2}$ are given in Å. All energies and broadenings are in units of eV. $\sigma_0$ was calculcated from Eq. (36) and is given in $1/\Omega$cm. Amplitudes are dimensionless except for $A_4$, which is in units of $eV^2$. The number of significant digits is based on 90% confidence limits.

| $x$ | ann | $E_P$ | $\Gamma_d$ | $\sigma_0$ | $A_1$ | $E_1$ | $\Gamma_1$ | $A_2$ | $E_2$ | $\Gamma_2$ | $A_4$ | $A_3$ | $t_{Ni-Pt}$ | $t_{SiO_2}$ |
|---|---|---|---|---|---|---|---|---|---|---|---|---|---|---|
| 0 | no | 6.2 | 1.07 | 4832 | 9.9 | 1.80 | 2.74 | 4.67 | 4.68 | 2.94 | 8.1 | 1.38 | 113.6 | 1934.7 |
| 0.10 | no | 7.1 | 1.07 | 6310 | 7.4 | 1.62 | 1.74 | 4.88 | 4.82 | 5.54 | 8.7 | 1.01 | 119.5 | 2288.1 |
| 0.10 | yes | 6.9 | 0.95 | 6720 | 10.4 | 1.60 | 1.94 | 4.89 | 4.80 | 5.30 | 9.3 | 1.04 | 116.4 | 2338.4 |
| 0.15 | no | 7.5 | 1.15 | 6550 | 4.9 | 1.58 | 1.48 | 6.12 | 4.86 | 7.33 | 8.4 | 0.90 | 120.9 | 2290.2 |
| 0.15 | yes | 7.4 | 1.07 | 6860 | 7.1 | 1.59 | 1.68 | 6.31 | 4.81 | 6.93 | 9.3 | 1.00 | 115.7 | 2332.6 |
| 0.20 | no | 7.6 | 1.15 | 6730 | 4.3 | 1.57 | 1.41 | 6.9 | 4.87 | 8.5 | 8.2 | 0.86 | 118.0 | 2266.5 |
| 0.20 | yes | 7.5 | 1.11 | 6790 | 5.3 | 1.57 | 1.51 | 7.2 | 4.72 | 7.8 | 9.0 | 0.95 | 114.6 | 2325.3 |
| 0.25 | no | 7.7 | 1.19 | 6680 | 4.5 | 1.61 | 1.54 | 6.4 | 4.81 | 7.8 | 8.9 | 0.99 | 116.9 | 2058.2 |
| 0.25 | yes | 7.9 | 1.20 | 6970 | 4.2 | 1.58 | 1.39 | 7.5 | 4.84 | 8.8 | 10.2 | 0.95 | 112.2 | 2151.2 |

(approximately 220 nm thick), and the $Ni_{1-x}Pt_x$ alloy (approximately 10 nm thick). The optical constants of Si and $SiO_2$ are well known [40]. In theory, it should be possible to determine the optical constants of $Ni_{1-x}Pt_x$ at each photon energy and the layer thicknesses from the data by numerical inversion of Fresnel's equations. In practice, this is difficult, because one finds systematic, numerical, as well as random errors. For example, critical points in the Si substrate will appear in the $Ni_{1-x}Pt_x$ optical constants, if film thicknesses are inaccurate (in the model) or vary across the surface [41]. Similarly, interference fringes in the ellipsometric angles can also cause errors in the optical constants of our films. We reduce this source of errors by varying the angles of incidence over a broad range. Usually, there is at least one suitable angle of incidence where $\psi$ and $\Delta$ vary smoothly with photon energy. This incidence angle provides a stable numerical solution to Fresnel's equations and accurate optical constants for $Ni_{1-x}Pt_x$.

Two techniques are commonly used to determine accurate optical constants of thin films, oscillator models and basis spline fits.

- **Drude-Lorentz Oscillator Model**

  The complex dielectric function $\epsilon = \epsilon_1 + i\epsilon_2$ versus photon energy $E$ for $Ni_{1-x}Pt_x$ alloys can be written in the following functional form known as the Drude-Lorentz model: [5, 22, 42, 43, 44]

$$\epsilon(E) = 1 - \frac{E_P^2}{E(E + i\Gamma_d)} + \sum_{j=1}^{3} \frac{A_j E_j^2}{E_j^2 - E^2 - i\Gamma_j E} - \frac{A_4}{E^2} \qquad (33)$$

  The first term describes the permeability of vacuum. The second term (Drude term) with parameters $E_P$ and $\Gamma_d$ (related to the density per unit volume and scattering time of free carriers) describes the response of free carriers to the electromagnetic wave. Typical values for Ni are $E_P$=7 eV

and $\Gamma_d$=1 eV, but exact values are highly model-dependent (including the photon energy range and number of Lorentz oscillators) and not physically meaningful. The sum of Lorentz oscillators in the third term describes the response of bound electrons with dimensionless oscillator strength $A_j$, resonance energy $E_j$, and damping constant $\Gamma_j$. Two oscillators near 1.5 eV ($j$=1) and 4.9 eV ($j$=2) are usually sufficient to achieve a good fit to our data. Adding a third oscillator does not significantly improve the quality of the fit for $Ni_{1-x}Pt_x$ alloys. Instead, we add two poles (Lorentz oscillators with $\Gamma_j$=0) at 0 eV ($j$=4) and in the vacuum-UV (arbitrarily chosen at 11 eV, $j$=3) to account for optical absorption outside of our spectral range, including d-interband transitions at low energies. These poles only influence the real part, not the imaginary part of the dielectric function. A pole at 0 eV (with zero broadening, last term) together with a Drude oscillator with a finite broadening (second term) essentially includes the possibility that the Drude scattering time is frequency dependent [45]. Put differently, Drude claimed that the optical properties of metals pointed to at least two different kinds of charged particles which could move freely in the metals he studied [42]. A suitable set of fit parameters is shown in Table 3, but we do not claim that these parameters are unique. Using these parameters, the mean square difference between the data and the model is typically 5-7 times larger than the experimental measurement errors for $\psi$ and $\Delta$. The broadening $\Gamma_d$ of the Drude term is related to the free electron relaxation time $\tau$ through Heisenberg's uncertainty relation $\Gamma_d\tau = \hbar$, but see the warning above that the parameters are usually model-dependent. Our Drude broadenings are similar to those shown in Ref. [22]. The Fermi velocity $v_f = l/\tau$, where $l$ is the carrier mean free path [46]. We expect that our metals are rather

"dirty" and scattering is dominated by impurities and grain boundaries [47], obscuring the ideal behavior of scattering in a Fermi liquid [48].

Expanding the optical constants of a transition metal as in Eq. (33) is dangerous and requires care. First, such an expansion is only valid over a specific photon energy range (which must be specified if parameters are reported). Second, the parameters may have no physical meaning. For example, in the case of transition metals the Fermi energy splits the d-bands into occupied and unoccupied states. Therefore, d-interband optical transitions are allowed at arbitrarily low energies. There is no energy range where a Drude model gives a good description of the optical constants. Third, a numerical solution of Fresnel's equations forces one to choose starting values for the parameters in Eq. (33). A peak may simply appear in our optical constants because of our choice of starting parameters or the number of Lorentz oscillators for the fit. Finally, strong correlations exist between some fit parameters and therefore a set of parameters (such as those given in Table 3) is usually not unique. An expansion as in Eq. (33) should only be attempted if approximate values of the optical constants and the general shape of $\epsilon(E)$ are known.

If we neglect the last term in Eq. (33), we note that $\epsilon - 1$ diverges as $E^{-1}$ for low photon energies. To avoid this divergence, one defines the complex optical conductivity

$$\sigma(E) = -i\frac{\epsilon_0}{\hbar}\left[\epsilon(E) - 1\right]E, \tag{34}$$

where $\epsilon_0$ is the permittivity of vacuum and $\hbar$ the reduced Planck's constant.

In our Drude-Lorentz form (38), the conductivity becomes

$$\frac{\hbar\sigma\left(E\right)}{\epsilon_0}=\frac{iE_P^2}{E+i\Gamma_d}-\sum_{j=1}^{3}\frac{iEA_jE_j^2}{E_j^2-E^2-i\Gamma_jE}+\frac{iA_4}{E} \tag{35}$$

The pole in the last term is clearly outside of the realm of the Drude model, but it is required to fit our data for Ni. This term is not needed for noble metals such as silver or gold [46, 47, 49]. It is clearly unphysical, because the imaginary part of the DC conductivity diverges. This pole does not affect the real part of $\sigma$.

At zero photon energy ($E$=0), $\sigma$ becomes equal to the DC conductivity. From our fits (and ignoring the pole in the last term, which only affects the imaginary part of the DC conductivity), we calculate

$$\sigma_0=\sigma\left(E=0\right)=\frac{\epsilon_0}{\hbar}\frac{E_P^2}{\Gamma_d}\approx 4800\left(\Omega\text{cm}\right)^{-1}, \tag{36}$$

which is about 30 times lower than the bulk conductivity of pure nickel at room temperature, $\sigma_0$=1.43×10$^5$ $(\Omega\text{cm})^{-1}$, see Ref. [9]. Therefore, our ellipsometry technique is not representative to determine the conductivity of transition metals, as should be expected because of the contribution of d-intraband transitions to the optical absorption. The values calculcated from Eq. (36) increase with Pt concentration, see Table 3, whereas the electrical DC conductivity of $Ni_{1-x}Pt_x$ alloys drops from 1.43×10$^5$ $(\Omega\text{cm})^{-1}$ for $x$=0 to 0.3×10$^5$ $(\Omega\text{cm})^{-1}$ for $x$=0.3 as shown in Ref. [50]. The slow dependence of $\sigma_0$ with Pt variation is another argument that our optical conductivity is determined by optical transitions and not dominated by the Drude term (DC conductivity).

For comparison, a factor of 5 of the electrical to the optical (extrapolated)

DC conductivity $\sigma_0$ was found for copper by Johnson and Christy [45]. For Ni, this discrepancy is expected to be larger, because the nickel d-intraband transitions are dominant throughout our spectral range and free-electron effects are negligible [45]. This statement needs to be reconsidered at lower photon energies using infrared ellipsometry.

The complex conductivity $\sigma$, the complex dielectric function $\epsilon = n^2$, and the complex refractive index $n$ are all equivalent descriptions of the optical constants of a material.

- **Basis Spline Fits**

  The second technique to determine accurate optical constants does not assume a functional form as in Eq. (33), but allows the optical constants to vary freely as a function of wavelength. We enforce some wavelength-to-wavelength correlation by expanding $\epsilon$ using cubic basis spline functions [51] with a control point spacing between 0.1 and 0.4 eV. Results are shown in Fig. 16. The finite control point spacings avoid numerical instabilities and systematic errors at specific wavelengths. For a control spacing of 0.1 eV, we find structures in $\sigma$ near 4.3 and 6.0 eV, which coincide with the depolarization peaks (Fig. 15) and the focal points in the $\psi$ spectra (Fig. 14). These structures are clearly numerical artifacts. We conclude that there is only one broad peak in $\sigma$ between 3 and 6.5 eV. We approximately describe this peak with a control point spacing of 0.4 eV, which mostly eliminates the artificial structures.

  On the other hand, a control point spacing of 0.1 eV yields a reasonable dispersion of $\sigma$ below 3 eV. The shoulder at 1.5 eV is also observed in other data [36]. A control point spacing of 0.4 eV leads to a non-physical decrease

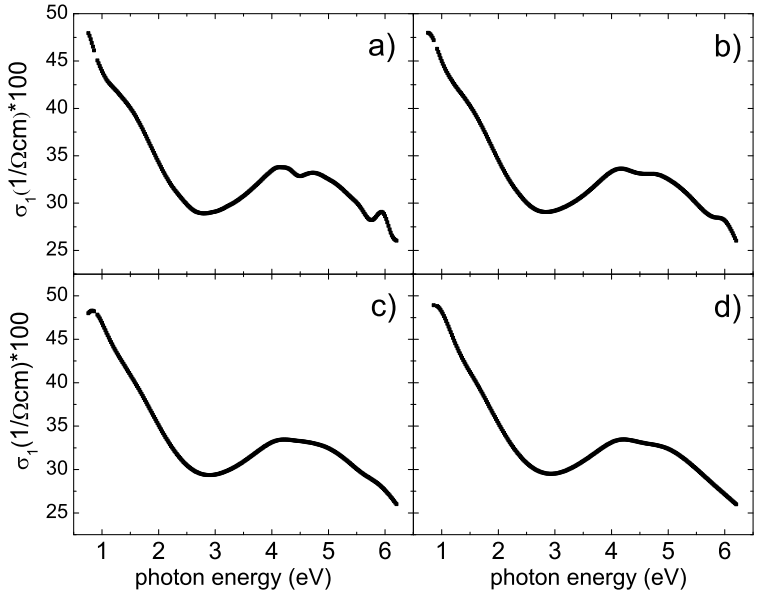


Figure 16: Real part of the optical conductivity for a 10 nm thick $Ni_{0.9}Pt_{0.1}$ alloy film on thermal oxide, calculated from the ellipsometric angles using cubic basis spline fits with different control point spacings of (a) 0.1 eV, (b) 0.2 eV, (c) 0.3 eV, and (d) 0.4 eV.

of $\sigma_1$ at the lowest energies. This decrease is due to termination problems of the basis spline functions at the high and low ends of our spectral range [51]. This problem can be avoided by choosing a sufficiently small control point spacing.

The basis spline technique (with 0.1 eV control spacing below 3 eV and with 0.4 eV spacing above 3 eV), see Fig. 16, gives us strong confidence in the overall shape of $\sigma$ versus photon energy. We now proceed to fit our ellipsometric angles with the Drude-Lorentz oscillator model in Eq. (33) described above.

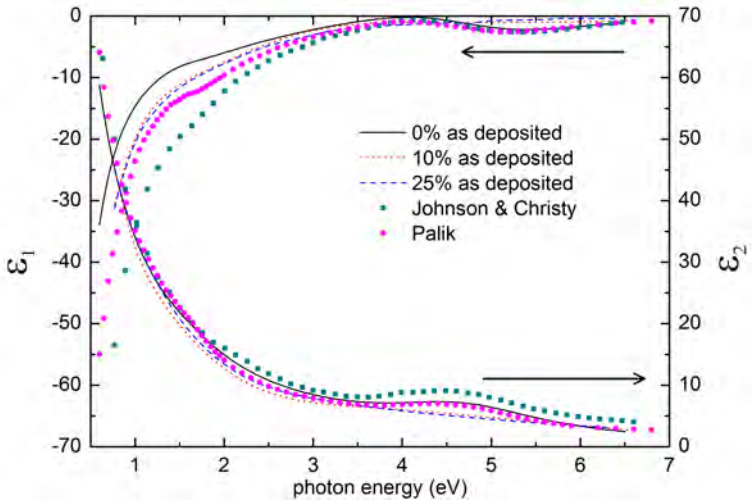


Figure 17: Lines: Real and imaginary parts of the dielectric functions versus photon energy for as-deposited 10 nm thick $Ni_xPt_{1-x}$ alloy films on thermal oxide, calculated from the ellipsometric angles using Drude-Lorentz oscillator fits for $x$=0 (solid), 0.1 (dotted), and 0.25 (dashed). Symbols: Literature data from Refs. [32] (Palik) and [36] (Johnson & Christy).

### 3.6 Experimental Results and Discussion

We acquired the ellipsometric angles $\psi$ and $\Delta$ and the depolarization for our 10 nm thick $Ni_{1-x}Pt_x$ alloy samples for $x$=0, 0.1, 0.15, 0.2, and 0.25 as shown in Fig. 14 and 15. We first determined the film thicknesses and the optical constants using a basis spline fit. We then fitted the same experimental data with the Drude-Lorentz model as in Eq. (33) and verified that both techniques yielded the same thicknesses and optical conductivities (except for artifacts in both methods). We also determined that the metal thickness was unique. (A good fit could not be achieved when changing the thickness by more than 10 Å. Since refractive index and thickness are correlated, this limits the absolute accuracy of our optical constants to about 10%.)

The resulting dielectric functions for as-deposited $Ni_{1-x}Pt_x$ alloys determined from our films are shown in Fig. 17 for $x$=0, 0.1, and 0.25. Our values of $\epsilon_2$ for

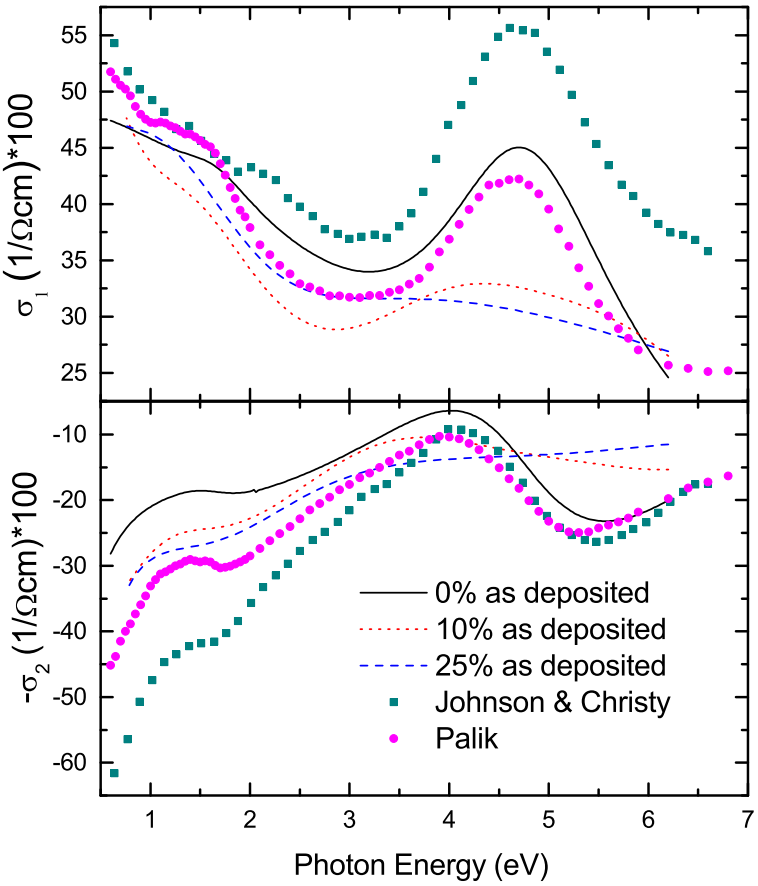


Figure 18: Same data as in Fig. 17, but displayed as optical conductivity, see Eq. (34).

pure Ni are in excellent agreement with those tabulated by Lynch and Hunter. [32] Because of the strong divergence of $\epsilon_2$ at low energies, the structure at 1.5 eV is not visible in the $\epsilon_2$ data. On the other hand, there clearly is a peak at 4.5 eV in $\epsilon_2$, which broadens with Pt addition. Johnson and Christy [36] found slightly higher values of $\epsilon_2$ in the UV than our work.

Large differences between our data and those in Refs. [32] and [36] exist for $\epsilon_1$ in the visible and infrared spectral ranges. Our data diverge much less rapidly at low photon energies. In addition to the valley at 5 eV (compare the peak in the $\epsilon_2$ spectra already noted) all $\epsilon_1$ data sets for pure Ni show a structure near 1.7 eV.

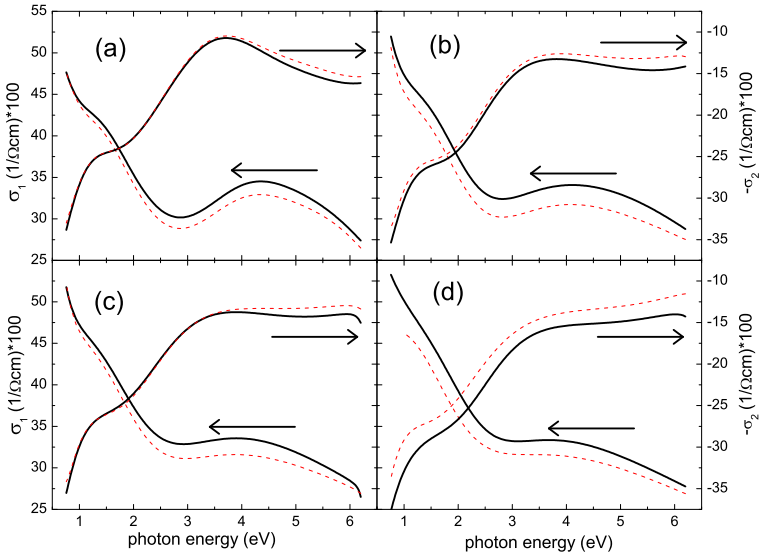


Figure 19: Complex optical conductivity for 10 nm thick $Ni_xPt_{1-x}$ alloy films as deposited (dotted) and after annealing at 500°C for 30s (solid), with Pt concentrations of (a) 10%, (b) 15%, (c) 20%, and (d) 25%.

These structures disappear as Pt is added. We note that the dielectric functions in Refs. [32] and [36] were determined by reflectance followed by Kramers-Kronig transformation. We expect that our ellipsometry results are more accurate. At the same near-IR photon energy (say, 1 eV), $\epsilon_1$ is smaller for $Ni_{1-x}Pt_x$ alloys than for pure Ni, while $\epsilon_2$ is about the same. This can be explained with different IR pole contributions for different $x$, which corresponds to a difference in d-interband transitions below our spectral range (non-Drude IR absorption).

In Fig. 18, we show the same data as in Fig. 17, but displayed as the complex optical conductivity. This representation shows the variations between different data sets more clearly. For example, the gradual increase in the broadening of the UV absorption at 4.5 eV with increasing Pt content is very apparent. In Table 3, this corresponds to an increase of $\Gamma_2$.

In Fig. 19, we summarize the optical conductivity for all four $Ni_{1-x}Pt_x$ alloys. Dotted lines show data for the as-deposited films, while solid lines show data

for pieces of the same films that were annealed at 500°C for 30 s. As expected, the optical conductivity is higher after annealing because of larger grain size and healing of defects.

### 3.7 Conclusions and Future Work

We have determined the optical constants (complex dielectric function and optical conductivity) of 10 nm thin $Ni_{1-x}Pt_x$ films from 0.76 to 6.6 eV using variable-angle spectroscopic ellipsometry. We critically discuss various data acquisition and analysis procedures. Our results are expected to be more accurate than previous reflectance measurements followed by Kramers-Kronig transform. The peaks due to interband transitions observed at 1.6 and 4.8 eV broaden significantly with increasing Pt content.

Future work will include a comparison of our experimental results with *ab initio* band structure calculations for Ni and $Ni_3Pt$. In our present work, we have ignored surface overlayer effects, because their influence on our optical constants is small. We believe, however, that our fits to the data can be improved slightly by including surface effects. Considering surface roughness alone does not improve the fit. Instead, we will investigate the impact of a native oxide and study the optical constants of bulk NiO. We will also study the validity of our Drude-Lorentz oscillator model with infrared ellipsometry measurements on our films. Finally, we plan to determine the optical constants of nickel-platinum-silicides with ellipsometry measurements of $Ni_{1-x}Pt_x$ alloys deposited directly on Si.

### 3.8 Acknowledgments

We are grateful to V.W. Kamineni and A.C. Diebold for offline discussions about Ref. [22]. This work was supported by the National Science Foundation

(DMR-1104934).

# 4 Optical Conductivity of $Ni_{1-x}Pt_x$ Alloys ($0<x<0.25$) from 0.76 to 6.6 eV

This article was published in AIP Advances, volume **4**, 017101 (2014).

Lina S. Abdallah, Tarek M. Tawalbeh, Igor V. Vasiliev, Stefan Zollner
Department of Physics, New Mexico State University, MSC 3D, P.O. Box 30001, Las Cruces, NM 88003-8001, USA

Christian Lavoie
IBM Research Division, T.J. Watson Research Center, P.O. Box 218, Yorktown Heights, NY 10598

Ahmet Ozcan
IBM Systems and Technology Group, Hopewell Junction, NY 12533

Mark Raymond
GLOBALFOUNDRIES, 255 Fuller Rd., Albany, NY 12203

## 4.1 Abstract

Using spectroscopic ellipsometry and Drude-Lorentz oscillator fitting, we determined the dielectric function and optical conductivity versus photon energy from 0.76 to 6.6 eV of 10 nm thick $Ni_{1-x}Pt_x$ alloy ($0<x<0.25$) films deposited on thick thermal oxides. We find absorption peaks near 1.6 and 5.0 eV due to interband optical transitions. There is a significant broadening of the UV peak with increasing Pt content, since the bandwidth of the 3d electrons in Ni is smaller than that of the 5d bands in Pt. Our experimental observation is consistent with *ab initio* calculations of the density of states for Ni, Pt, and the $Ni_3Pt$ compound. Annealing the metals at 500°C for 30 s increases the optical conductivity.

## 4.2 Introduction

The optical properties of many semiconductors and insulators have been determined with high accuracy and over a broad spectral range using experimental techniques such as spectroscopic ellipsometry, the minimum-deviation prism

method, and transmission and reflection measurements [31]. Many semiconductors and insulators can be prepared as high-purity single crystals. They are often very stable in air and form only thin native oxides. A small amount of surface roughness can be considered in the interpretation of the spectra. The complex refractive index $n$ and the complex dielectric function $\epsilon = n^2$ have been tabulated for many semiconductors and insulators [31].

The complex dielectric functions of metals are less well known than those of insulators and semiconductors, because it is hard to achieve comparable purity and crystallinity in metals. Metals can be deposited on various substrates (especially glass [52] or $SiO_2$ on Si) as poly-crystalline films by evaporation, sputtering, electro-plating, or chemical vapor deposition. Single-crystalline metals are rare [53]. Therefore, the optical response of metal films will depend on the deposition technique and parameters such as grain size, texture, film thickness, deposition rate, impurity content, etc [32].

Our present work describes the optical constants of Ni and $Ni_{1-x}Pt_x$ alloys as a function of composition ($0<x<0.25$), where $x$ is measured in atomic percent. To be consistent, most of our alloys were deposited as thin films (10 nm thickness) on thermal oxides by physical vapor deposition (sputtering). We find interesting physics related to the interactions of the $d$-bands in Ni and Pt, which lead to a broadening of the interband optical transitions in $Ni_{1-x}Pt_x$ alloys with increasing Pt content. We interpret our experimental results in comparison with *ab initio* density functional theory band structure calculations.

Many metals (especially alkali metals and rare earths) are highly reactive. Therefore, the optical constants of noble and near-noble metals such as Au, Ag, and Pt are known with the highest accuracy. Our previous analysis of $Ni_{1-x}Pt_x$ alloys [54] ignored surface effects. In this work, we also consider possible surface

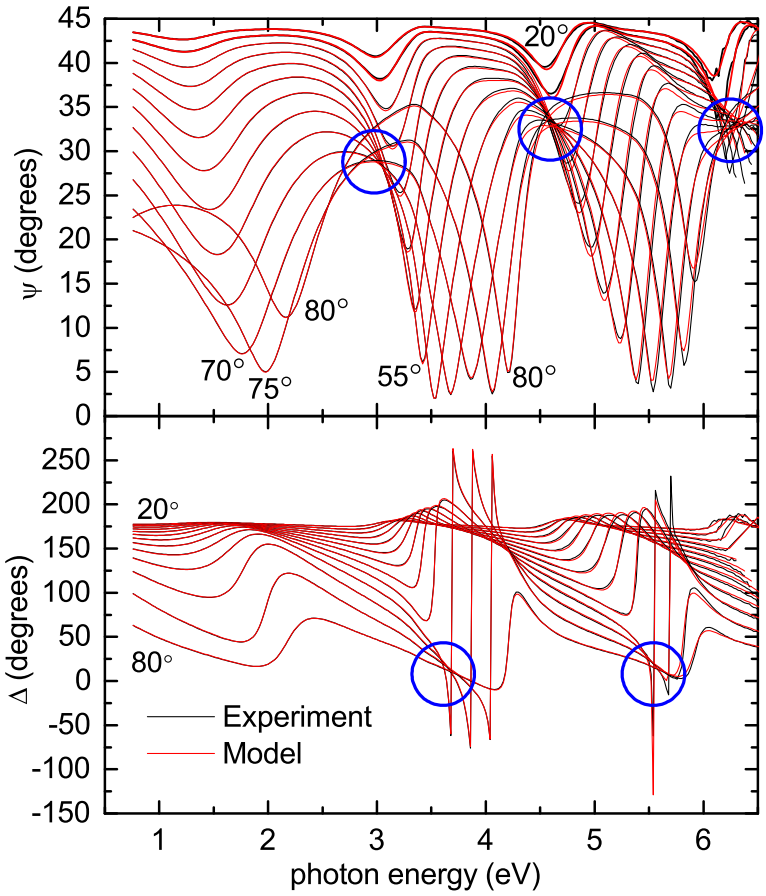


Figure 20: Ellipsometric angles $\psi$ and $\Delta$ as a function of photon energy for a 10 nm thick $Ni_{1-x}Pt_x$ alloy ($x$=0.1) on 220 nm oxide deposited on an undoped Si substrate, acquired with incidence angles ranging from 20° to 80°. Experimental data are shown in comparison with fits to the data using a Drude-Lorentz oscillator model for the Ni-Pt optical constants (without surface corrections). Small differences between data and model can be seen above 4 eV due to surface effects. The circles show focal points, where $\psi$ or $\Delta$ is independent of incidence angle (for large angles). The incidence angle $\phi$ is indicated for some spectra.

overlayers and find that our data can be fit best with a thin layer of water covering our metal films.

While most previous work on Ni was based on reflection and transmission measurements (usually followed by Kramers-Kronig analysis to determine the dielectric function), we used spectroscopic ellipsometry, which allows the simultaneous determination of the real and imaginary part of the dielectric function by line shape fitting. Previous results for the optical constants of Ni have been critiqued by Lynch and Hunter [32]. The most important measurements are calorimetric absorption by Lynch and coworkers [55] on single-crystalline Ni at 4 K in the infrared and visible (up to 3 eV), UV reflectance measurements on evaporated films by Johnson and Christy[36] and in situ UV reflectance by Vehse and Arakawa.[52] Early polarimetric measurements on a polycrystalline disk were carried out by Stoll [56, 57]. More recent ellipsometry measurements on Ni films have been performed by Kamineni *et al.*[22] and by Losurdo *et al.*[58]

Our choice of film thickness and composition is motivated by the application of similar alloys as Ohmic contacts in modern complementary metal-oxide-semiconductor (CMOS) device processing. Our results enable inline optical thickness measurements of metal contact layers using spectroscopic ellipsometry, the most common film thickness measurement technique in the semiconductor industry.

### 4.3 Sample Preparation

Most of our $Ni_{1-x}Pt_x$ films were deposited on two-side polished Si wafers with 300 mm diameter. Thick transparent $SiO_2$ layers were first grown as thermal oxides on the Si substrates. For convenience, we chose an oxide thickness of 200 nm, since such thermal oxides can easily be grown on front-end CMOS processing

equipment. The transparent oxide below the absorbing metal thin film enhances the information available through variable-angle spectroscopic ellipsometry, since the optical path length in the oxide varies with the angle of incidence [33]. The oxide also prevents reaction of the metal films with the Si substrate (silicide formation).

$Ni_{1-x}Pt_x$ films with varying compositions ($0<x<0.25$, measured as an atomic percentage) were sputtered on the thermal oxide using a commercial DC magnetron sputtering tool. The wafer was kept at room temperature during deposition. Typical deposition pressures are on the order of 1 mTorr. We chose a film thickness of 10 nm, which is similar to Ni films used in CMOS device processing. The composition was varied by co-sputtering simultaneously from two targets with compositions of $Ni_{0.9}Pt_{0.1}$ and $Ni_{0.7}Pt_{0.3}$. The deposition rate was on the order of 1 Å/s (about 100 times slower than for evaporated films[52, 36]), resulting in a deposition time of about 2 min for a 100 Å thick film.

The thicknesses and compositions of the $Ni_{1-x}Pt_x$ films were measured using x-ray reflectivity (XRR), x-ray fluorescence (XRF) [37], and sheet resistance measurements. XRR[37, 22] also showed that the surface layer (oxide and roughness) thickness for similar films was on the order of 15 Å. This was also confirmed by atomic force microscopy. The $Ni_{1-x}Pt_x/SiO_2$ interface is very stable. Ni diffusion in $SiO_2$ or nickel silicate formation can be neglected at temperatures below 600°C, which was confirmed by XRR measurements [37]. To eliminate backside reflections in ellipsometry measurements, the back surface was roughened with alumina sand, followed by rinsing the wafer with water to remove the sand.

For comparison, we also investigated pure Ni films with thicknesses ranging from 5 nm to 100 nm, sputter-deposited on single-side polished undoped four-inch Si wafers covered with thick oxide, and bulk poly-crystalline Ni obtained

commercially. To investigate the influence of thermal processing on the optical constants of $Ni_{1-x}Pt_x$ alloys, some samples were annealed. The most common annealing conditions were heating to 500°C for 30 s.

### 4.4 Experimental Methods

Spectroscopic ellipsometry[4, 5, 38] measures the Jones ratio

$$\rho\,(E,\phi) = r_p/r_s = (\tan\psi)\,e^{i\Delta} \tag{37}$$

versus photon energy $E$ and angle of incidence $\phi$. $r_p$ and $r_s$ are the complex Fresnel reflectance ratios for p- and s-polarized light. $\psi$ and $\Delta$ are known as the ellipsometric angles [5]. We acquired $\psi$ and $\Delta$ and the depolarization on a vertical variable-angle-of-incidence rotating-analyzer ellipsometer with a computer-controlled Berek waveplate compensator [39]. Details have been described elsewhere [54].

Figure 20 shows the ellipsometric angles for an as-deposited 10 nm thick $Ni_{1-x}Pt_x$ alloy ($x$=0.1) on $SiO_2$. $\psi$ is always below 45°, which indicates that $|r_p| < |r_s|$ for all energies and incidence angles. (For a bare oxide film without Ni, $\psi$ reaches peaks close to 90°.) The $\psi$ spectrum shows minima (interference fringes) near 2 eV, 4 eV, and 5.5 eV. They originate from the thick $SiO_2$ layer below the metal. The fringes shift with the incidence angle due to variations in the path length. Small incidence angles (near-normal conditions) only yield shallow $\psi$ minima, while large incidence angles (above 40°) result in steep $\psi$ minima. Since we observe strong interference effects (with $\psi$ almost reaching zero) over the entire spectral range, we conclude that the 10 nm thick metal film is essentially transparent. (Thicker Ni films absorb more light and therefore show shallower $\psi$ minima or none at all.)

## 4.5 Data Analysis Methods

The ellipsometric angles shown in Fig. 20 can be calculated from Maxwell's equations governing the propagation of electromagnetic waves and their reflection by stratified planar structures (Fresnel equations), with the optical constants of all layers (at each wavelength) and the layer thicknesses as parameters [5, 4, 38]. In our case, the thin-film structure consists of a Si substrate, a $SiO_2$ layer (approximately 220 nm thick), the $Ni_{1-x}Pt_x$ alloy (about 10 nm thick), and a surface layer (see below). The optical constants of Si and $SiO_2$ are well known [40].

To determine the optical constants of the metal film, we proceed in two steps [54]. We first expand the metal optical constants with Kramers-Kronig consistent cubic splines (for 0.1 and 0.4 eV basis steps) with variable spline coefficients to obtain the general shape of dispersion and absorption [51]. These results guide the second step, where we use a Drude-Lorentz oscillator model as described by Eq. (38). The parameters used to fit the ellipsometric angles are therefore the oxide, metal, and surface layer thicknesses and the oscillator parameters.

The influence of surface effects (oxide and roughness) on the optical spectra is small, but measurable (especially in the UV), see Fig. 20. We were unable to achieve improvements to our fits by describing the surface layer as surface roughness (an effective medium consisting of 50% voids and 50% metal) or a native oxide with optical constants similar to bulk NiO [59]. On the other hand, we obtained very good fits (where the mean square deviation between the data and model was on the same order of magnitude as the experimental error) using a transparent surface layer with a small refractive index.

We therefore model the surface layer using the optical constants of water

[60, 61]. Other adsorbed atmospheric molecular contaminants have similar optical constants. (Our metal films were rinsed with water after roughening the back side of our wafers. Also, many months passed between deposition and ellipsometry measurements.) We did not observe a water peak [62] in FTIR ellipsometry measurements on our metal films, but such a peak would be marginal for a 25 Å thick film of water. In situ ellipsometry measurements under high vacuum ($10^{-7}$ Torr) conditions show that the water layer thickness can be reduced significantly by annealing in vacuum at 700 K for one hour, followed by an overnight cool-down to 300 K, see Fig. 21. An ozone clean at 150°C has a similar effect as the vacuum degas.

The complex dielectric function $\epsilon = \epsilon_1 + i\epsilon_2$ versus photon energy $E$ for $Ni_{1-x}Pt_x$ alloys (and other metals) can be written in the following functional form known as the Drude-Lorentz model:[44, 42, 43, 5, 22]

$$\epsilon(E) = 1 - \frac{E_P^2}{E(E + i\Gamma_d)} + \sum_{j=1}^{3} \frac{A_j E_j^2}{E_j^2 - E^2 - i\Gamma_j E} - \frac{A_4}{E^2} \tag{38}$$

The first term describes the permeability of vacuum. The second term (Drude term) with parameters $E_P$ and $\Gamma_d$ (related to the density per unit volume and scattering time of free carriers) describes the response of free carriers to the electromagnetic wave. Typical values for the plasma frequency $E_P$ and the broadening parameter $\Gamma_d$ of Ni-Pt alloys are $E_P$=7 eV and $\Gamma_d$=0.9 eV, respectively, but exact values are highly model-dependent (including the photon energy range, number of Lorentz oscillators, and surface corrections) and not physically meaningful.

The sum of Lorentz oscillators in the third term describes the response of bound electrons with dimensionless oscillator strength $A_j$, interband transition energy $E_j$, and damping constant $\Gamma_j$. Two oscillators near 1.6 eV ($j$=1) and 5.0

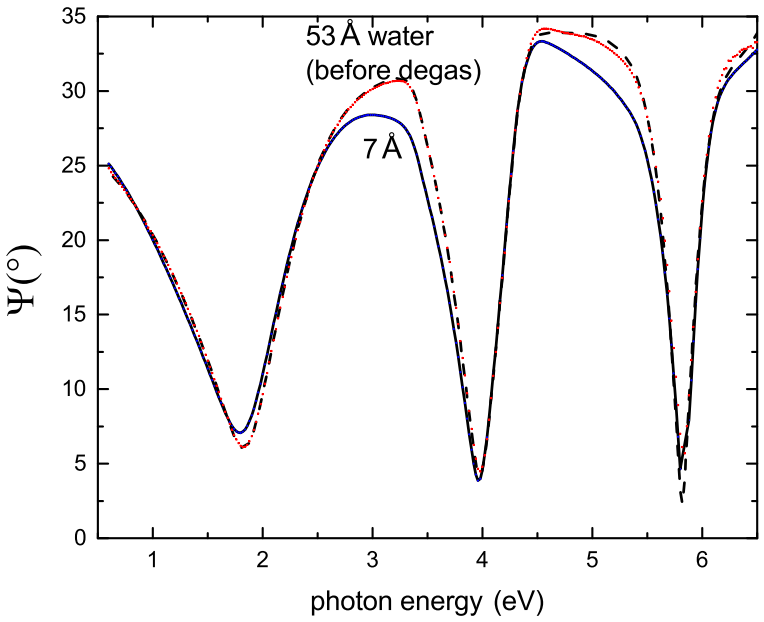


Figure 21: Ellipsometric angle $\psi$ of 100 Å of Ni:Pt on $SiO_2$ measured at a 70° incidence angle under UHV conditions. Dashed: Immediately after loading, modeled using a Drude-Lorentz layer for Ni:Pt with 53 Å of water on the surface. Solid: After annealing to 700 K for 12 hours, followed by a cool-down to 300 K (degas). This reduces the water layer to 7 Å thickness. It can be seen that the water layer increases the peak to valley ratio in the interference fringes. Symbols show experimental data, lines simulated data based on a multi-layer model consisting of Si, $SiO_2$, Ni, and water.

eV ($j$=2) are usually sufficient to achieve a good fit to our data. Adding a third oscillator does not significantly improve the quality of the fit for $Ni_{1-x}Pt_x$ alloys. (We did not observe the small peaks between 2 and 2.5 eV mentioned by Stoll [56, 57].) Instead, we add two poles (Lorentz oscillators with $\Gamma_j$=0) at 0 eV ($j$=4) and in the vacuum-UV (arbitrarily chosen at 11 eV, $j$=3) to account for optical absorption outside of our spectral range, including d-interband transitions at low energies. These poles only influence the real part, not the imaginary part of the dielectric function. A pole at 0 eV (with zero broadening, last term) together with a Drude oscillator with a finite broadening (second term) essentially includes the possibility that the Drude scattering time is frequency dependent [45]. Put differently, Drude claimed that the optical properties of metals pointed to at least two different kinds of charged particles which could move freely in the metals he studied [42]. For example, it is well known that the Fermi surface of Ni has several components made up of itinerant d and s electrons with different Fermi velocities [63, 64]. A suitable set of Drude-Lorentz parameters obtained from fitting our data is shown in Table 4, but we do not claim that these parameters are unique. Instead of placing the IR pole at 0 eV, we also attempted fits with a pole at 0.3 eV (where transitions were observed by Ehrenreich *et al.*[63] and Lynch *et al.*[55]), but this does not agree with our data below 1 eV.

The broadening $\Gamma_d$ of the Drude term is related to the free electron relaxation time $\tau$ through Heisenberg's uncertainty relation $\Gamma_d\tau = \hbar$, but see the warning above that the parameters are usually model-dependent. Our Drude broadenings are similar to those shown in Ref. [22], since our samples are quite similar. The Fermi velocity $v_f = l/\tau$, where $l$ is the carrier mean free path [46]. For a broadening parameter $\Gamma_d$=0.9 eV (see Table 4), the scattering time $\tau$=0.7 fs. Combined with the Fermi velocity in Ni of $0.3\times10^6$ m/s (see Refs. [63] and [64]), we obtain

an "optical" mean free path $l$=2.1 Å, much smaller than our film thickness and the expected grain size [22]. The "electrical" zero-frequency mean free path was found to be about 20 Å from lifetime broadenings observed in high-resolution photoemision measurements [64]. We expect that our metals are rather "dirty" and scattering is dominated by impurities, interfaces, and grain boundaries [47], obscuring the ideal behavior of scattering in a Fermi liquid [48].

From Eq. (38), it is possible to find the contribution to the long-wavelength dielectric constant by bound electrons (interband electronic transitions). In a semiconductor, this quantity is called $\epsilon_\infty$, while $\epsilon_b$ is a more common notation for metals. Removing the Drude term and the pole at 0 eV (free-carrier optical response) in Eq. (38) and setting $E = 0$, we find

$$\epsilon_\infty = \epsilon_b = 1 + A_1 + A_2 + A_3, \tag{39}$$

which is also tabulated in Table 4. This result is clearly model-dependent. Our results are influenced by the lower end of the spectral range of our instrument (0.7 eV). Measurements to lower energies using FTIR ellipsometry would result in larger values of $\epsilon_\infty$, since interband transitions also occur below the spectral range of our instruments, as reported by Lynch and coworkers [55].

If we neglect the last term in Eq. (38), we note that $\epsilon - 1$ diverges as $E^{-1}$ for low photon energies. To avoid this divergence, one defines the complex optical conductivity[63]

$$\sigma(E) = -i\frac{\epsilon_0}{\hbar}\left[\epsilon(E) - 1\right]E, \tag{40}$$

where $\epsilon_0$ is the permittivity of vacuum and $\hbar$ the reduced Planck's constant. In

Table 4: Summary of Drude-Lorentz parameters, see Eq. (38), for 10 nm thick $Ni_{1-x}Pt_x$ alloys. For all films, $E_3$=11 eV and $\Gamma_3$=0. Films with annealing conditions marked "yes" were annealed at 500°C for 30 s. Thicknesses $t_{\mathrm{Ni-Pt}}$ and $t_{SiO_2}$ are given in Å. All energies and broadenings are in units of eV. $\sigma_0$ was calculcated from Eq. (42) and is given in $1/\Omega$cm. $\epsilon_\infty$ was calculated from Eq. (39). Amplitudes are dimensionless except for $A_4$, which is in units of $eV^2$. The number of significant digits is based on 90% confidence limits. A preliminary version of this Table (without water surface corrections) has been published previously [54]

| $x$ | ann | $E_P$ | $\Gamma_d$ | $\sigma_0$ | $A_1$ | $E_1$ | $\Gamma_1$ | $A_2$ | $E_2$ | $\Gamma_2$ | $A_4$ | $A_3$ | $\epsilon_\infty$ | $t_{\mathrm{Ni-Pt}}$ | $t_{SiO_2}$ | $t_{H_2O}$ |
|---|---|---|---|---|---|---|---|---|---|---|---|---|---|---|---|---|
| 0 | no | 6.8 | 0.80 | 7799 | 13.6 | 1.73 | 3.00 | 5.12 | 4.98 | 3.17 | 7.75 | 1.69 | 21.4 | 101 | 1924 | 33 |
| 0.10 | no | 6.7 | 0.77 | 7817 | 16.6 | 1.59 | 2.35 | 4.49 | 4.93 | 4.96 | 7.72 | 1.39 | 23.5 | 111 | 2279 | 25 |
| 0.10 | yes | 6.7 | 0.76 | 7920 | 18.6 | 1.59 | 2.45 | 4.51 | 4.89 | 4.75 | 9.18 | 1.45 | 25.6 | 107 | 2330 | 25 |
| 0.15 | no | 7.1 | 0.83 | 8144 | 13.9 | 1.58 | 2.17 | 5.79 | 5.03 | 6.73 | 7.10 | 1.27 | 21.9 | 111 | 2280 | 28 |
| 0.15 | yes | 7.2 | 0.84 | 8275 | 14.7 | 1.58 | 2.03 | 5.91 | 4.90 | 6.40 | 8.50 | 1.31 | 22.9 | 108 | 2325 | 21 |
| 0.20 | no | 7.4 | 0.86 | 8538 | 11.9 | 1.56 | 2.03 | 7.02 | 5.09 | 8.33 | 6.89 | 1.16 | 21.1 | 108 | 2256 | 28 |
| 0.20 | yes | 7.3 | 0.86 | 8309 | 13.2 | 1.57 | 2.11 | 6.99 | 4.90 | 7.40 | 8.30 | 1.30 | 22.5 | 105 | 2316 | 27 |
| 0.25 | no | 7.6 | 0.91 | 8511 | 9.5 | 1.55 | 1.86 | 8.20 | 5.10 | 9.67 | 9.69 | 1.10 | 19.8 | 106 | 2048 | 30 |
| 0.25 | yes | 7.9 | 0.98 | 8539 | 8.3 | 1.55 | 1.72 | 8.85 | 5.05 | 9.89 | 9.90 | 1.08 | 19.2 | 103 | 2144 | 24 |

our Drude-Lorentz form (38), the conductivity becomes

$$\frac{\hbar\sigma\left(E\right)}{\epsilon_0}=\frac{iE_P^2}{E+i\Gamma_d}-\sum_{j=1}^{3}\frac{iEA_jE_j^2}{E_j^2-E^2-i\Gamma_jE}+\frac{iA_4}{E} \tag{41}$$

The pole in the last term is clearly outside of the realm of the Drude model, but it is required to fit our data for Ni. This term is not needed for noble metals such as silver or gold [46, 47, 49]. It is clearly unphysical, because the imaginary part of the DC conductivity diverges. This pole does not affect the real part of $\sigma$.

At zero photon energy ($E$=0), $\sigma$ becomes equal to the DC conductivity. From our fits (and ignoring the pole in the last term, which only affects the imaginary part of the DC conductivity), we calculate

$$\sigma_0=\sigma\left(E=0\right)=\frac{\epsilon_0}{\hbar}\frac{E_P^2}{\Gamma_d}\approx 7800\left(\Omega\mathrm{cm}\right)^{-1}, \tag{42}$$

which is about 20 times lower than the bulk conductivity of pure nickel at room temperature, $\sigma_0$=1.43×10$^5$ $(\Omega\mathrm{cm})^{-1}$, see Ref. [9]. Therefore, our NIR/VIS ellipsometry technique is not representative to determine the conductivity of transition metals, as should be expected because of the contribution of d-intraband transitions to the optical absorption [52, 55]. The values calculcated from Eq. (42) increase with Pt concentration, see Table 4, whereas the electrical DC conductivity of $Ni_{1-x}Pt_x$ alloys drops from 1.43×10$^5$ $(\Omega\mathrm{cm})^{-1}$ for $x$=0 to 0.3×10$^5$ $(\Omega\mathrm{cm})^{-1}$ for $x$=0.3 as shown in Ref. [50]. The slow dependence of $\sigma_0$ with Pt variation is another argument that our optical conductivity is determined by optical transitions and not dominated by the Drude term (DC conductivity). For comparison, a factor of 5 of the electrical to the optical (extrapolated) DC conductivity $\sigma_0$ was found for copper by Johnson and Christy [45]. For Ni, this discrepancy is expected to be larger, because the nickel d-intraband transitions are dominant throughout

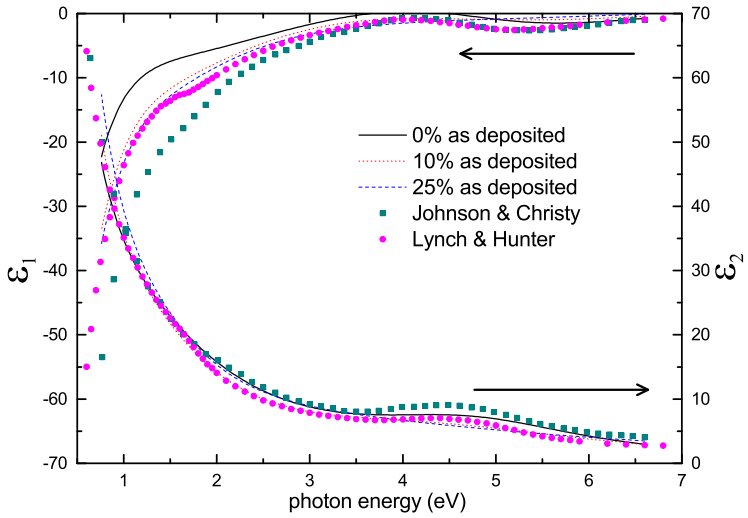


Figure 22: Lines: Real and imaginary parts of the dielectric functions versus photon energy for as-deposited 10 nm thick $Ni_xPt_{1-x}$ alloy films on thermal oxide, calculated from the ellipsometric angles using Drude-Lorentz oscillator fits for $x$=0 (solid), 0.1 (dotted), and 0.25 (dashed). Symbols: Literature data from Refs. [32] (Lynch & Hunter) and [36] (Johnson & Christy). Our tabulated data are available as supplemental materials.

our spectral range and free-electron effects are negligible [45]. This statement needs to be reconsidered at lower photon energies using infrared ellipsometry.

### 4.6 Experimental Results and Discussion

We acquired the ellipsometric angles $\psi$ and $\Delta$ for our 10 nm thick $Ni_{1-x}Pt_x$ alloy samples for $x$=0, 0.1, 0.15, 0.2, and 0.25 as shown in Fig. 20. We first determined the film thicknesses and the optical constants using a basis spline fit. We then fitted the same experimental data with the Drude-Lorentz model as in Eq. (38) and verified that both techniques yielded the same thicknesses and optical conductivities (except for artifacts in both methods). We also determined that the metal thickness was unique. (A good fit could not be achieved when changing the thickness by more than 5 Å. Since refractice index and thickness are correlated, this limits the absolute accuracy of our optical constants to about 5%.)

The resulting dielectric functions for as-deposited $Ni_{1-x}Pt_x$ alloys determined from our films are shown in Fig. 22 for $x$=0, 0.1, and 0.25. Our values of $\epsilon_2$ for pure Ni are in excellent agreement with those tabulated by Lynch and Hunter [32]. Because of the strong divergence of $\epsilon_2$ at low energies, the structure at 1.5 eV is not visible in the $\epsilon_2$ data. On the other hand, there clearly is a peak at 4.5 eV in $\epsilon_2$, which broadens with Pt addition. (The position of this peak is influenced by surface conditions.) Johnson and Christy[36] found slightly higher values of $\epsilon_2$ in the UV than our work.

Large differences between our data and those in Refs. [32] and [36] exist for $\epsilon_1$ in the visible and infrared spectral ranges. We note that the dielectric functions in Ref. [52] and [36] were determined by reflectance followed by Kramers-Kronig transformation. We expect that our ellipsometry results are more accurate. Our data diverge much less rapidly at low photon energies. In addition to the valley at 5 eV (compare the peak in the $\epsilon_2$ spectra already noted) all $\epsilon_1$ data sets for pure Ni show a structure near 1.7 eV. This structure is more pronounced in the low-temperature calorimetric data of Ref. [32] than in the room-temperature data of Johnson and Christy [36]. These structures disappear as Pt is added. At the same near-IR photon energy (say, 1 eV), $\epsilon_1$ is smaller for $Ni_{1-x}Pt_x$ alloys than for pure Ni, while $\epsilon_2$ is about the same. This can be explained with different IR pole contributions for different $x$, which corresponds to a difference in d-interband transitions below our spectral range (non-Drude IR absorption). We will show in the next section that Pt addition has a very significant impact on the d-states of Ni-Pt alloys.

In Fig. 23, we show the same data as in Fig. 22, but displayed as the complex optical conductivity. This representation shows the variations between different data sets more clearly. For example, the gradual increase in the broadening of the

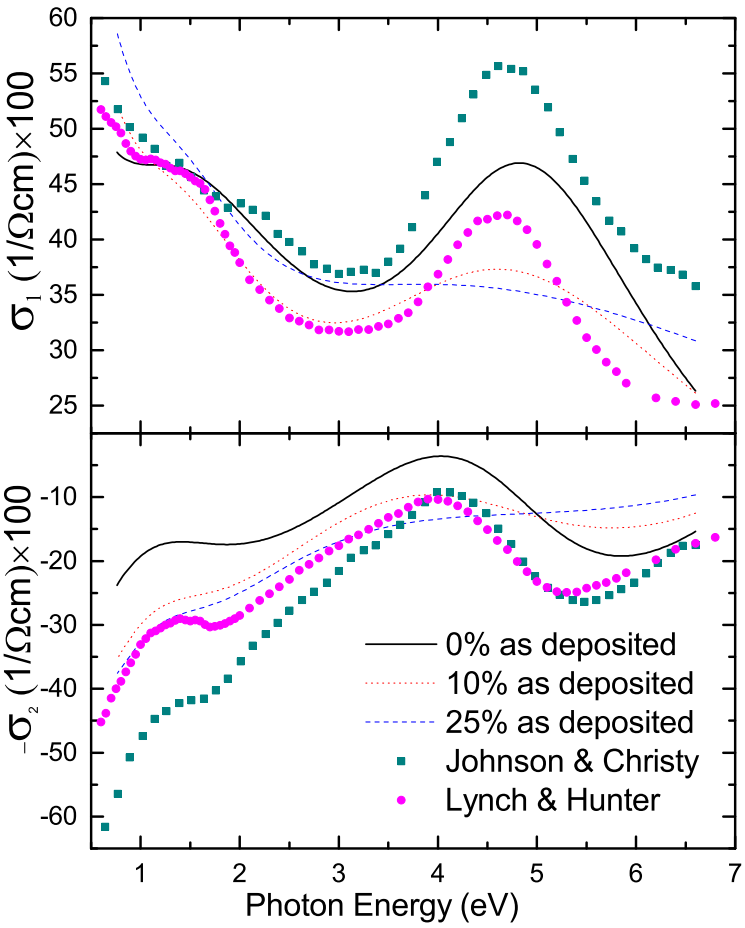


Figure 23: Same data as in Fig. 22, but displayed as optical conductivity, see Eq. (40). Symbols show literature data from Refs. [32] (Lynch & Hunter) and [36] (Johnson & Christy).

UV absorption peak at 4.5 eV with increasing Pt content is very apparent. The conductivity peak at 1.5 eV is strongest in the low-temperature data from Ref. [55]. The peak at 4.5 eV is strongest in the data from Johnson and Christy[36] despite their room-temperature measurements. The strength of the $\sigma_1$ peak at 4.5 eV and the $-\sigma_2$ valley at 5.0 eV are influenced equally by surface roughness (which can be shown by simulations). Since the differences between previous datasets (Refs. [36] and [52]) are more pronounced in $\sigma_1$ than in $\sigma_2$, we rule out surface roughness as the source of the discrepancy. The same statement is true for a native oxide with optical constants similar to bulk NiO [59]. On the other hand, a transparent surface overlayer with a small refractive index (similar to $SiO_2$ or water[61, 60]) affects mostly $\sigma_1$ and has a minimal impact on $\sigma_2$. Therefore, we attribute the differences in the different data sets to surface overlayers or details in the Kramers-Kronig transform.

In Fig. 24, we summarize the optical conductivity for all four $Ni_xPt_{1-x}$ alloys. $\sigma_1$ clearly has two peaks at 1.6 and 5.0 eV. The UV peak broadens with increasing Pt content (see Table 4), but its energy remains about the same. $-\sigma_2$ has Kramers-Kronig consistent peaks at similar energies. The origin of these peaks will be discussed in the next section.

Dotted lines show data for the as-deposited films, while solid lines show data for pieces of the same films that were annealed at 500°C for 30 s. The optical conductivity increases after annealing, as expected. Annealing of metals increases grain size and improves crystallinity and therefore is expected to increase the amplitude of interband transitions, which are the origin of the peaks in $\sigma_1$. Annealing sometimes also increases surface roughness (due to grain growth), which would decrease the peak height in $\sigma_1$, but this was not observed here.

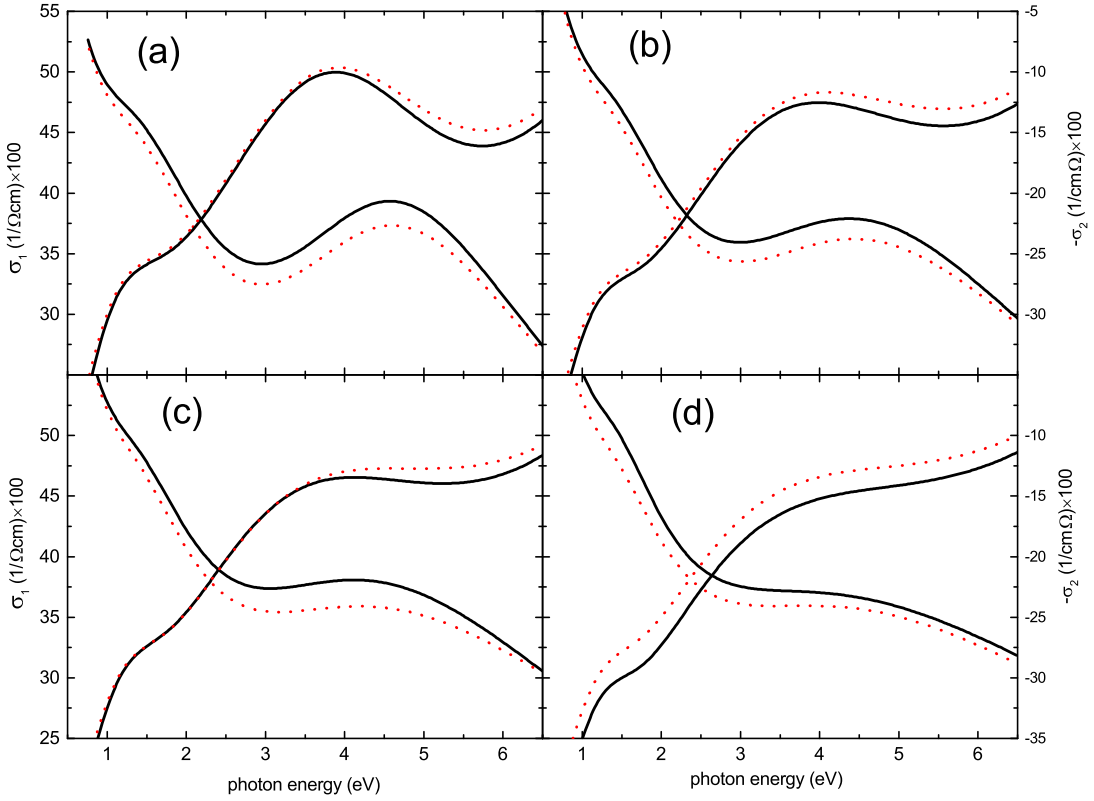


Figure 24: Complex optical conductivity for 10 nm thick $Ni_xPt_{1-x}$ alloy films as deposited (dotted) and after annealing at 500°C for 30s (solid), with Pt concentrations of (a) 10%, (b) 15%, (c) 20%, and (d) 25%.

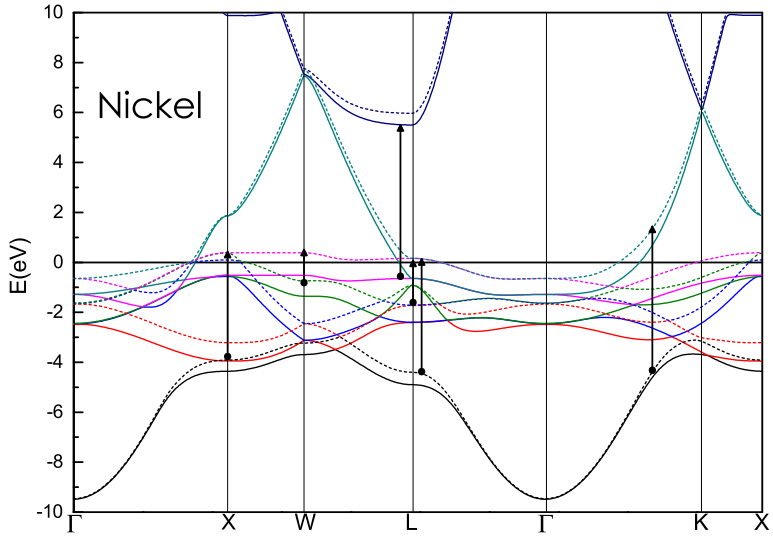


Figure 25: Band structure of crystalline Ni along some symmetry lines in the Brillouin zone, relative to the Fermi level at $E$=0. The solid and dashed lines indicate minority and majority spin states, respectively.

### 4.7 Electronic structure and Comparison with Experiment

To understand the position and broadening of the optical conductivity peaks in NiPt alloys, we performed band structure and density of states calculations for Ni, Pt and $Ni_3Pt$ compound. The computational part of our work was performed in the framework of density functional theory (DFT) using an ab initio pseudopotential technique [65, 66]. We implemented the Kleinman-Bylander form [67] of normconserving nonlocal relativistic Troullier-Martins pseudopotentials [68]. The exchange-correlation energy was evaluated using the generalized gradient approximation (GGA) parameterized by Perdew, Burke, and Ernzerhof [69]. Spin polarization was explicitly specified in our computational approach.

The periodic boundary condition calculations were carried out using the electronic structure code SIESTA (Spanish Initiative for Electronic Simulations with Thousands of Atoms) [70, 71]. The SIESTA code expands electronic wave func-

tions in a basis of Gaussian-type atomic orbitals. The basis set allows arbitrary angular momenta, multiple-zeta, polarized, and off-site orbitals. The Hartree and exchange-correlation potentials are obtained by projecting the electronic density and wave functions onto a real-space grid. All our calculations were conducted using the double-zeta plus polarization (DZP) basis set [72]. The energy cut-off was set to 100 Ry. The Brillouin zone was sampled over 4851 critical k-points. Pure Ni and Pt crystals were modeled using primitive rhombohedral cells containing 1 atom each. $Ni_3Pt$ crystals were modeled using conventional FCC unit cells containing 1 Pt atom and 3 Ni atoms. Structural optimization of crystals was performed using the conjugate gradient algorithm. The optimization was carried out until all residual interatomic forces were smaller than 0.03 eV/A. The optimized crystal structures where then used to calculate the band structure and density of states (DOS) for the Ni, Pt, and $Ni_3Pt$ crystals. The band lines where calculated at the high symmetry points $\Gamma$-$X$-$W$-$L$-$\Gamma$-$K$-$X$ using a grid of 46575 k-points. The DOS was calculated using 46575 k-points over the range from -10.0 eV to 10.0 eV around the Fermi energy.

Figure 25 shows our band structure of pure crystalline Nickel along the lines of high-symmetry. Our results are qualitatively similar to those obtained previously [73, 74]. The plot displays both majority and minority spin states (dashed and solid, respectively). The dispersion of the s-electrons reaches near free-electron behavior at the $K$ and $W$ symmetry points with energy of more than 6 eV above the Fermi level (at zero) and minimal spin-splitting. The lowest s-state shown is approximately 9.5 eV below the Fermi level at the $\Gamma$ point. The d-bands are confined to a range of slightly more than 4 eV with all minority states below the Fermi Level, and the highest majority state about 0.5 eV above the Fermi level along $XW$ and $KX$. The d-electrons in Ni are split by the cubic crystal

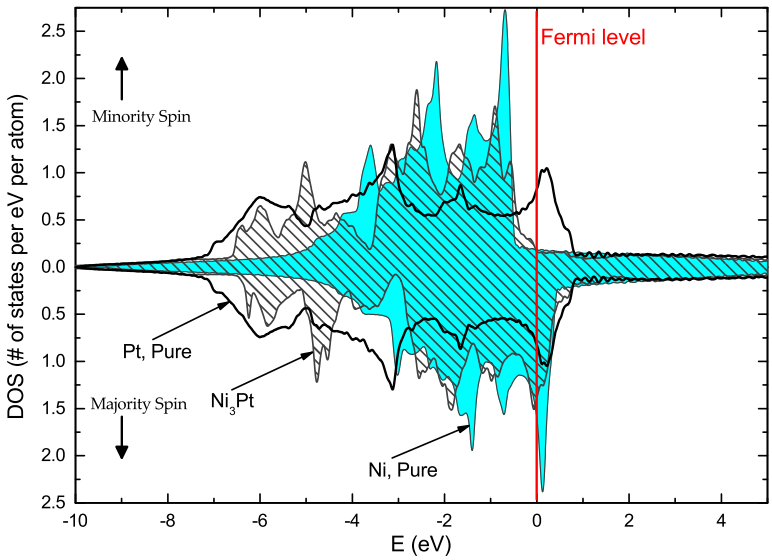


Figure 26: Total density of states for Ni (shaded), Pt (lines), and $Ni_3Pt$ (hatched).

field into a threefold degenerate state with $\Gamma_{25}$ symmetry and, at slightly higher energy, a two-fold degenerate state with $\Gamma_{12}$ symmetry. Our calculations find a spin splitting of the d-bands of about 1 eV, which is larger than the experimental value[64] of 0.23 eV near the crossing of the Fermi level along $\Gamma K$. In Ni, the d bands are more hybridized than in Fe. All Ni d-bands show significant dispersion indicating itinerant character [75].

The real and imaginary parts of the dielectric constant for Ni were measured previously [22, 36, 63]. Two peaks were found at energies similar to ours. Johnson and Christy state that the peak at 5.3 eV (5 eV in this work) is due to transitions from the lowest d bands to the free-electron like bands. They attribute the peak at 1.8 eV (1.6 eV in this work) to transitions within 3d bands. Our band structure shows some of the possible transitions in nickel. It is possible that transitions from the highest minority d- band along $WL$ to an excited state about 5 eV above the Fermi level contribute to the 5eV peak observed in our experiment. Another potential contribution to the 5 eV experimental peak arises from the flat bands

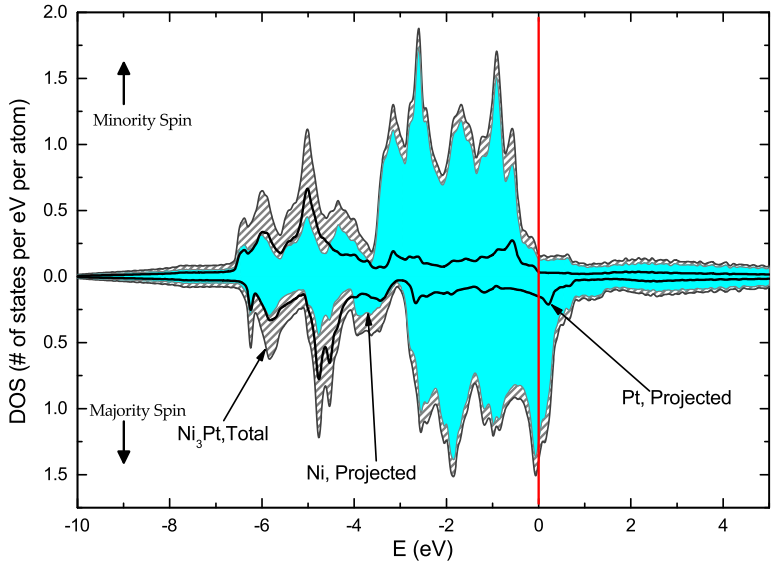


Figure 27: Total Density of states for $Ni_3Pt$ (hatched) and projected density of states for Pt (lines), and Ni (shaded).

of majority carriers near $X$, $W$, $K$ and $L$ (about 4 to 6 eV below the Fermi level) to the d- states just above the Fermi level. The origin of the 1.6 eV experimental peak is clearly d- intraband transitions of majority carriers near the Fermi edge. Possible regions in the Brillouin zone contributing to this peak are located near $X$, $W$, $L$ and $K$. Some of these transitions are indicated by arrows drawn in our band structure.

A glance at the DOS plot for pure nickel and platinum (Fig. 26) will immediately make apparent the significantly broader distribution of states for Pt (lines) in comparison with Ni (shaded). Specifically, the Pt distribution of states extends from 0.6 eV to $-7$ eV (approximately) whereas most Ni states are confined to the 0.3 eV to $-4$ eV range.

By comparison, the projected DOS (that is the density of states per contributing element) shown in Fig. 27 clearly shows the marked effect the lower energy states of Pt have on $Ni_3Pt$. Whereas the Pt contribution to $Ni_3Pt$ density of states

in the $-4$ to 1 eV energy range is minimal, it not only contributes to the alloy density of states in the $-4$ to 7 eV directly, but also enhances, alters, and modifies the Ni contribution to the DOS. Our results of the density of states agree with those calculated previously [76, 77].

Wang and Zunger[76] explained the bonding in transition metals as well as coupling between 3d and 5d transition metals; it was shown that the 3d-5d bands bonding plays a significant role in NiPt alloys. This d-d interaction in the NiPt alloys is responsible for the broadening we see in the optical conductivity (see Fig. 24). This broadening can be explained in terms of the broadening in the Ni 3d bands offering more states and hence more transitions, keeping the peak magnitude of the Ni optical conductivity unchanged.

### 4.8 Conclusions

Our optical constants for Ni-Pt alloys determined using spectroscopic ellipsometry (available as supplemental materials[78]) will have important applications for inline metrology in the semiconductor industry, where Ni is used to contact electronic devices. There are significant differences between our data and those previously published for Ni, especially in $\epsilon_1$ in the near-IR spectral region. We believe that our data are more accurate, since we considered a thin surface layer and since the use of our ellipsometric technique did not rely on a Kramers-Kroing transform.

While the Drude contribution to the dielectric function of $Ni_{1-x}Pt_x$ alloys does not change significantly with composition, there is a significant broadening of the interband transition at 5 eV with increasing Pt content. Our *ab initio* band structure calculations for Ni, Pt, and the $Ni_3Pt$ compound show that the increased broadening is due to the mixing of the 3d states of Ni with the 5d states of Pt.

## 4.9 Acknowledgments

We are grateful to V.W. Kamineni and A.C. Diebold for offline discussions about Ref. [22] and helpful suggestions. We also thank Peter de Chatel for a careful reading of our manuscript and useful comments. Harland G. Tompkins, James Hilfiker, and Thomas E. Tiwald contributed valuable suggestions on data analysis and modeling. Laura G. Piñeda performed simulations to show the impact of surface roughness on the optical conductivity. This work was supported by the National Science Foundation (DMR-1104934). This work has been partially supported by the independent Bulk CMOS and SOI technology development projects at the IBM Microelectronics Division Semiconductor Research & Development Center, Hopewell Junction, NY 12533.

# 5 Optical Conductivity of $Ni_{1-x}Pt_xSi$ Monosilicides ($0<x<0.3$) from Spectroscopic Ellipsometry

This chapter has been submitted for publication as a regular article in the Journal of Vacuum Science and Technology B and is currently under review.

Lina S. Abdallah, Stefan Zollner
Department of Physics, New Mexico State University, MSC 3D, P.O. Box 30001, Las Cruces, NM 88003-8001, USA

Christian Lavoie
IBM Research Division, T.J. Watson Research Center, P.O. Box 218, Yorktown Heights, NY 10598

Ahmet Ozcan
IBM Systems and Technology Group, Hopewell Junction, NY 12533

Mark Raymond
GLOBALFOUNDRIES, 255 Fuller Rd., Albany, NY 12203

## 5.1 Abstract

The optical constants of 22 nm thick $Ni_{1-x}Pt_xSi$ ($0<x<0.3$) monosilicide films were measured using spectroscopic ellipsometry, in the spectral range from 0.6 to 6.6 eV at room temperature. $Ni_{1-x}Pt_x$ films sputtered on clean Si were annealed at 500°C for 30 s to form nickel platinum monosilicides. The correct silicide thickness was found by minimizing Si substrate artifacts in the optical constants of $Ni_{1-x}Pt_xSi$ determined from ellipsometric data analysis. Two interband transitions at 1.8 and 4.5 eV were observed (rather than three peaks in PtSi). The absorption peak at 4.5 eV broadens with increasing Pt content in the monosilicide.

## 5.2 Introduction

Due to their low resistivity (15 $\mu\Omega$cm), nickel silicides are used in microelectronic devices as Ohmic metal-semiconductor contacts with superior chemical and

physical and good thermal stability. Nickel monosilicides have low formation temperature and low Si consumption that result in creating shallow NiSi contacts [17]. However, NiSi is unstable at high temperatures and subject to both agglomeration and formation of $NiSi_2$ [21, 23, 27, 28, 79]. Both need to be avoided, since they lead to high silicide resistivity. Another reason to avoid the formation of $NiSi_2$ is the fact that it is lattice-matched to Si. The disilicide $NiSi_2$ tends to form inverted pyramid defects into the Si (100) substrates used for complementary metal-oxide-semiconductor (CMOS) transistors [80].

Pt is known to be soluble in NiSi, but less soluble in $NiSi_2$, which prevents the formation of $Ni_{1-x}Pt_xSi_2$ due to the decrease in the entropy of the system [23, 81]. Solutions with complete solubility always result in higher entropy and this is not the case in the $Ni_{1-x}Pt_xSi_2$ formation, which will tend to phase-separate into $NiSi_2$ and PtSi. Therefore, as we increase the Pt content in the $Ni_{1-x}Pt_x$ alloys the $Ni_{1-x}Pt_xSi_2$ nucleation barrier becomes higher. Thin silicide layers are known to exhibit reduced thermal stability, easily forming disilicide pyramids or rough (agglomerated) NiSi/Si interfaces due to high interfacial energy [17]. Adding Pt to the NiSi increases the thermal stability of $Ni_{1-x}Pt_xSi$ by delaying the formation of the disilicide as well as agglomeration [21, 23, 81].

After we investigated the optical constants of $Ni_{1-x}Pt_x$ metal alloys in our previous work [54, 7], we are now able to provide accurate optical constants for $Ni_{1-x}Pt_xSi$ monosilicides as a function of platinum content. In this work, our goal is to develop an inline thickness metrology (using inline ellipsometry tools) and enable thickness measurements of $Ni_{1-x}Pt_xSi$ films used on CMOS product wafers. Our methods can be used for monosilicides formed on bulk Si as well as on silicon-on-insulator (SOI) wafers [82].

We also explain our optical constants using the electronic structure by studying

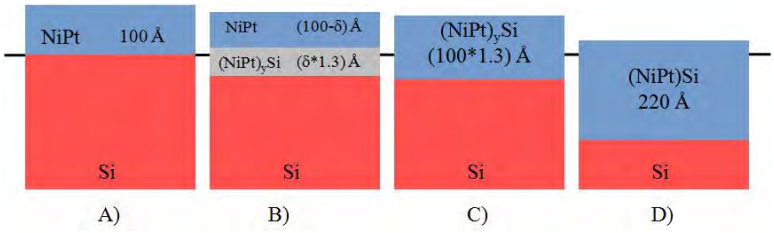


Figure 28: The steps involved in the formation of $Ni_{1-x}Pt_xSi$ monosilicides:[80] A) A 100 Å thick $Ni_{1-x}Pt_x$ alloy is deposited on top of a clean Si surface. B) During deposition, some (but not all) $Ni_{1-x}Pt_x$ diffuses into the Si, creating a buried silicide layer covered by unreacted metal. C) After some annealing, when all the unreacted metal has been consumed, the resulting metal rich silicide has a thickness of 130 Å. D) Annealing the sample at 500°C for 30 s leads to the formation of $Ni_{1-x}Pt_xSi$ monosilicide with a thickness of about 220 Å.

the possible interband transitions in $Ni_{1-x}Pt_xSi$ monosilicides in comparison with *ab initio* theory and measurements on PtSi and NiSi [14].

### 5.3 Samples and Experimental Methods

$Ni_{1-x}Pt_x$ films were deposited on clean 300 mm Si substrates. First, the native $SiO_2$ oxide on Si was removed using wet HF etching. The wafer was then transferred immediately to a physical vapor deposition (PVD) tool where $Ni_{1-x}Pt_x$ films with 100 Å thickness were deposited by co-sputtering from $Ni_{0.9}Pt_{0.1}$ and $Ni_{0.7}Pt_{0.3}$ targets. The samples were annealed at 500°C for 30 s. This temperature is sufficient to form a monosilicide without causing agglomeration of the thin film or disilicide formation. Figure 28 displays the steps involved in the monosilicide formation showing the different phases formed at each step [80, 83]. The monosilicide thickness is usually just above twice the thickness of the unreacted metal (i.e., 220 Å in our case). Composition and thickness of our unreacted metal alloys were confirmed using sheet resistance, X-ray fluorescence, and X-ray reflectivity measurements [22]. We also determined the unreacted metal thickness by spectroscopic ellipsometry of similar films deposited on $SiO_2$ [7, 54].

Spectroscopic ellipsometry measures two ellipsometric angles $\psi$ and $\Delta$ that represent the amplitude ratio and phase difference between p- and s-polarization states, before and after the light gets reflected off the sample. $\psi$ and $\Delta$ are related to the Fresnel reflection coefficients $r_p$ and $r_s$ for the p- and s-polarization through[4, 5]

$$\rho = r_p/r_s = (\tan\psi)\, e^{i\Delta} = (E_{rp}/E_{ip}) \,/\, (E_{rs}/E_{is}) \tag{43}$$

where $\mathrm{E}_{rp}$ ($\mathrm{E}_{ip}$) and $\mathrm{E}_{rs}$ ($\mathrm{E}_{is}$) are the electric field components of the reflected (incident) light in the p and s-direction, respectively.

We acquired the ellipsometric angles $\psi$ and $\Delta$ using a variable angle of incidence rotating analyzer ellipsometer with a computer-controlled Berek wave plate compensator [84]. The angle of incidence was varied from 65° to 75°. Measurements were performed over a broad photon energy range from 0.6 eV to 6.6 eV. The back sides of our samples were roughened to avoid backside reflection, which would result in depolarization of the reflected beam. In our experiments, the depolarization is typically below 0.5% except at the ends of our spectral range, where the noise increases.

### 5.4 Data Analysis and Results

Our experimental data for $\mathrm{Ni_{0.9}Pt_{0.1}Si}$ monosilicide, displayed as a pseudodielectric function, are shown in Fig. 29. In this data representation, one assumes (incorrectly) that the sample is a bulk substrate, which allows the conversion of the ellipsometric angles into the pseudo-dielectric function using Fresnel's equations [4, 5]. For a layered sample, the pseudodielectric function combines the electronic structure of all materials and also considers interference effects. Therefore, the Si substrate $E_1$ critical point appears in the pseudodielectric function at 3.4 eV as

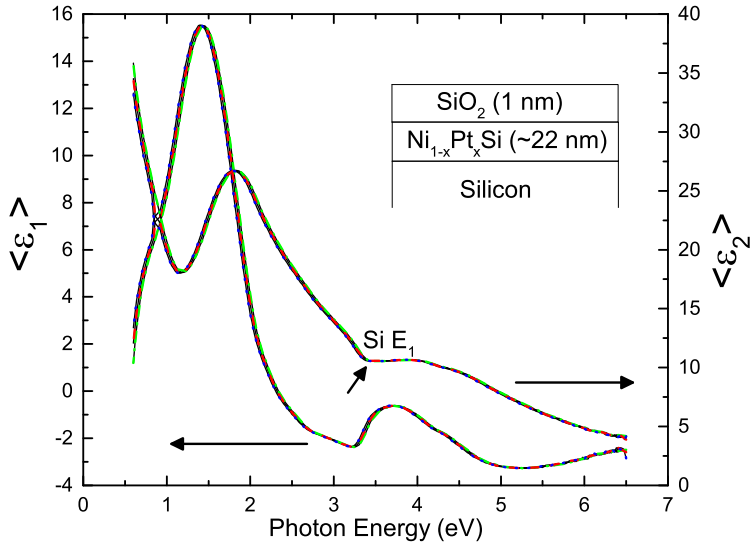


Figure 29: Pseudodielectric function for a 220 Å thick $Ni_{0.9}Pt_{0.1}Si$ monosilicide sample measured at three angles of incidence (65°, 70°, 75°). The kink seen in the pseudodielectric function at 3.4 eV arises from the Si $E_1$ critical point. The graph shows both experimental data and results of a point-by-point fit at all three angles. All data sets are in excellent agreement. The inset shows the sample structure assumed for the point-by-point fit.

shown by the arrow.

In order to determine accurate optical constants of our $Ni_{1-x}Pt_xSi$ monosilicides, we assume a layered sample structure as shown in the inset of Fig. 29, where the optical constants for the silicon substrate and for $SiO_2$ are well known. Previous studies found that monosilicides are covered with a thin $SiO_2$ native oxide [22, 85, 86]. We added a 10 Å $SiO_2$ layer in our model to account for this, see Fig. 29.

If the silicide layer thickness is assumed to be known, we can find the optical constants for the layer by solving the Fresnel equations numerically [4, 5]. This is known as a point-by-point fit. The critical points of the substrate appear as artifacts in the optical constants of the layer if an incorrect thickness is used for the monosilicide layer [33, 87]. Miniziming these artifacts allows us to determine

the correct silicide thickness.

Figure 30 shows an example of this procedure, which we followed to choose the correct thickness for the $Ni_{0.9}Pt_{0.1}Si$ monosilicide. The dip at 3.4 eV represents the $E_1$ critical point for Si [88]. This dip can be minimized by choosing the correct $Ni_{1-x}Pt_xSi$ thickness (230 Å). However, this dip cannot be eliminated completely since the interface between the silicide layer and the Si substrate is not entirely flat and the Pt distribution throughout the silicide is not uniform (based on transmission electron micrographs with elemental mapping). The same procedure for choosing the correct silicide layer thickness was followed for all the films, with results shown in Table 5. As expected [80], the ratio of the monosilicide to unreacted metal thickness is about 2.2. (We stress that it is not necessary to know the resistivity of the silicide to determine its thickness, as was argued in Ref. [82].)

After the $Ni_{1-x}Pt_xSi$ monosilicide thicknesses are determined, another fit is performed using a set of oscillators: a Drude oscillator with two parameters $E_P$ and $\Gamma_d$ (related to the carrier density per unit volume and their scattering time) describes the response of free carriers to the electromagnetic wave. In addition, a sum of Lorentz oscillators describes the interband transitions of bound electrons. Each Lorentz oscillator $j$ has three parameters: oscillator strength $A_j$, interband transition energy $E_j$, and damping constant $\Gamma_j$.

The complex dielectric function $\epsilon = \epsilon_1 + i\epsilon_2$ versus photon energy $E$ for $Ni_{1-x}Pt_xSi$ alloys can thus be written in the following functional form known as the Drude-Lorentz model:[5, 22, 42, 43, 44, 82]

$$\epsilon(E) = 1 - \frac{E_P^2}{E(E + i\Gamma_d)} + \sum_{j=1}^{5} \frac{A_j E_j^2}{E_j^2 - E^2 - i\Gamma_j E} \tag{44}$$

The first term describes the permeability of vacuum, the second term represents the Drude contribution and the third term represents a sum of Lorentz oscillators.

The dielectric function of $Ni_{1-x}Pt_xSi$ monosilicides shows two dominant peaks at 1.9 eV and at 4.4 eV (which we label $\alpha$ and $\gamma$, see Fig. 30). The same peaks were seen in previous studies for NiSi [22, 82, 89] and PtSi [14]. In addition to these two strong Lorentz oscillators, three weaker oscillators are also necessary to achieve a good fit to the ellipsometric angles. Therefore, a total of five Lorentz oscillators and one Drude oscillator were used to expand the optical constants of $Ni_{1-x}Pt_xSi$ monosilicides. Figure 31 shows that both methods, point-by-point fit and Drude-Lorentz oscillator fit, yield the same dielectric function of the silicide (for the same layer thickness).

The real and imaginary parts of the dielectric function for five $Ni_{1-x}Pt_xSi$ monosilicides ($x$=0 to $x$=0.3) are shown in Fig. 32. The two strongest interband transitions are indicated by the Greek letters $\alpha$ and $\gamma$ and will be discussed later. Table 5 lists the Drude parameters obtained from the Drude-Lorentz fit for all samples. Tables of the dielectric functions of these silicides, obtained from a Drude-Lorentz fit in Eq. (44), are available as supplemental materials and on the authors' web site. These dielectric functions are suitable for inline metrology purposes.

Figure 31 shows that the contribution of the Drude term to the dielectric function (intraband free-carrier absorption) becomes small above 2 eV in comparison to the interband absorption (Lorentz oscillators) shown by the solid line. On the other hand, even at the lower end of our spectral range (0.6 eV), there are still significant contributions of interband transitions to the overall dielectric function. Because of our limited spectral range, the two Drude parameters (plasma frequency and broadening) are strongly correlated and therefore the parameters

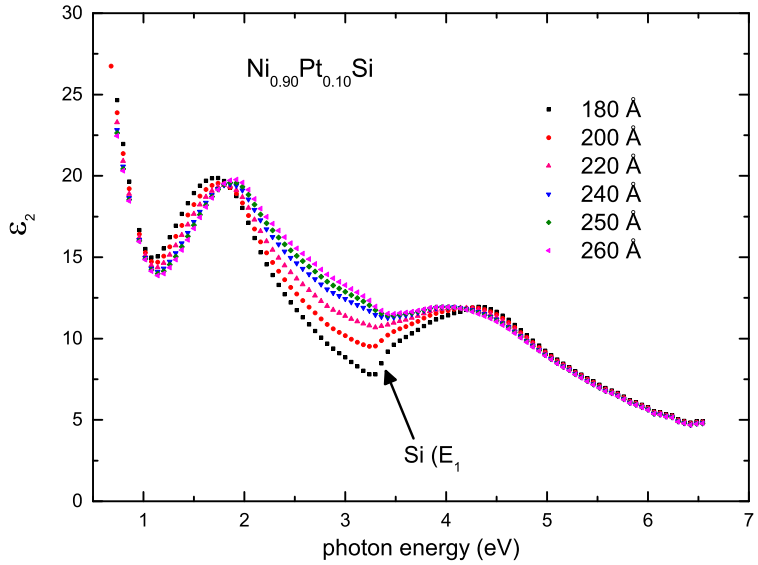


Figure 30: The imaginary part of the dielectric function for $Ni_{0.9}Pt_{0.1}Si$ monosilicide derived from the raw data assuming different monosilicide thicknesses. The graph shows the Si critical point for the different thicknesses. The true monosilicide thickness (230 Å) is the thickness leading to the weakest Si structure.

shown in Table 5 are only examples of suitable parameters, not suggested values with known error limits. There is also a strong correlation between the parameters of the lowest Lorentz oscillator (at 0.8 eV) and the Drude parameters [22]. These correlations might be removed with infrared ellipsometry measurements, which are planned. Because of these parameter correlations, we will not discuss trends of our parameter sets with thickness or Pt content.

### 5.5 Discussion

The band structure and the origin of the bonding in NiSi and PtSi have been investigated by several authors [14, 90, 91, 92, 93]. It was shown that the overlap of Ni 3d (Pt 5d) with Si 3s and 3p bands is responsible for partially covalent bonding in NiSi and PtSi [14, 89]. The valence band of $Ni_{1-x}Pt_xSi$ is comprised of Ni/Pt d-states and Si 3p-states, while the conduction band is dominated by Si 3p-

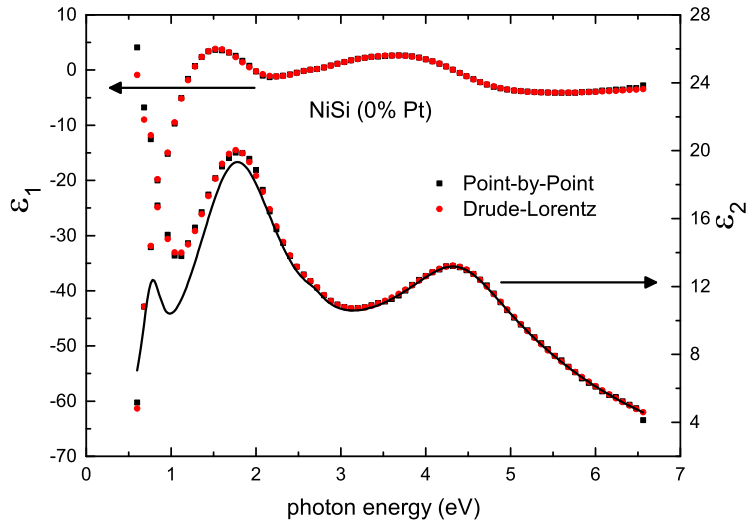


Figure 31: The real and imaginary parts of the dielectric function for NiSi monosilicide using a point by point fit (squares) in comparison with a Drude-Lorentz oscillator fit (circles). Both methods yield the same results for the dielectric function. The solid line shows the contribution of interband transitions (Lorentz oscillators) to the absorption, with free-carrier absorption (Drude term) subtracted.

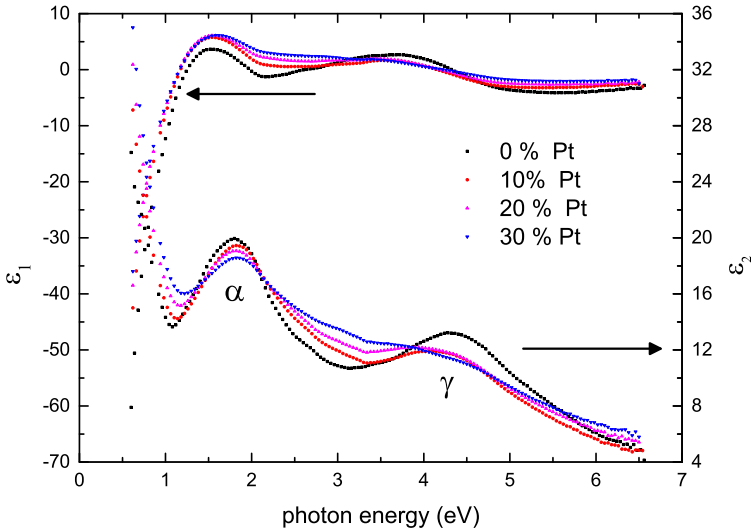


Figure 32: The real and imaginary parts of the dielectric functions for different $Ni_{1-x}Pt_xSi$ monosilicides ($x$=0 to $x$=0.3) determined from a point-by-point fit with thicknesses shown in Table 5. Data obtained from a fit with Eq. (44) are very similar. The two peaks labeled $\alpha$ and $\gamma$ are caused by interband transition in the silicide.

states [92]. We therefore expect two types of interband transitions in $Ni_{1-x}Pt_xSi$ monosilicides: (1) Transitions from Ni (3d) or Pt (5d) ground states to Si (3p) excited states, and (2) transitions from Si (3p) ground states to Si (3p) excited states. As we will show, we identify peak $\alpha$ in Fig. 32 with type (2) and peak $\gamma$ with type (1). Some mixing of the orbitals is possible, of course, due to the covalent bonding between Ni-Pt and Si [14].

Previous optical studies measured the real and the imaginary parts of the dielectric function for NiSi using spectroscopic ellipsometry[22, 94, 82] and reflectance followed by Kramers-Kronig transform [89]. These results showed two peaks in the imaginary part at 1.9 eV and 4.4 eV [82]. The same two peaks were observed in the imaginary part of the dielectric function for PtSi [14] as well as another peak at 3 eV (not observed in our results for $Ni_{1-x}Pt_xSi$). Spectroscopic ellipsometry has also been used to study the formation of NiSi [94], NiGe[95], and PtSi[96] by annealing of thin metal films sputtered on Si.

Only the nickel monosilicide NiSi shows the two characteristic peaks at 1.9 and 4.4 eV. Metal-rich silicides (such as $Ni_3Si$ or $Ni_2Si$) and the disilicide $NiSi_2$ have peaks with different shapes and peak energies [89, 94, 97, 98]. In general, the amplitude of interband transitions increases with decreasing metal-silicon ratio [94]. Also, peak $\alpha$ shifts towards the UV as the metal-silicon ratio is decreased [89]. Therefore, ellipsometry spectra are suitable to identify the silicide phase that has formed on the wafer.

The dielectric function of conductors (metals, silicides, doped semiconductors, etc) diverges at low photon energies because of the Drude contribution in Eq. (44). In a perfect conductor, the absorption is infinite and a static electric field cannot exist. This divergence (see Fig. 32) dominates the dielectric function. It is convenient to remove this divergence by multiplying the optical constants with the

photon energy and defining the complex optical conductivity by the equation[63]

$$\sigma(E) = -i\frac{\epsilon_0}{\hbar}\left[\epsilon(E) - 1\right]E, \tag{45}$$

where $\epsilon_0$ is the permittivity of vacuum and $\hbar$ is Planck's constant. For our monosilicide films, the optical conductivity as a function of photon energy is shown in Fig. 33.

The imaginary part of $\epsilon$ is related to absorption (energy dissipated in the system), while its real part is related to the speed of light (energy stored in the system). Similarly, $\sigma_1$ is related to interband optical absorption and the attenuation of an AC signal, while $\sigma_2$ is related to dispersion and the phase shift of an AC signal in a system (circuit or material).

The DC conductivity is calculated at zero photon energy (E=0). Using the Drude parameters we obtained from our fits (summarized in Table 5), we calculate

$$\sigma_0 = \sigma(E = 0) = \frac{\epsilon_0}{\hbar}\frac{E_P^2}{\Gamma_d}, \tag{46}$$

Table 5 also shows the zero-frequency conductivity calculated from the oscillator fit. These values of optical conductivity are compared with the electrical conductivity $\sigma_{\text{exp}}$ calculated from the sheet resistance $r_s$ measured for our films. This is the ratio $r_s = \rho/t$, where $\rho = \sigma_{\text{exp}}^{-1}$ is the electrical resistivity and t is the thickness of the silicide [99].

For our monosilicide films, the plasma energy varies between 5.6 eV for NiSi ($x$=0) and 5.0 eV for $Ni_{0.7}Pt_{0.3}Si$, see Table 5. Therefore, the free carrier density, which is related to the plasma frequency $\omega_P = E_P/\hbar$, varies only slightly with Pt content. In our earlier work [54] on unreacted $Ni_{1-x}Pt_x$, we found plasma energies between 7 and 8 eV, slightly higher than for monosilicides.

While the plasma energy does not show significant variations, the Drude broad-

ening approximately triples as $x$ is increased from 0 to 0.3. Similarly, we find that the extrapolated DC conductivity $\sigma_0$ also decreases by about a factor of 3. We conclude that the reduction in $\sigma_0$ with increasing Pt content is due to increased scattering of carriers, not due to a change in carrier concentration (or effective mass of the carriers). A threefold increase in $Ni_{1-x}Pt_xSi$ resistivity was also observed in Ref. [100] as the Pt content was increased from 0 to 0.5. This was confirmed by our own sheet resistance measurements shown in Fig. 34. It was argued [100] that the reduction in conductivity with increasing Pt content was due to increased grain boundary scattering (reduced grain size for larger Pt content). That statement is consistent with our increase in the Drude broadening parameter.

As a word of caution, we need to stress that our Drude parameters were obtained by fitting the dielectric function from 0.7 to 1.0 eV and then extrapolating to $E$=0. That is not very reliable. As a matter of fact, our DC conductivities determined from ellipsometry are consistently lower than the conductivities determined from electrical sheet resistance measurements (up to a factor of 2 for monosilicides, or a factor of 20 for pure unreacted Ni). In future work, we will investigate if the agreement between optical and electrical conductivity measurements can be improved with infrared ellipsometry.

Figure 33 shows the complex optical conductivity as a function of photon energy for the different monosilicides in comparison with that of a $Ni_{0.9}Pt_{0.1}$ film deposited on $SiO_2$. The real part of the optical conductivity in the IR region shows that the DC conductivity for the unreacted metal is higher than for silicides. The conductivity in this part of the spectrum is dominated by the Drude response of the free electrons in the sample. The unreacted metal shows more metallic behavior in the IR region than the monosilicide [89].

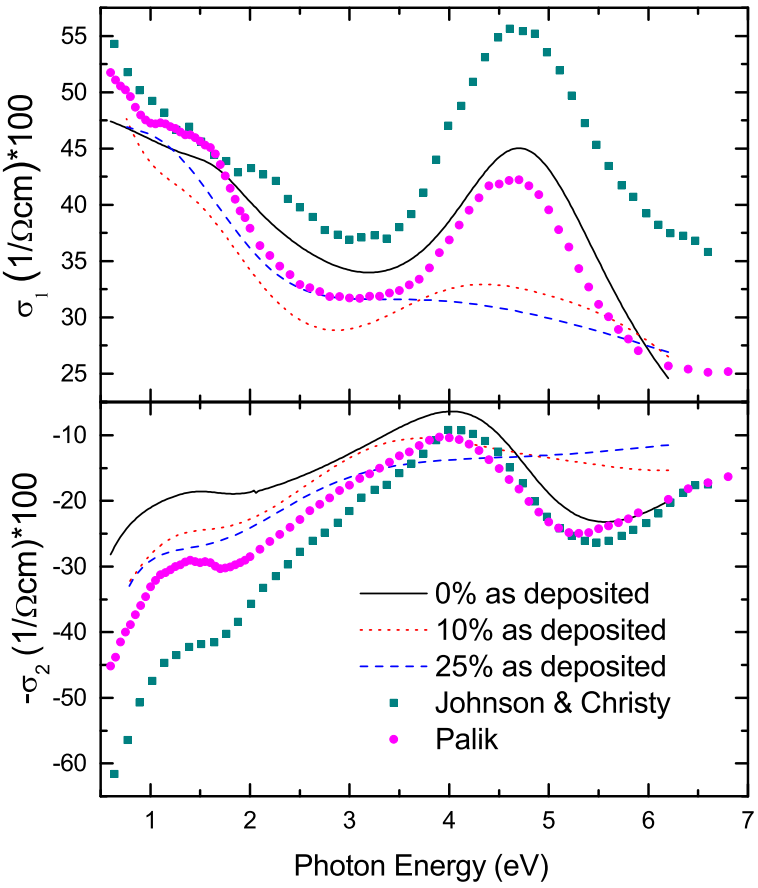


Figure 33: The real and the imaginary parts of the optical conductivity for $Ni_{1-x}Pt_xSi$ monosilicides (x=0, 0.1, 0.2, 0.3) (symbol) in comparison with 100 Å pure $Ni_{0.9}Pt_{0.1}$ metal alloy (lines).

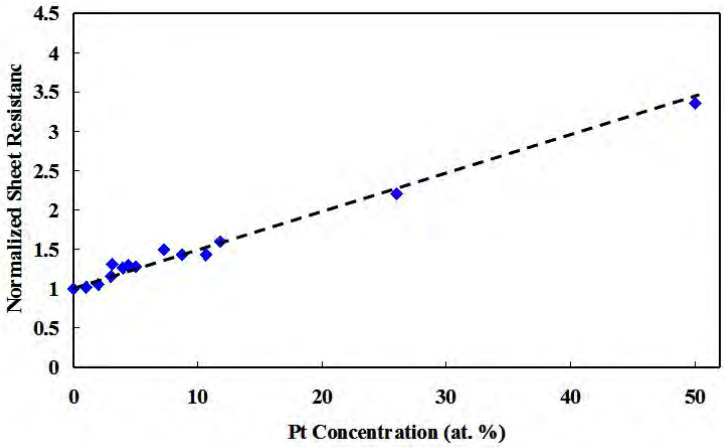


Figure 34: Sheet resistance of 100 Å thick $Ni_{1-x}Pt_xSi$ monosilicides determined using four-point-probe measurements.

Table 5: Thickness $t$ of different $Ni_{1-x}Pt_xSi$ monosilicide films obtained by minimizing substrate artifacts, see Fig. 30. $\sigma_0$ is the zero-energy optical conductivity calculated from Eq. (46) and $\sigma_{\rm exp}$ is the DC electrical conductivity determined from sheet resistance measurements (in units of $1/\Omega$cm). For comparison, results for a pure Ni film on $SiO_2$ from Ref. [7] are also given. As expected [80], the ratio of the monosilicide to unreacted metal thickness is about 2.2. Drude parameters for NiSi from a mid-infrared reflectance experiment [89] are also given.

| $x$ | $E_P$ (eV) | $\Gamma_d$ (eV) | $\sigma_0$ | $t$ (Å) | $\sigma_{\rm exp}$ |
|---|---|---|---|---|---|
| 0 | 5.57 | 0.12 | 34773 | 240 | 65104 |
| 0.10 | 5.31 | 0.19 | 19959 | 230 | 30193 |
| 0.20 | 5.2 | 0.24 | 15153 | 220 | 25680 |
| 0.30 | 5.0 | 0.31 | 10847 | 200 | 14684 |
| Ni | 6.8 | 0.8 | 7799 | 101 | 143000 |
| NiSi[a] | 3.8 | 0.035 | 54000 | 1900 | 83000 |

[a] Ref. [89].

For the visible and UV parts of the spectrum, the optical conductivity for the monosilicide is higher than that of the metal films due to the enhanced interband transitions driven by the silicon in the monosilicide [89]. The 4.5 eV absorption peak clearly broadens with increasing platinum content in the monosilicide. Similar broadening with increasing $x$ was found in our earlier work on unreacted $Ni_{1-x}Pt_x$ alloys [54]. It was shown that the absorption peak broadens with increasing Pt content in the alloy due to the enhanced density of states that Pt causes when added to Ni. The larger the Pt concentration in the alloy, the broader the peak. The same argument can be applied in the monosilicide optical conductivity. We claim that the peak at 4.5 eV is due to interband transitiona from the overlapped Ni(3d)-Pt(5d) valence bands to the Si 3p conduction bands. The broadening of the peak is therefore related to the broadening of the initial states in the valence band.

On the other hand, the peak at 1.8 eV does not seem to depend on Pt content. This means that the transition at this photon energy is caused mainly by Si electronic states. The Pt content therefore does not affect the interband transition.

## 5.6 Conclusions

We performed ellipsometry measurements from 0.6 to 6.6 eV on $Ni_{1-x}Pt_xSi$ monosilicide films ($0<x<0.3$) with 220 Å thickness on Si substrates. Through careful analysis of the data with two different methods (point-by-point fit with variable thickness to reduce substrate artifacts and Drude-Lorentz oscillator fitting), we were able to determine the optical constants of $Ni_{1-x}Pt_xSi$ monosilicides ($0<x<0.3$) with high accuracy. At low photon energies, $\epsilon$ diverges due to the Drude response of free carriers. The Drude broadening increases with increasing Pt content. In the visible and UV region of the spectra, we find peaks at 1.8 and

4.5 eV due to interband optical transitions. While the peak at 1.8 eV does not change much with Pt content, there is a significant broadening of the peak at 4.5 eV, presumably due to mixing of the Ni 3d- and Pt 5d-related valence band states in the silicide.

## 5.7 Acknowledgments

This work was supported by the National Science Foundation (DMR-1104934). This work has been partially supported by the independent Bulk CMOS and SOI technology development projects at the IBM Microelectronics Division Semiconductor Research & Development Center, Hopewell Junction, NY 12533. LSA is grateful to the AVS Thin Film Division for being selected as a finalist for the J.M.E. Harper Graduate Student Award at the 2013 AVS International Symposium.

# 6 Infrared Optical Conductivity of $Ni_{1-x}Pt_x$ Alloys and $Ni_{1-x}Pt_xSi$ Monosilicides from Spectroscopic Ellipsometry

This chapter is currently being prepared for submission as a regular article for publication in the Journal of Vacuum Science and Technology B.

Lina S. Abdallah, Stefan Zollner, Travis Willett-Gies, Eric Delong
Department of Physics, New Mexico State University, MSC 3D, P.O. Box 30001, Las Cruces, NM 88003-8001, USA

Christian Lavoie
IBM Research Division, T.J. Watson Research Center, P.O. Box 218, Yorktown Heights, NY 10598

Ahmet Ozcan
IBM Systems and Technology Group, Hopewell Junction, NY 12533

Mark Raymond
GLOBALFOUNDRIES, 255 Fuller Rd., Albany, NY 12203

Harland Tompkins
J.A. Woollam Co., Lincoln, NE

## 6.1 Abstract

The optical constants of $Ni_{1-x}Pt_x$ metal alloys and $Ni_{1-x}Pt_xSi$ monosilicides in the mid-infrared spectral region were determined as a function of Pt content using Fourier-transform spectroscopic ellipsometry from 250 to 6500 $cm^{-1}$. For pure Ni films on $SiO_2$, we also studied the dependence of the optical constants on Ni thickness from 100 to 1000 Å.

## 6.2 Introduction

The complex dielectric function $\epsilon(\omega)=\epsilon_1(\omega)+i\epsilon_2(\omega)$ of metals and other conductors (e.g., doped semiconductors or conducting metal compounds, such as silicides) has two contributions from free and bound electrons. Free electron absorption is usually described by a Drude term, while bound electron absorption

is given by one or more oscillator-like terms, such as a Lorentz, Gauss, or Tauc-Lorentz oscillator. (For this work, we ignore the contributions to infrared absorption by polar lattice vibrations, which were not observed in our metal alloys or silicides.) The Drude term causes a divergence of the dielectric function at low frequencies, because a static electric field cannot exist in a metal. The complex refractive index $n = N + ik$, where $N$ is the refractive index and $k$ the extinction coefficient, is the (complex) square root of $\epsilon$. It also diverges at low energies.

An equivalent description of the infrared optical constants of metals can be given by the complex optical conductivity defined by [63]

$$\sigma(E) = -i\frac{\epsilon_0}{\hbar}\left[\epsilon(E) - 1\right]E, \tag{47}$$

where $E{=}\hbar\omega$ is the photon energy, $\epsilon_0$ is the permittivity of vacuum, and $\hbar$ is Planck's constant. The real part of the optical conductivity describes the absorption of the material (dissipated energy), whereas the imaginary part is related to dispersion (stored energy). Multiplying the dielectric function by the photon energy cancels the Drude divergence at low frequencies and leads to a finite real conductivity for the metal, as it should be.

However, describing the infrared dielectric function of transition metals and their compounds is complicated, because in such materials the d-band manifold usually crosses the Fermi level, leaving some d-states filled and others unfilled [7, 14]. In transition metals, d-intraband optical transitions (which are different from the plasma oscillations of free carriers near the Fermi level) therefore occur at arbitrarily low energies. The Drude model is not expected to give a good description of the infrared optical constants of transition metals, because the contributions to the absorption by free carriers cannot easily be separated from the intraband absorption of d-electrons. Interband transitions occur at higher

energies (usually in the near-infrared or visible), but conceptually, within the band model of a metal, they are also treated using Lorentz oscillators, within the same framework as d-intraband transitions.

Measurements of the mid-infrared optical constants of metals are rare and for most metals have been confined to infrared reflectance measurements, followed by a Kramers-Kronig transformation to obtain the dielectric function. Most notable are the reflection measurements of noble metals and transition metals by Johnson and Christy. The recent development of Fourier-transform infrared ellipsometry has not yet been applied to transition metals and their silicides.

The purpose of the present article is to follow our earlier near-infrared to quartz-ultraviolet work on the optical constants of Ni, $Ni_{1-x}Pt_x$ alloys, and their monosilicides [7, 54, 101] between 0.5 and 6.5 eV with infrared ellipsometry measurements on the same samples. This will achieve a more comprehensive and yet consistent understanding of the optical constants of transitions metals and their silicides, from the mid-infrared to the quartz-ultraviolet.

### 6.3 Experimental Methods, Data Analysis, and Samples

Infrared ellipsometry measurements were performed using a J.A. Woollam FTIR-VASE variable angle of incidence ellipsometer from 250 $cm^{-1}$ to 6000 $cm^{-1}$ at three angles of incidence: 60°, 65°, and 70°. This instrument is based on a fixed analyzer (at 0° and 180°), a fixed polarizer (at ±45°), and a rotating compensator. To increase accuracy, two fixed positions for the analyzer and polarizer were chosen (four-zone measurements), as this cancels experimental errors to first order in the analyzer and polarizer position. In the spectral range around 6000 $cm^{-1}$, our FTIR ellipsometry results are consistent with our earlier near-IR work [7, 101].

Ellipsometry measurements result in finding two ellipsometric angles $\psi$ and $\Delta$

as a function of photon energy and incidence angle. These ellipsometric angles are related to the Fresnel reflectance ratio $\rho = r_p/r_s = e^{i\Delta} \tan\psi$, where $r_p$ and $r_s$ are the Fresnel reflectance coefficients for p- and s-polarized light, respectively.

To extract the optical constants of a thin metal film, one needs to know the sample structure and all film thicknesses. For our samples, the film thicknesses were determined in our previous (near-IR to UV) work and therefore fixed, see [7, 101] and tables therein. Small thickness errors are possible due to within-wafer variations, but this only affects the absolute accuracy of our optical constants (on the order of 5%), but not the physical interpretation of our results. (Varying thicknesses did not improve the quality of our fits.) The infrared optical constants for Si and $SiO_2$ (used as a buffer layer between Si and metals for some samples, to avoid silicide formation) were taken from the instrument's database and confirmed with control samples (Si with native oxide, Si with thick thermal oxide without metal). We note that the optical constants of thick thermal oxides depend on the growth conditions and the use of control samples without metal is therefore crucial. The root-mean-square surface roughness of our samples (determined by atomic force microscopy) was typically about 1 nm or less, which can be ignored in infrared ellipsometry data analysis, because the thickness of the roughness layer is much smaller than the wavelength.

Given these assumptions, the optical constants (dielectric function, refractive index, optical conductivity) of our metal and metal silicide films can be determined using standard ellipsometry data fitting techniques. In general, one varies the parameters of a model until good agreement between the model and the experimental data is reached. In our work, we use three different techniques: (1) uncorrelated wavelength-by-wavelength (point-by-point) inversion of the Fresnel equations; (2) expansion of the dielectric function using basis splines; (3) expan-

sion of the dielectric function as a sum of Drude and Lorentz oscillators. All three techniques have advantages and disadvantages [54]. We used all three methods and refined them, until all three yielded the same results, within their limitations. The basis spline and point-by-point results usually yield the most accurate and unbiased optical constants, but the oscillator expansion is more suitable for metrology applications (thickness measurements) and to achieve a physical understanding of the optical properties of metals. Details about our oscillator models are given in the next section.

In this work, we are investigating the infrared optical constants for three sets of samples: (1) pure Ni films with different thicknesses ranging from 100 to 1000 Å, deposited on a thick layer of $SiO_2$; (2) unreacted $Ni_{1-x}Pt_x$ alloys deposited on a thick layer of $SiO_2$; and (3) a set of $Ni_{1-x}Pt_xSi$ monosilicides created by annealing of the samples (2). The details of the deposition process of the second and third set of samples is illustrated in Refs. [7, 54] whereas the details of the third set of samples will be discussed later.

## 6.4 Models for Optical Constants of Metals

Within the Drude-Lorentz model mentioned in the introduction (Sec. 6.2), we write the dielectric function versus photon energy $E{=}\hbar\omega$ as

$$\epsilon\left(E\right)=1-\sum_{i}\frac{E_{Pi}^{2}}{E\left(E+i\Gamma_{di}\right)}+\sum_{j}\frac{A_{j}E_{j}^{2}}{E_{j}^{2}-E^{2}-i\Gamma_{j}E}. \tag{48}$$

The constant term ($\epsilon{=}1$) describes the contribution of the vacuum to the optical constants. The first sum (Drude model) considers the optical absorption and dispersion due to several species of free carriers, each with a plasma frequency $E_{Pi}$ and a constant scattering rate $\Gamma_{di}$. (Frequencies and scattering rates carry units of energy, after multiplication by $\hbar$.) These distinct species of free carriers

might be electrons and holes, electrons in different bands (s, p, d, etc), or electrons in different spatial regions of the crystal (for example inside of grains and near grain boundaries). Two Drude sums were sufficient to describe our ellipsometry data for Ni, $Ni_{1-x}Pt_x$ alloys, and related monosilicides within the range of our experiment from 250 to 6000 $cm^{-1}$.

The second sum (Lorentz model) describes the contribution of interband transitions to absorption and dispersion. $A_j$, $E_j$, and $\Gamma_j$ are the amplitude, resonance energy, and broadening of each transition. The number of oscillators required depends on the energy range of the optical measurement. If a resonance energy $E_j$ is far outside the experimental spectral range, it may be sufficient to set the broadening $\Gamma_j$ to zero. (This leads only to a real part contribution. The corresponding imaginary part vanishes. Such a term with $\Gamma_j$=0 is called a pole.) Finally, for very large resonance energies, the contribution to the dielectric function may be constant within the experimental spectral range. Such constant contributions of high-energy transitions can be combined with the vacuum term to yield the high-frequency dielectric constant $\epsilon_\infty$. (In an insulator, the high-frequency dielectric constant is equal to the dielectric constant at a photon energy much larger than that of lattice vibrations and much lower than that of electronic interband or intraband transitions. It represents the electronic contribution to the static zero-frequency dielectric constant. In a transition metal, there is no such energy which meets this condition, since intraband electronic transitions can happen at arbitrarily low frequencies, even below the vibrational frequencies. Therefore, the term $\epsilon_\infty$ in a metal describes the contribution to the dielectric constant by the vacuum and all Lorentz oscillators in the long-wavelength limit, with the Drude contribution due to free carriers subtracted.)

Some researchers describe the infrared dielectric function of metals with a

single Drude term

$$\epsilon(E) = 1 - \frac{E_P^2}{E(E + i\Gamma_d)}. \tag{49}$$

This simple expression can only agree with the more comprehensive Drude-Lorentz expression (48), if the scattering rate $\Gamma_d$ is frequency-dependent. Therefore, some previous studies [102] claim that a frequency dependent relaxation time is nessecary when describing the infrared optical properties of metals with a Drude model. By contrast, we take the viewpoint that several scattering rates $\Gamma_{di}$ and $\Gamma_j$ are needed, with each being constant and independent of photon energy. Both viewpoints lead to the same infrared dielectric function and are not in conflict with each other.

### 6.5 Pure nickel samples

A thickness series of pure nickel was sputtered using a sputter-up tool with a DC power of 135 Watts and a deposition pressure of 3 mTorr. The sputtering time (at 1 Angstrom/sec dep rate) varies for the different nickel thicknesses. The film thicknesses under study are 100, 200, 500, and 1000 Å. The choice of this group of thicknesses has to do with the fact that at 100 Å the film starts to exhibit a metallic behavior and after 1000 Å the film no longer shows a difference in optical properties.

Figures 35 and 36 show the ellipsometric angles $\psi$ and $\Delta$ for the different pure nickel samples. Both figures show a dip at around 1100 $cm^{-1}$ which is related to TO peak in $SiO_2$ that corresponds to bond-stretching vibration [103]. The dip is present in both 100 Å and 200 Å thickness graphs and cannot be seen in the 500 Å and 1000 Å graphs.

Ellipsometric angles were fitted using two Drude oscillators whose parameters are shown in Table 6. Optical conductivity using equation 47

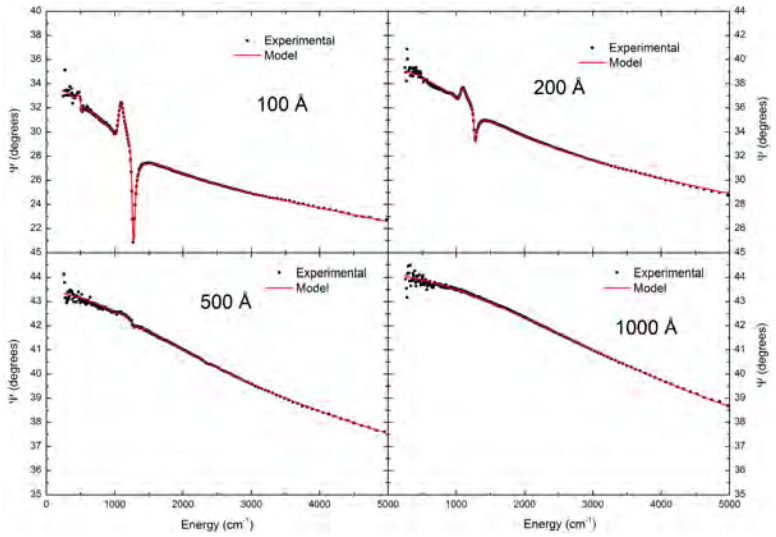


Figure 35: The ellipometric angle Ψ for different pure nickel films deposited on $SiO_2$ on Si substrate. The graph shows that thinner films are transparent whereas thicker films are opaque.

Figure 37 shows both real and imaginary parts of optical conductivity. The graph shows that the real part of optical conductivity increases with thickness which indicates that thicker samples absorb more light.

### 6.6 Unreacted $Ni_{1-x}Pt_x$ films on $SiO_2$

$Ni_{1-x}Pt_x$ alloys with different Pt concentrations were deposited on top of a thick layer of $SiO_2$ (2000 Å) to prevent interaction with the silicon substrate when annealed. Our previous work on the same set of films showed that there had to be a layer of water about 25 Å thick on top of the metal film. To be consistent with this result, we added a layer of water on top of the unreacted metal alloy films. The effect of the water layer as well as the $SiO_2$ absorption structure are shown in figure 38.

Optical conductivity is shown in figure 39. Two different trends are shown in the real part part of the optical conductivity graph below and above 1000 $cm^{-1}$.

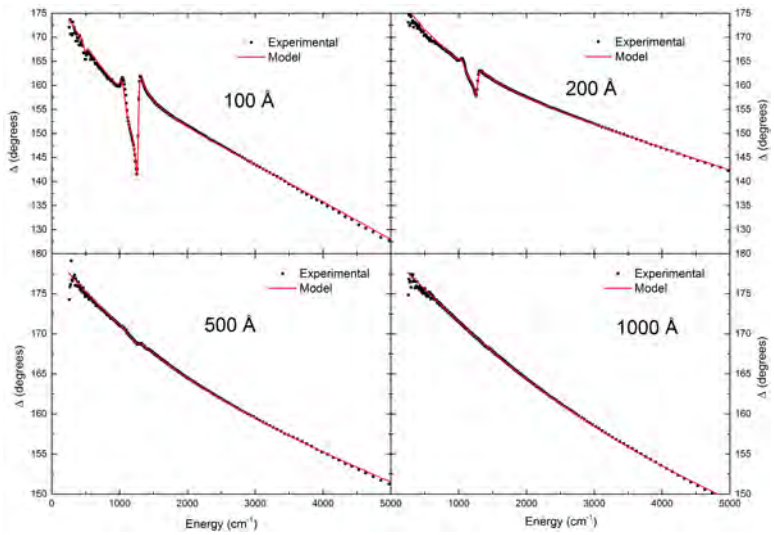


Figure 36: The ellipometric angle $\Delta$ for different pure nickel films deposited on $SiO_2$ on Si substrate. The graph shows that thinner films are transparent whereas thicker films are opaque.

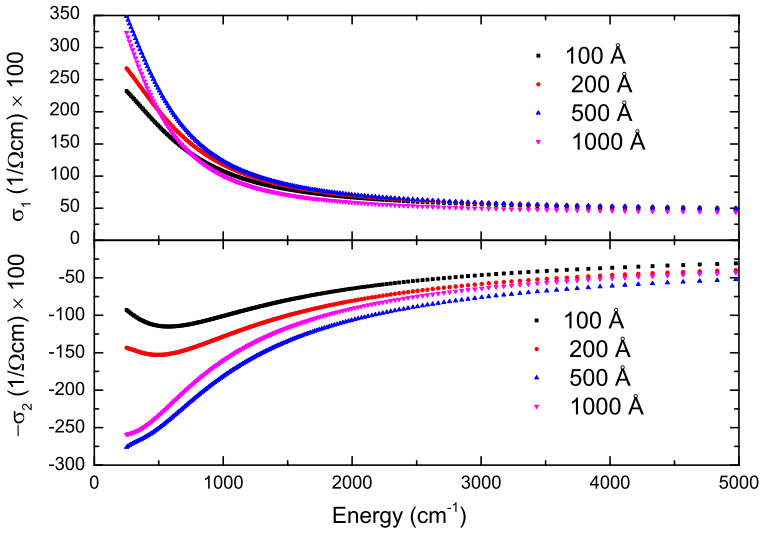


Figure 37: The real and the imaginary parts of optical conductivity for pure nickel films with different thicknesses using an oscillator fit with two Drude oscillators that describe free carrier absorption and intraband transitions.

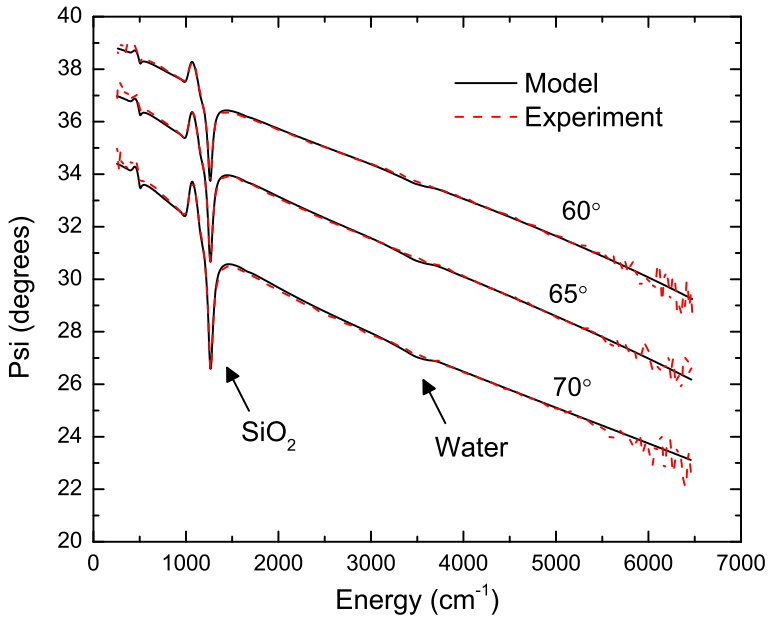


Figure 38: The ellipometric angle $\Psi$ for a $Ni_{0.9}Pt_{0.1}$ alloy film deposited on $SiO_2$ on a Si substrate measured at three angles of incidence. The graph shows the Si-O vibration at 1100 $cm^{-1}$. The structure at around 3500 $cm^{-1}$ is due to vibrations in the water layer on top of the alloy.

Absorption increases with Pt content above 1000 $cm^{-1}$ and decreases with Pt content below 1000 $cm^{-1}$. The result

Fits were done using two Drude oscillators to describe absorption in the metallic layer. The Drude parameters are shown in table 7.

### 6.7 $Ni_{1-x}Pt_xSi$ Monosilicides

A set of 100 Å thick $Ni_{1-x}Pt_x$ alloy films with different platinum concentrations (0 to 30%) were deposited on top of a silicon substrate and annealed at 500 for 30 seconds to create 200 Å layer of $Ni_{1-x}Pt_xSi$ monosilicides with 10 Å layer of $SiO_2$ on top.

The complex optical conductivity for the $Ni_{1-x}Pt_xSi$ monosilicides is shown in figure 40. The structure at 1100 $cm^{-1}$ present in the $Ni_{1.0}Pt_{0.0}$ which is attributed

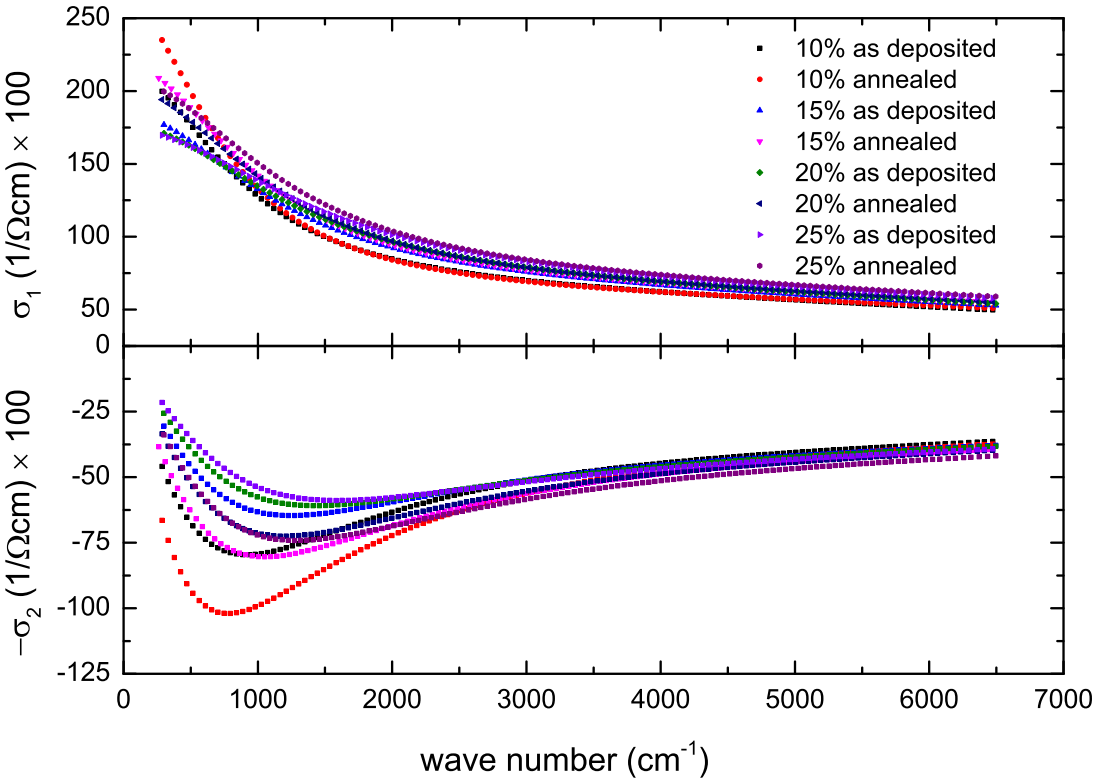


Figure 39: The real and imaginary parts of the optical conductivity for $Ni_{1-x}Pt_x$ alloys with different Pt composition and annealing conditions using an oscillator fit that consists of two Drude oscillators.

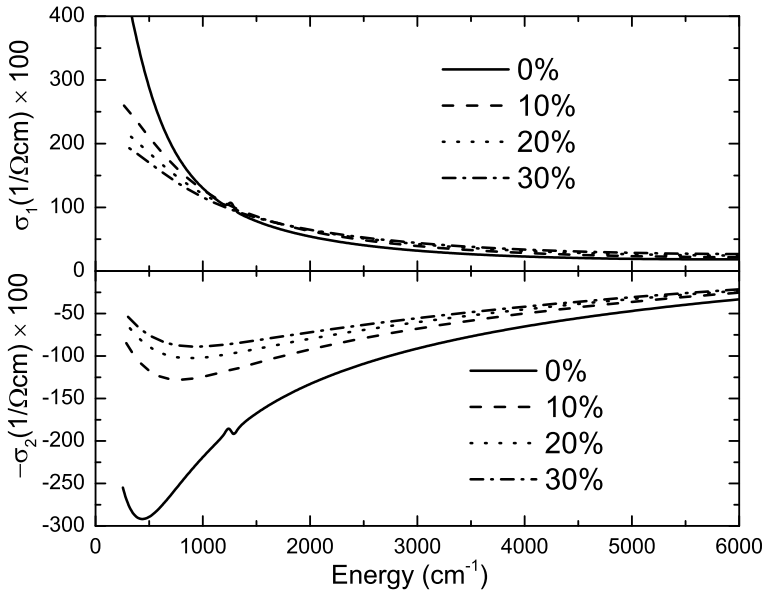


Figure 40: The real and imaginary parts of the optical conductivity for $Ni_{1-x}Pt_xSi$ monosilicide with different Pt compositions, determined from a Drude-Lorentz oscillator fit.

to the bond streching of the oxygen atoms relative to silicon indicates that there might be some oxygen atoms in the silicide layer.

The trends seen in the real part of the optical conductivity graph are similar to those seen in the pure nickel data.

Ellipsometric data for monosilicides was fitted using two Drude terms to describe free electron absorption as well as a Lorentz oscillator to describe the interband transitions caused by silicon.

### 6.8 Data Analysis

Nagel and Schnatterly [102] had shown that two carrier effect is needed to describe the frequency dependent relaxation energy in infrared region. It states that the two carrier effect is attributed to two sets of electrons located inside the crystallites and at the grain boundaries, each responds to the applied AC electric

field differentely.

The general equation of the Drude-Lorentz model is given by the equation [44, 42, 5, 22]

$$\epsilon(E) = 1 - \frac{E_P^2}{E(E + i\Gamma_d)} + \sum_{j=1}^{n} \frac{A_j E_j^2}{E_j^2 - E^2 - i\Gamma_j E} \tag{50}$$

where the first term describes the permeability of vacuum, the second term represents the Drude contribution and the third term represents a sum of Lorentz oscillators that describe interband transitions.

Tables 6, 7 and 8 list the oscillator parameters for pure nickel, $Ni_{1-x}Pt_x$, and $Ni_{1-x}Pt_xSi$ monosilicides films respectively.

### 6.9 Discussion

Hunderi [104] had shown the impact crystallite structure has on the optical properties of metals. Two sets of electrons with different densities are located in the voids and defects along grain boundaries and insite crystallites. This theory can be used to explain the need of two Drude parameters to fit the ellipsometric data for pure Ni films and $Ni_{1-x}Pt_x$ alloys. $Ni_{1-x}Pt_xSi$ monosilicides cannot be fitted using two Drude terms since there will be some interband transitions caused by the overlapping between the metal and Si bands [101]

The DC conductivity is calculated at zero photon energy (E=0). Using the Drude parameters we obtained from our fits, we calculate

$$\sigma_0 = \sigma(E = 0) = \frac{\epsilon_0}{\hbar} \sum_i \frac{E_{Pi}^2}{\Gamma_{di}}, \tag{51}$$

Tables 7 and 8 show that DC conductivity decreases as the platinum content increases in the alloy. Table 7 also shows that annealed alloys have higher conductivity than as deposited. Table 6 show that thicker samples have lower DC

Table 6: Drude parameters (plasma energy $E_P$ and scattering rate $\Gamma_d$, in eV) for pure Ni films with varying thickness $t$ deposited on 2000 Å thick layers of $SiO_2$. $\sigma_0$ is the zero-energy optical conductivity calculated from Eq. (51) and $\sigma_{\rm exp}$ is the DC electrical conductivity of bulk Ni, both in units of $(\Omega{\rm cm})^{-1}$.

| $t$ (Å) | $E_{P1}$ | $\Gamma_{d1}$ | $E_{P2}$ | $\Gamma_{d2}$ | $\sigma_0 \times 10^5$ | $\sigma_{\rm exp} \times 10^5$ |
|---|---|---|---|---|---|---|
| 100 | 14.5 | 0.08 | 6.3 | 10 | 3.5 | |
| 200 | 14.9 | 0.07 | 5.9 | 4.5 | 4.3 | |
| 500 | 17.9 | 0.05 | 6.1 | 2.8 | 8.6 | |
| 1000 | 17.6 | 0.05 | 5.7 | 3.1 | 8.3 | 1.43[a] |

[a] Conductivity of bulk Ni from Litschel and Pop [50].

Table 7: Oscillator parameters for 100 Å unreacted $Ni_{1-x}Pt_x$ alloy films deposited on a 2000 Å thick layer of $SiO_2$. $\sigma_0$ is the zero-energy optical conductivity calculated from Eq. (51) and $\sigma_{\rm exp}$ is the DC electrical conductivity determined from sheet resistance measurements (in $1/\Omega$cm).

| $x$ | annealed | $E_{P1}$ | $\Gamma_{d1}$ | $E_{P2}$ | $\Gamma_{d2}$ | $\sigma_0 \times 10^5$ | $\sigma_{exp} \times 10^5$ |
|---|---|---|---|---|---|---|---|
| 0.10 | no | 6.8 | 1.4 | 10.6 | 0.11 | 1.42 | 0.23 |
| 0.10 | yes | 6.7 | 1.6 | 12.2 | 0.09 | 2.26 | 0.29 |
| 0.15 | no | 6.9 | 1.4 | 9.4 | 0.14 | 0.8 | 0.2 |
| 0.15 | yes | 7 | 1.5 | 10.7 | 0.12 | 1.33 | 0.23 |
| 0.20 | no | 7 | 1.4 | 9 | 0.16 | 0.7 | 0.19 |
| 0.20 | yes | 7 | 1.5 | 10.1 | 0.14 | 1.02 | 0.21 |
| 0.25 | no | 7 | 1.6 | 8.9 | 0.17 | 0.6 | 0.18 |
| 0.25 | yes | 7.1 | 1.6 | 10.2 | 0.15 | 0.9 | 0.22 |

Table 8: Oscillator parameters for 200 Å $Ni_{1-x}Pt_xSi$ monosilicides. Fits are done using two Drude parameters to describe free electron absorption and two Lorentz oscillators to describe interband transitions. Energies and broadenings are in units of eV, the amplitudes $A$ are dimensionless, and $\sigma$ is in units of $1/\Omega$cm.

| $x$ | $E_{P1}$ | $\Gamma_{d1}$ | $E_{P2}$ | $\Gamma_{d2}$ | $A_1$ | $E_1$ | $\Gamma_1$ | $A_2$ | $E_2$ | $\Gamma_2$ | $E_3$ | $A_3$ | $\sigma_0 \times 10^5$ | $\sigma_{\exp} \times 10^5$ |
|---|---|---|---|---|---|---|---|---|---|---|---|---|---|---|
| 0 | 20.6 | 0.55 | 5.4 | 0.37 | 56 | 0.16 | 0.006 | 3.4 | 0.75 | 0.28 | 1.8 | 57.7 | 10.5 | 0.6 |
| 0.10 | 13.4 | 0.09 | 5.9 | 0.4 | 19.4 | 0.16 | 0.01 | 4.2 | 0.77 | 0.4 | 1.8 | 54.7 | 2.7 | 0.3 |
| 0.20 | 12 | 0.1 | 5.4 | 0.47 | 14.5 | 0.16 | 0.006 | 7.5 | 0.76 | 0.4 | 1.8 | 57 | 2.04 | 0.25 |
| 0.30 | 11 | 0.1 | 6.3 | 0.44 | 14.6 | 0.16 | 0.006 | 7.5 | 0.76 | 0.4 | 1.8 | 57 | 1.72 | 0.22 |

conductivity due to reuced scattering from grain boundaries.

## 6.10 Conclusion

Infrared spectroscopic ellipsometry results for pure $Ni_{1-x}Pt_x$ metal alloys and $Ni_{1-x}Pt_xSi$ monosilicides showed the need of using two Drude oscillators to fit the ellipsometric data. This can be attributed to two types of carriers contributing to absorption. Two trends were seen in absorption for $Ni_{1-x}Pt_x$ metal alloys and $Ni_{1-x}Pt_xSi$ monosilicides, below and above 1000 $cm^{-1}$. Absorption seemed to broaden with increasing metal thickness due to reduced scattering.

## 6.11 Acknowledgments

This work was supported by the National Science Foundation (DMR-1104934). This work has been partially supported by the independent Bulk CMOS and SOI technology development projects at the IBM Microelectronics Division Semiconductor Research & Development Center, Hopewell Junction, NY 12533. This work was performed, in part, at Arizona State University and also at the Center for Integrated Nanotechnologies, an Office of Science User Facility operated for the U.S. Department of Energy (DOE) Office of Science by Los Alamos National Laboratory (Contract DE-AC52-06NA25396) and Sandia National Laboratories (Contract DE-AC04-94AL85000). We are grateful to Dr. R.J. Davis and his colleagues at The Ohio State University, Columbus, OH, for providing sputtered Ni films on $SiO_2$ with varying thicknesses.

# 7 Conclusion and Outlook

In this work we studied the effect of platinum concentration on the optical conductivity of different nickel platinum alloys and nickel platinum monosilicides. Platinum addition broadened the conductivity peak due to enhancement of states when compared to those for nickel. The broadening increased as the platinum concentration increased in the alloy. The same broadening was observed in the optical conductivity of $Ni_{1-x}Pt_xSi$ monosilicides. In the visible spectrum, data for both unreacted $Ni_{1-x}Pt_x$ alloys and $Ni_{1-x}Pt_xSi$ monosilicides were fit using a Drude term to describe free carrier absorption and intraband transitions as well as a set of Lorentz oscillators to describe interband transitions. Pure $Ni_{1-x}Pt_x$ alloys showed more metallic behavior in the low energy region whereas $Ni_{1-x}Pt_xSi$ monosilicides showed enhanced interband transitions due to the Si content in the silicide.

In the infrared region we required a set of two Drude oscillators. This can be attributed due to intraband transitions that are difficult to separate from free carrier absorption at low energies, or it can be due to two sets of carriers that exist inside the crystallite and near grain boundaries, both respond to the applied electric field in different ways and this results in different Drude parameters.

For future work, our aim is to be able to build one model that fits our data over a broad spectral range from 250 $cm^{-1}$ to 6.6 eV. We also hope to extend our measurements to cover the far-infrared and Terahertz regions. We also hope to perfom measurements under the effect of a magnetic field. The surface of our films can be studied further by looking at the optical constants of NiO.

We would like to study the temperature dependence of the optical conductivity for $Ni_{1-x}Pt_x$ alloys and $Ni_{1-x}Pt_xSi$ monosilicides.

## REFERENCES


[1] R. J. D. Tilley, *Colour and the Optical Properties of Materials*, (Wiley, New York, 2011)

[2] J.A. Woolam Co., Inc., *Guide to Using WVASE32®*, (J.A. Woollam Co., Inc., Lincoln, NE, 2009)

[3] R.M.A. Azzam and N.M. Bashara, *Ellipsometry on Polarized Light,* (North-Holland Publ. Co., Amsterdam, 1984).

[4] H.G. Tompkins and W.A. McGahan, *Spectroscopic Ellipsometry and Reflectometry*, (Wiley, New York, 1999).

[5] H. Fujiwara, *Spectroscopic Ellipsometry*, (Wiley, Chichester, UK, 2007).

[6] C. M. Nelson, M Spies, L.S. Abdallah, S. Zollner, Y. Xu, and H. Luo, J. Vac. Sci. Technol. A **30**, 061404 (2012).

[7] L.S. Abdallah, T.M. Tawalbeh, I.V. Vasiliev, S. Zollner, C. Lavoie, A. Ozcan, and M. Raymond, AIP Advances **4**, 017101, 2014.

[8] M. R. Derrick, D. Stulik, J.M. Landry *Infrared Spectroscopy in Conservation Science*, (The Getty Conservation Institute, Los Angeles, USA, 1999).

[9] C. Kittel, *Introduction to Solid State Physics*, (Wiley, New York, 1996), ch. 10, p. 271.

[10] P.Y. Yu and M. Cardona, *Fundamentals of Semiconductors*, (Springer, Berlin, 1996).

[11] J.D. Jackson, *Classical Electrodynamics,* (Wiley, New York, NY, 3rd edition, 1999).

[12] K.A. Jenkins,J.N. Burgharz and P.D. Agnello, IEEE Trans. Electron Devices **43**, 759 (1996).

[13] R. Pretorius and J. W. Mayer, J. Appl. Phys. **81**, 2448 (1997).

[14] H. Bentmann, A.A. Demkov, R. Gregory, and S. Zollner, Phys. Rev. B. **78**, 205302 (2008).

[15] J.H. Gülpen, A.A. Kodentsov, F.J.J. van Loo, Zeitschrift fuer Metallkunde **5**, 530-539 (1995).

[16] R.C. Vehse and E.T. Arakawa, Phys. Rev. **180**, 695 (1969).

[17] V. Theodorescu, L. Nistor, H. Bender, A. Steegen, A. Lauwers, K. Maex, and J. Van Landuyt, J. Appl. Phys. **90**, 167 (2001).

[18] G. E. Moore, Cramming more components onto integrated circuits Electronics, **38**, 114-117 (1965).

[19] J.M. Poate, K.N. Tu, and J.W. Mayer, *Thin Films: Interdiffusion and Reactions*, (Wiley-Interscience, New York, 1978).

[20] J.W. Mayer and S.S. Lau, *Electronic Materials Science for Integrated Circuits in Si and GaAs*, (Macmillan, New York, 1990).

[21] D.Z. Chi, D. Mangelinck, J. Y. Dai, S. K. Lahiri, K. L. Pe and C. S. Ho, App. Phys. Lett. **76**, 3385-3387 (2000).

[22] V.W. Kamineni, M. Raymond, E.J. Bersch, B.B. Doris, and A.C. Diebold, J. Appl. Phys. **107**, 093525 (2010).

[23] C. Lavoie, C. Detavernier, C. Cabral Jr, F.M. d'Heurle, A.J. Kellock, J. Jordan-Sweet, J.M.E Harper, Microelectronic Engineering **83**, 2042-2054 (2006).

[24] F.M. dHeurle, J. Electron. Mat. **27**, 1138 (1998).

[25] E. Laves and H.J. Wallbaum, Z. Kristallogr. **101**, 78 (1939).

[26] R. Beyers and R. Sinclair, J. Appl. Phys. **57**, 5240 (1985).

[27] D. Mangelinck, J.Y. Dai, J.S. Pan, and S.K. Lahiri, App. Phys. Lett. **75**, 1736 (1999).

[28] C. Detavernier and C. Lavoie, App. Phys. Lett. **84**, 3549 (2004).

[29] Ward, 111 *et al.* (2011). *US Patent No. 7,875,545 B2*

[30] S.P Muraka , Ann. Rev. Matter. Sci. **13**, 117-137 (1983).

[31] E.D. Palik, *Handbook of Optical Constants of Solids*, Vols. 1-3 (Academic, San Diego, 1998).

[32] D.W. Lynch and W.R. Hunter, in *Handbook of Optical Constants of Solids*, edited by E.D. Palik (Academic, San Diego, 1998), p. 275.

[33] J.N. Hilfiker *et al.*, Thin Solid Films **516**, 7979 (2008).

[34] R.A. Synowicki, phys. stat solidi (c) **5**, 1085 (2008).

[35] Central Pneumatic 220 grit white alumina abrasive (68 $\mu$m average particle size, item 66846) was blown onto the Si surface using a small hand-held gravity feed blast gun (item 95793) and a 1/3 hp, 3 gallon, 100 psi oilless air compressor (item 95275). A few seconds are sufficient to roughen the sample.

[36] P.B. Johnson and R.W. Christy, Phys. Rev. B **9**, 5056 (1974).

[37] S. Zollner *al.*, in *2007 International Conference on Frontiers of Characterization and Metrology*, edited by D.G. Seiler, A.C. Diebold, R. McDonald, C.M. Garner, D. Herr, R.P. Khosla, and E.M. Secula, AIP Conf. Proc. **931**, 337-346 (2007).

[38] R.M.A. Azzam and N.M. Bashara, *Ellipsometry and Polarized Light*, (North-Holland, Amsterdam, 1977).

[39] J.A. Woollam Co., Inc., Lincoln, NE. Model V-VASE.

[40] C.M. Herzinger, B. Johs, W.A. McGahan, J.A. Woollam, and W. Paulson, J. Appl. Phys. **83**, 3323 (1998).

[41] H. Arwin and D.E. Aspnes, Thin Solid Films **113**, 101 (1984); J. Vac. Sci. Technol. A **2**, 1316 (1984).

[42] S. Roberts, Phys. Rev. **114**, 104 (1959).

[43] H. Raether, *Solid State Excitations by Electrons*, in *Springer Tracts in Modern Physics*, edited by G. Höhler, (Springer, Berlin, 1965), **38**, p. 84.

[44] P. Drude, *The Theory of Optics*, (Longmans, Green, and Company, New York, 1902), p. 398.

[45] P.B. Johnson and R.W. Christy, Phys. Rev. B **11**, 1315 (1975).

[46] M. Losurdo *et al.*, J. Phys. Chem. C **116**, 23004 (2012).

[47] V.P. Drachev, U.K. Chettiar, A.V. Kildishev, H.K. Yuan, W. Cai, and V.M. Shalaev, Opt. Express **16**, 1186 (2008).

[48] D.N. Basov, R.D. Averitt, D. van der Marel, M. Dressel, and K. Haule, Rev. Mod. Phys. **83**, 471 (2011).

[49] P.B. Johnson and R.W. Christy, Phys. Rev. B **6**, 4370 (1972).

[50] H. Litschel and I. Pop, J. Phys. Chem. Solids **46**, 1421 (1985).

[51] B. Johs and J.S. Hale, phys. stat. solidi (a) **205**, 715 (2008).

[52] R.C. Vehse and E.T. Arakawa, Phys. Rev. **180**, 695 (1969).

[53] T.A. Gavrilova, V.V. Atuchin, V.N. Kruchinin, and D.V. Lychagin, Physics Procedia **23**, 61 (2012).

[54] L.S. Abdallah, S. Zollner, C. Lavoie, A. Ozcan, and M. Raymond, Thin Solid Film (in print)

[55] D.W. Lynch, R. Rosei, and J.H. Weaver, Solid State Commun. **9**, 2195 (1971).

[56] M. Stoll, Solid State Commun. **8**, 1207 (1970).

[57] M. Stoll, J. Appl. Phys. **42**, 1717 (1971).

[58] M. Losurdo, (unpublished).

[59] R.J. Powell and W.E. Spicer, Phys. Rev. B **2**, 2182 (1970).

[60] R.A. Synowicki, G.K. Pribil, G. Cooney, C.M. Herzinger, S.E. Green, R.H. French, M.K. Yang, J.H. Burnett, and S. Kaplan, J. Vac. Sci. Technol. B **22**, 3450 (2004).

[61] M.R. Querry, D.M. Wieliczka, and D.J. Segelstein, in *Handbook of Optical Constants of Solids II*, edited by E.D. Palik, (Academic Press, San Diego, CA, 1991), p. 1059.

[62] T.E. Tiwald, D.W. Thompson, J.A. Woollam, and S.V. Pepper, Thin Solid Films **313-314**, 718 (1998).

[63] H. Ehrenreich, H.R. Philipp, and D.J. Olechna, Phys. Rev. **131**, 2469 (1963).

[64] D.Y. Petrovykh, K.N. Altmann, H. Höchst, M. Laubscher, S. Maat, G.J. Mankey, and F.J. Himpsel, Appl. Phys. Lett. **73**, 3459 (1998).

[65] P. Hohenberg and W. Kohn, Phys. Rev. **136**, B864 (1964).

[66] W. Kohn and L.J. Sham, Phys. Rev. **140**, A1133 (1965).

[67] L. Kleinman and D.M. Bylander, Phys. Rev. Lett. **48**, 1425 (1982).

[68] N. Troullier and J.L. Martins, Phys. Rev. B **43**, 1993 (1991).

[69] J.P. Perdew, K. Burke, and M. Ernzerhof, Phys. Rev. Lett. **77**, 3865 (1996).

[70] P. Ordejon, E. Artacho, and J.M. Soler, Phys. Rev. B **53**, R10441 (1996).

[71] J.M. Soler, E. Artacho, J. Gale, A. Garcia, J. Junquera, P. Ordejon, and D. Sanchez-Portal, J. Phys. Condens. Mat. **14**, 2745 (2002).

[72] F. El-Mellouhi, N. Mousseau, and P. Ordejon, Phys. Rev. B **70**, 205202 (2004).

[73] M.Ph. Stoll and C. Jung, J. Phys. F Met. Phys. **9**, 2491 (1979).

[74] C.S. Wang and J. Callaway Phys. Rev. B **9**, 4897 (1974).

[75] M.B. Stearns, J. Mag. Mag. Mat. **5**, 167 (1977).

[76] L.G. Wang and Alex Zunger, Phys. Rev. B **67**, 092103 (2003).

[77] A. Pisanty, C. Amador, Y. Ruiz, and M. de la Vega, Z. Phys. B Con. Mat. **80**, 237 (1990).

[78] See Supplemental Material at *URL to be inserted by publisher* for tabulated dielectric functions of $Ni_{1-x}Pt_x$ alloys at 300 K versus energy from 0.8 to 6.6 eV for $x$=0, 0.10, 0.15, 0.20, 0.25.

[79] J.A. Kittl, A. Lauwers, O. Chamirian, M.A. Pawlak, M. Van Dal, A. Akheyar, M. De Potter, A. Kottantharayil, G. Pourtois, R. Lindsay, and K. Maex, MRS Symp. Proc. **810**, C2.1 (2004).

[80] Karen Maex and Marc van Rossum, *Properties of Metal Silicides*, (INSPEC,London, 1995).

[81] M. Christensen, V. Eyert, C. Freeman, E. Wimmer, A. Jain, J. Blatchford, D. Riley and J. Shaw, J. Appl. Phys. **114**, 033533 (2013).

[82] A. Vellei, R. Fallica, D. Sangalli, and A. Lamperti, J. Appl. Phys. **111**, 093501 (2012).

[83] M.A. Nicolet and S. Lau, in *VLSI Electronics: Microstruture Science*, Vol. 6, ed. by N.G. Einspruch and G. Larrabee (Academic Press, NY, 1983).

[84] J.A. Woollam vertical VASE, J.A. Woollam Co., Lincoln, NE.

[85] G.J. Huang and L.J. Chen, J. Appl. Phys. **78**, 2 (1995).

[86] A. Cros R. A. Cros, R. A. Pollak, and K. N. Tu, J. Appl. Phys. **57**, 6 (1985).

[87] H. Arwin, and D.E. Aspnes, J. Vac. Sci. Technol. A **2**, 1316 (1984).

[88] P. Lautenschlager, M. Garriga, L. Vina, and M. Cardona, Phys. Rev. B. **36**, 48214830 (1987).

[89] M. Amiotti, A. Borghesi, G. Guizzetti, and F. Nava, Phys. Rev. B **42**, 8939 (1990).

[90] O. Bisi and C. Calandra, J. Phys. C **14**, 5479 (1981).

[91] O. Bisi, C. Calandra, U. del Pennino, P. Sassaroli, and S. Valeri, Phys. Rev. B **30**, 5696 (1984).

[92] D.D. Sarma, W. Speier, R. Zeller, E. van Leuken, R.A. de Groot, and J.C. Fuggle, J. Phys. Condens. Mat. **1**, 9131 (1989).

[93] L. Vočadlo, I.G. Wood, and D.P. Dobson, J. Appl. Cryst. **45**, 186 (2012).

[94] M. Tinani, A. Mueller, Y. Gao, and E. A. Irene, J. Vac. Sci. Technol. B **19**, 376 (2001).

[95] Q. Zhang, C.W. Han, and C. Zhu, J. Electrochem. Soc. **154**, H314 (2007).

[96] S.M. Zhou, M. Hundhausen, T. Stark, L.Y. Chen, and L. Ley, J. Vac. Sci. Technol. A **17**, 144 (1999).

[97] H.-W. Chen and J.-T. Lue, J. Appl. Phys. **59**, 2165 (1986).

[98] J.R. Jimenez, Z.-C. Wu, L.J. Schowalter, B.D. Hunt, R.W. Fathauer, P.J. Grunthaner, and T.L. Lin, J. Appl. Phys. **66**, 2738 (1989).

[99] S.A. Campbell, *The Science and Engineering of Microelectronic Fabrication* (Oxford, New York, 2001), p. 5.

[100] T. Sonehara, A. Hokazono, H. Akutsu, T. Sasaki, H. Uchida, M. Tomita, H. Tsujii, S. Kawanaka, S. Inaba, and Y. Toyoshima, 2008 IEEE International Electron Devices Meeting, p. 921.

[101] L.S. Abdallah, S. Zollner, C. Lavoie, A. Ozcan, and M. Raymond, J. Vac. Sci. Technol. (under review).

[102] S.R. Nagel, S.E. Schnatterly, Phys. Rev. B. **9**, 12991303 (1974).

[103] R. Bell, N.F. Bird and P. Dean, Proc. Phys. Soc. **1**, 209-303 (1968).

[104] O. Hunderi, Phys. Rev. B. **7**, 34193429 (1973).